

**“ON THE CHARACTERISATION OF  
SOLAR CELLS USING LIGHT BEAM  
INDUCED CURRENT  
MEASUREMENTS”**

**N. KWARIKUNDA**

**2015**

**“ON THE CHARACTERISATION OF SOLAR  
CELLS USING LIGHT BEAM INDUCED  
CURRENT MEASUREMENTS”**

By

**Nicholas KWARIKUNDA**

Submitted in fulfilment of the requirements for the degree of

**PHILOSOPHIAE DOCTOR**

in the Faculty of Science

at the Nelson Mandela Metropolitan University

Supervisor: Prof. E.E. van Dyk

Co-Supervisor: Dr. F.J. Vorster

Co-Supervisor: Dr. W. Okullo

March, 2015

# Declaration

Full Names: Nicholas KWARIKUNDA

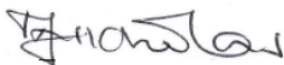
Student Number: 212319116

Qualification: PHILOSOPHIAE DOCTOR

Title of Project: "On the Characterisation of Solar Cells using Light Beam Induced Current Measurements"

In accordance with Rule G4.6.3, I hereby declare that the above-mentioned thesis is my own work and that it has not previously been submitted for assessment to another University or for another qualification.

Signature



8th March 2015

# Dedication

To my mother **Alice Rutagyirenda** and to the memory of my father **Francis Rutagyirenda**



# Acknowledgement

I would like to thank my supervisors Prof. EE van Dyk, Dr. FJ Vorster and Dr. W Okullo for the invaluable guidance through out my PhD work. Your insightful and thought provoking comments always kept me on my toes through out my work. Thank you for always encouraging me and allowing me to grow as a research scientist. I also wish to thank Jualine Ferreira for the administrative work and the parental guidance accorded to me during my study. You were a mother to me, always willing to listen and help whenever I would walk into your office and you made sure that I felt at home away from home. To Len Compton, I am grateful for the technical assistance during the development of the LBIC system.

I wish to thank colleagues and members of the PV research group for the fruitful discussions we had, both formal and informal, and the assistance rendered to me during my studies; Lucian Bezuidenhout for the LBIC and Matlab discussions, Jacqui Crozier for the EL and PL characterisation techniques, Ross Schultz for the CTJ discussions and Michael Okullo for his assistance with the Keithley SMU instrument. To Dr. Denis Okello, I am so grateful for your words of wisdom and encouragement and for being there with me in the “bush”. You motivated me to push on when the going got tough.

My time at NMMU was made enjoyable by a number of friends and colleagues in the struggle with whom we would occasionally organise some Braais or share a cup of tea just to take away the stress. Enoch, Valentine, Doreen, Penninah, Duncan, Edwige, Sr Anne, thank you for being good friends and for your moral support and encouragement. It has been a memorable and delightful three years.

I am so grateful for the financial support from the African Laser Centre (ALC), Nelson Mandela Metropolitan University and Makerere University, without which it would have been impossible to undertake this PhD study.

Lastly, I am grateful to my wife Annetah and children Alicia, Arnold and Albert for their support and for enduring my long absence. It has indeed been a long walk!

# Abstract

The presence of inhomogeneities in semiconductor materials used to fabricate solar cell devices may result in spatial non uniformities in the device properties which may affect current generation in these devices. Besides, current reducing defects such as inclusions, local shunts and optical blockages may be introduced during the various device manufacturing processes which may adversely affect the performance and overall efficiency of solar cells. Diagnostic techniques are therefore needed to identify these defects so as to improve the production technology. This thesis presents the Light Beam Induced Current (LBIC) technique for mapping spatial non uniformities in solar cell devices. The LBIC is a non destructive characterisation technique that uses a focused light beam to raster scan a solar cell surface as the photo-generated current is recorded as a function of position to generate a photo-response map. The technique was used to obtain photo-response maps for a mc-Si, Back contact Back junction (BC-BJ) silicon solar cell and the InGaP/InGaAs/Ge concentrating triple junction (CTJ) solar cell from which various local current reducing defects were mapped. A reflection signal detector was incorporated into the LBIC measurement system to enable us distinguish between optical blockages on the cell surface and current reducing defects within the solar cell devices. By dynamically biasing the solar cell devices, the electrical activity of the identified defects was investigated and also point-by-point current-voltage (I-V) characteristics were obtained. An interval division algorithm was applied to the measured point-by-point I-V characteristics to extract device and performance parameters from which device and performance parameter uniformity of the devices were mapped. Dark and full cell solar illumination I-V characteristics were also measured to extract device parameters. Analysis of extracted parameters revealed differences between extracted dark and illuminated device parameters which was attributed to departure from the superposition principle due to non-linearity of the semiconductor device equations with respect to carrier concentration. An investigation into the effect of illumination intensity on the I-V parameters of a spot illuminated BC-BJ Si solar cell showed a linear increase and a logarithmic increase of the short circuit current and open circuit voltage respectively with intensity while the series resistance decreased with intensity, which was attributed to increase in conductivity of the active layer. The ideality factor and saturation current were observed to increase while the shunt resistance initially increased before decreas-

ing at higher intensity levels. Under monochromatic illumination, the photo-response of the BC-BJ Si cell was higher at  $785\text{ nm}$  than at  $445\text{ nm}$  due to low absorption coefficient of Si for longer wavelength radiations, resulting in carrier generation within the bulk, where there is a higher probability of carriers being collected at the p-n junction before they recombine. Under solar illumination, as the spectral content was altered using long pass colour filters with cut off wavelengths of  $610\text{ nm}$  and  $1000\text{ nm}$ , the performance parameters were observed to decrease and this was mainly due to decrease in intensity. For the CTJ solar cell, however, blocking of radiations below  $610\text{ nm}$  resulted in current mismatch that severely degraded the short circuit current ( $I_{sc}$ ). The current mismatch affected the extracted device and performance parameters. With a  $1000\text{ nm}$  long pass filter, a dark I-V was obtained since only the bottom Ge subcell was activated.

Key words: LBIC, concentrator solar cells, characterisation, photo-response, device parameters, performance parameters.

# Contents

<b>Declaration</b>	<b>i</b>
<b>Dedication</b>	<b>ii</b>
<b>Acknowledgement</b>	<b>iii</b>
<b>Abstract</b>	<b>iv</b>
<b>1 Introduction</b>	<b>1</b>
1.1 Concentrating photovoltaics . . . . .	5
1.2 Thesis objectives and outline . . . . .	6
1.2.1 Thesis objectives . . . . .	6
1.2.2 Content outline . . . . .	7
<b>2 Basics of solar cells and concentrator photovoltaic systems</b>	<b>9</b>
2.1 Introduction . . . . .	9
2.1.1 Solar cells and the solar spectrum . . . . .	10
2.2 Device Physics . . . . .	11
2.2.1 Bulk recombination . . . . .	12
2.2.1.1 Radiative recombination . . . . .	13
2.2.1.2 Auger recombination . . . . .	13
2.2.1.3 Recombination through defect levels . . . . .	14
2.2.2 Surface recombination . . . . .	15
2.2.3 Semiconductor diode characteristics . . . . .	16
2.2.4 Solar cell parameters . . . . .	18
2.2.4.1 Open circuit voltage . . . . .	19
2.2.4.2 Short circuit current . . . . .	19
2.2.4.3 Maximum power output . . . . .	20

2.2.4.4	Fill factor and efficiency . . . . .	20
2.2.4.5	Parasitic resistance . . . . .	21
2.2.5	Temperature effect . . . . .	22
2.3	Solar cells under concentration . . . . .	23
2.3.1	Effect of illumination intensity . . . . .	23
2.3.2	Effect of concentration on recombination . . . . .	24
2.4	Quantum efficiency and spectral response . . . . .	26
2.5	Solar cell equivalent circuit models . . . . .	27
2.6	Concentrator photovoltaic systems . . . . .	29
2.6.1	Silicon concentrator solar cells . . . . .	29
2.6.1.1	Back contact-Back junction silicon solar cells . . . . .	30
2.6.1.2	Emitter wrap through silicon solar cells . . . . .	31
2.6.1.3	Metal wrap through. . . . .	32
2.6.2	Multijunction concentrator solar cells . . . . .	33
2.6.2.1	Mechanically stacked multijunction solar cells . . . . .	34
2.6.2.2	Monolithic multijunction solar cells . . . . .	35
2.6.2.3	Effect of current mismatch on I-V characteristics . . . . .	39
2.7	Conclusion . . . . .	40
<b>3</b>	<b>LBIC mapping technique and system development</b>	<b>41</b>
3.1	Introduction . . . . .	41
3.2	Overview of LBIC systems . . . . .	42
3.3	LBIC system characterisation . . . . .	44
3.3.1	Beam diameter . . . . .	45
3.3.2	Generation volume . . . . .	46
3.3.3	Beam probe intensity . . . . .	47
3.3.4	System resolution . . . . .	47
3.4	System development . . . . .	48
3.4.1	Optics sub-system . . . . .	49
3.4.2	Sample positioning . . . . .	50
3.4.3	Electronics sub-system . . . . .	51
3.4.4	Computer control and data acquisition . . . . .	52
3.4.5	Reflection measurements . . . . .	55
3.5	Spot illuminated solar cell model . . . . .	56

3.6	Multi-crystalline silicon solar cell photo-response mapping . . . . .	57
3.7	Conclusion . . . . .	59
<b>4</b>	<b>Solar cell parameter extraction</b>	<b>60</b>
4.1	Introduction . . . . .	60
4.2	Parameter extraction algorithm . . . . .	61
4.2.1	Goodness of fit . . . . .	64
4.3	Multi-crystalline silicon solar cell I-V parameters . . . . .	64
4.3.1	Dark I-V characteristics . . . . .	64
4.3.2	Illuminated I-V characteristics . . . . .	66
4.3.2.1	Full cell illumination . . . . .	66
4.3.2.2	Solar cell under spot illumination . . . . .	68
4.4	Conclusion . . . . .	70
<b>5</b>	<b>Concentrator solar cell characterisation</b>	<b>72</b>
5.1	Introduction . . . . .	72
5.2	Back contact Back junction silicon solar cell . . . . .	73
5.2.1	Photo-response mapping . . . . .	73
5.2.2	I-V measurements and parameter extraction . . . . .	76
5.2.2.1	Dark I-V measurements . . . . .	76
5.2.2.2	Full cell illuminated I-V measurements . . . . .	77
5.2.2.3	Parameter maps . . . . .	78
5.3	InGaP/InGaAs/Ge triple junction solar cell . . . . .	81
5.3.1	Photo-response mapping . . . . .	83
5.3.2	I-V measurements and parameter extraction . . . . .	85
5.3.2.1	Dark I-V measurements . . . . .	85
5.3.2.2	Full cell solar illumination . . . . .	87
5.3.2.3	Spot illuminated I-V curve . . . . .	88
5.3.3	S-LBIC measurements . . . . .	89
5.4	Conclusion . . . . .	92
<b>6</b>	<b>Intensity and Spectral change effects on solar cell I-V parameters</b>	<b>93</b>
6.1	Introduction . . . . .	93
6.2	Effect of illumination intensity . . . . .	94
6.3	Effect of spectral change . . . . .	97

*Contents*

---

6.3.1	Back contact Back junction silicon solar cell . . . . .	97
6.3.1.1	Spot illumination . . . . .	97
6.3.1.2	Full cell illumination . . . . .	99
6.3.2	Concentrating triple junction solar cell under full cell illumination	101
6.4	Conclusion . . . . .	103
<b>7</b>	<b>Conclusion and outlook</b>	<b>105</b>
	<b>Bibliography</b>	<b>108</b>
<b>A</b>	<b>Research outputs associated with this work</b>	<b>124</b>
A.1	Journal publication . . . . .	124
A.2	Conference papers . . . . .	124
<b>B</b>	<b>Awards received</b>	<b>125</b>

# List of Figures

1.1	World primary energy consumption since 1988. . . . .	1
1.2	Record efficiencies for various types of research solar cells since 1975 . . .	3
1.3	Cummulative installed global solar PV power from 2004 to 2013 . . . . .	4
1.4	Principle of a CPV solar cell system using a Fresnel lens. . . . .	5
1.5	World map showing long term average levels of Direct Normal Irradiance	6
2.1	Solar spectra for space and terrestrial use . . . . .	10
2.2	I-V characteristics of a diode in dark and under illumination. . . . .	18
2.3	The Light I-V characteristic of a solar cell in the first quadrant showing the solar cell performance parameters. . . . .	18
2.4	Simulated effect of parasitic resistances on I-V curves of solar cells . . . .	21
2.5	Effect of temperature on I-V characteristics of a solar cell. . . . .	23
2.6	Typical quantum efficiency and reflectance curves of a semiconductor ma- terial. . . . .	26
2.7	Single diode equivalent circuit model. . . . .	28
2.8	Double diode equivalent circuit diagram. . . . .	28
2.9	Cross-section and structure of an IBC solar cell. . . . .	30
2.10	Illustration of an emitter wrap through (EWT) Silicon solar cell . . . . .	32
2.11	Structure of a Metal Wrap through (MWT) solar cell . . . . .	32
2.12	Spectral losses in single and multijunction solar cells . . . . .	34
2.13	Mechanically stacked multijunction solar cell . . . . .	35
2.14	Structure of a monolithic concentrating triple junction (CTJ) solar cell . .	36
2.15	Equivalent circuit model of a CTJ solar cell. . . . .	36
2.16	I-V characteristic of a tunnel diode . . . . .	37
2.17	Schematic diagram of a 3-junction inverted metamorphic solar cell . . . .	39
2.18	Simulated subcell I-V characteristics and the combined. . . . .	40
3.1	Short circuit current variation across a bus bar . . . . .	45



*List of Figures*

---

3.2	Schematic illustration of the generation volume of a solar cell device. . . .	46
3.3	Schematic diagram showing the main components of the LBIC system. . .	48
3.4	LBIC system built for indoor and outdoor measurements . . . . .	49
3.5	XY translation stages. . . . .	51
3.6	Flow diagram for the scanning program. . . . .	52
3.7	Front panel of the main window of the Labview scanning program. . . .	53
3.8	Screenshot of the scan type selection window. . . . .	54
3.9	Screenshot of the single spot continuous I-V curve measurement window. .	54
3.10	Reflection detector before and after mounting above the stage. . . . .	55
3.11	Equivalent circuit diagram of a spot illuminated solar cell. . . . .	56
3.12	Short circuit current ( $I_{sc}$ ) map of a mc-Si showing grain boundaries. . . .	57
3.13	Reflection map of a mc-Si solar cell. . . . .	58
4.1	Interval division algorithm flow chart. . . . .	62
4.2	Screenshot of the Labview Front Panel for the Parameter extraction algo- rithm . . . . .	63
4.3	Measured and fitted Dark I-V curve for a mc-Si solar cell. . . . .	65
4.4	Measured and Fitted full cell illumination I-V characteristic of a mc-Si solar cell. . . . .	67
4.5	Performance parameters of a mc-Si solar cell. . . . .	68
4.6	Reflection map of a mc-Si solar cell showing a surface defect. . . . .	69
4.7	Extracted device parameters of a mc-Si solar cell. . . . .	70
5.1	a) $I_{sc}$ map, b) Reflection map of a BC-BJ silicon solar cell. . . . .	74
5.2	Line scan through a defect region at different biasing voltages. . . . .	74
5.3	Two dimensional symmetry element of a BC-BJ silicon solar cell . . . . .	75
5.4	Dark I-V curve for a BC-BJ silicon concentrator solar cell. . . . .	76
5.5	Full cell illumination I-V curve of a BC-BJ silicon solar cell. . . . .	77
5.6	$I_{sc}$ map of the area around the defect . . . . .	79
5.7	Spot illuminated I-V curves extracted from LBIC measurements . . . . .	79
5.8	Device parameter maps for a BC-BJ solar cell . . . . .	80
5.9	Performance parameter maps for a BC-BJ solar cell . . . . .	81
5.10	CTJ Receiver Assembly . . . . .	82
5.11	Spectral response of individual subcells of InGaP/InGaAs/Ge CTJ . . . . .	83
5.12	CTJ solar cell under a forward bias of 3 V showing electroluminescence. .	83

*List of Figures*

---

5.13	$I_{sc}$ map for the InGaP/InGaAs/Ge CTJ using a 660 nm wavelength laser. . . . .	84
5.14	Dark I-V characteristic of a CTJ solar cell. . . . .	86
5.15	Full cell illumination I-V characteristic of a CTJ solar cell . . . . .	87
5.16	Point illuminated I-V curve extracted from LBIC measurements. . . . .	89
5.17	CTJ solar cell performance parameter maps . . . . .	90
5.18	CTJ solar cell device parameter maps . . . . .	91
6.1	I-V characteristics of a Back contact Back junction Si solar cell at different laser power outputs. . . . .	94
6.2	Variation of $I_{sc}$ and $V_{oc}$ with intensity for spot illuminated Back contact Back junction Si solar cell. . . . .	95
6.3	Shunt and series resistance as a function of illumination intensity. . . . .	96
6.4	Ideality factor and saturation current as a function of illumination intensity. . . . .	97
6.5	Measured and fitted I-V curves of Back contact Back junction silicon solar cell at two spectral conditions. . . . .	98
6.6	Optical absorption coefficients of various semiconductor materials . . . . .	99
6.7	Transmission spectra for long pass filters . . . . .	100
6.8	I-V characteristics for a BC-BJ Si solar cell under different spectral conditions . . . . .	100
6.9	Spectral response of a Silicon solar cell. . . . .	101
6.10	Illumination I-V curves for a CTJ solar cell under different solar spectral conditions . . . . .	102

# Chapter 1

## Introduction

One of the biggest challenges the world faces today is the increasing demand for energy. This has been partly driven by the increasing population and the level of economic activity globally. The global energy consumption stood at  $13 TW$  per year by 2005 and this rate is expected to increase to  $30 TW$  by 2050 [1]. Figure 1.1 [2] shows the growth of worldwide primary energy consumption from 1988 to 2013.

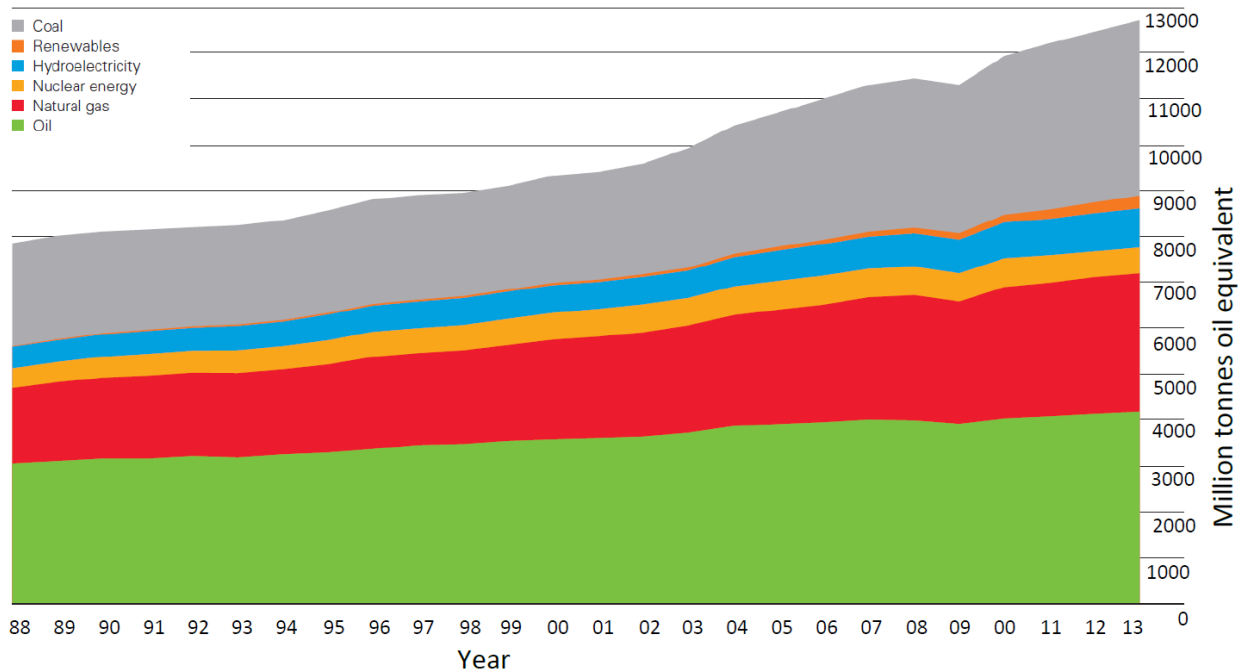


Figure 1.1: World primary energy consumption since 1988. The worldwide primary energy consumption grew by in 2013.

Satisfying this global energy demand is one the biggest challenges confronting mankind and must be addressed to satisfy the current levels of economic development. Fossil fuels, which are currently the major sources of energy, are expected to fall short of this demand [1]. Besides, their continued use has impacted negatively on the envi-

ronment through pollution by production of greenhouse gases and other waste products that affect all living organisms. According to the Intergovernmental Panel on Climate Change (IPCC) [3], global atmospheric concentration of green house gases especially carbon dioxide, methane and nitrous oxide have increased greatly as a result of human activities, with the primary source of the increased atmospheric concentration of carbon dioxide being attributed to fossil fuel usage. The increase in the levels of concentration of the green house gases is most likely the leading cause for most of the observed temperature increase since the middle of the 20<sup>th</sup> century. This therefore calls for alternative sources of energy which are clean and environmentally friendly so as to address the global challenges of energy security, climate change and sustainable development [3, 4]. The focus on renewable energy has grown, with various renewable energy sources experiencing a significant growth in investments and installed capacity. Global demand for renewable energy is rising and represents a rapidly rising share of energy supply in a growing number of countries such as China, Germany and Denmark. An estimated 19% of global final energy consumption by end of 2011 came from renewable energy sources [5]. The potential of different sources of renewable energy varies and if availability is taken into account, solar energy is by far, the most abundant and largest renewable energy source [6]. The energy supply from the sun to the surface of the earth exceeds by far the global energy consumption and if 0.16% of the land mass on earth were to be covered with 10% efficient solar conversion systems, it would provide energy sufficient to cover the annual global power demand [1]. Amongst various technologies of harvesting solar energy, solar photovoltaics (PV) provides an elegant method where the solar irradiation is directly converted into electricity. The other technologies of solar energy harvesting are concentrating solar power (CSP) and solar thermal collectors for heating and cooling (SHC). CSP systems use concentrated solar radiation as a high temperature energy source to produce electrical power and drive chemical reactions while SHC systems use the thermal energy directly from the sun to heat or cool domestic water or building spaces.

The concept of photovoltaic effect was discovered as far back as 1839 by a French scientist Edmund Becquerel when he observed that an electric current was produced by light incident on a silver coated platinum electrode immersed in an electrolyte [7]. However, significant development in solar PV began with the invention and demonstration of the silicon single crystal solar cell with 6% efficiency in 1954 [8]. A fundamental understanding of the performance of solar cells was consequently reached in 1961 by Shockley and Queisser, who determined the maximum theoretical light conversion efficiency (detailed balance limit of efficiency) of semiconductor solar cells [9]. Since then, significant progress was made in research and development that saw significant improvement in silicon solar cell efficiencies over time, with efficiencies reaching 15% over the following few years [10, 11]. The major viable application for solar cells at the time was power

supply for space applications. Today, solar PV energy conversion is used for both space and terrestrial energy generation. A major breakthrough for PV occurred in 1973 with the setting up of various publicly funded research and development institutions that ushered in the modern era of photovoltaics and gave a new sense of urgency to research and application of photovoltaics especially for terrestrial applications. This was mainly driven by the energy crisis in 1973 as alternative and stable energy sources were needed to absorb the oil embargo shock. This resulted in improvements in cell and module efficiency that saw reductions in cost of the complete system as solar cells moved from pilot scale to semi-automated production. Today, the need for much more extensive use of solar cells in terrestrial applications has resulted in the continued growth of the PV industry at an annual rate approximately of 35 – 40% , with silicon based solar cells contributing ~ 90% of the PV market [12], and major programs in the U.S, Japan and Europe are rapidly accelerating the implementation of stand alone and building integrated PV as well as grid tied PV systems.

Though silicon based solar cells have dominated and still continue to dominate the PV market today, several other cell types and technologies have entered the market and have added diversity in potential applications and offered alternate paths to increasing efficiency. The evolution of world record efficiencies of research laboratory solar cells is shown in Figure 1.2 [13].

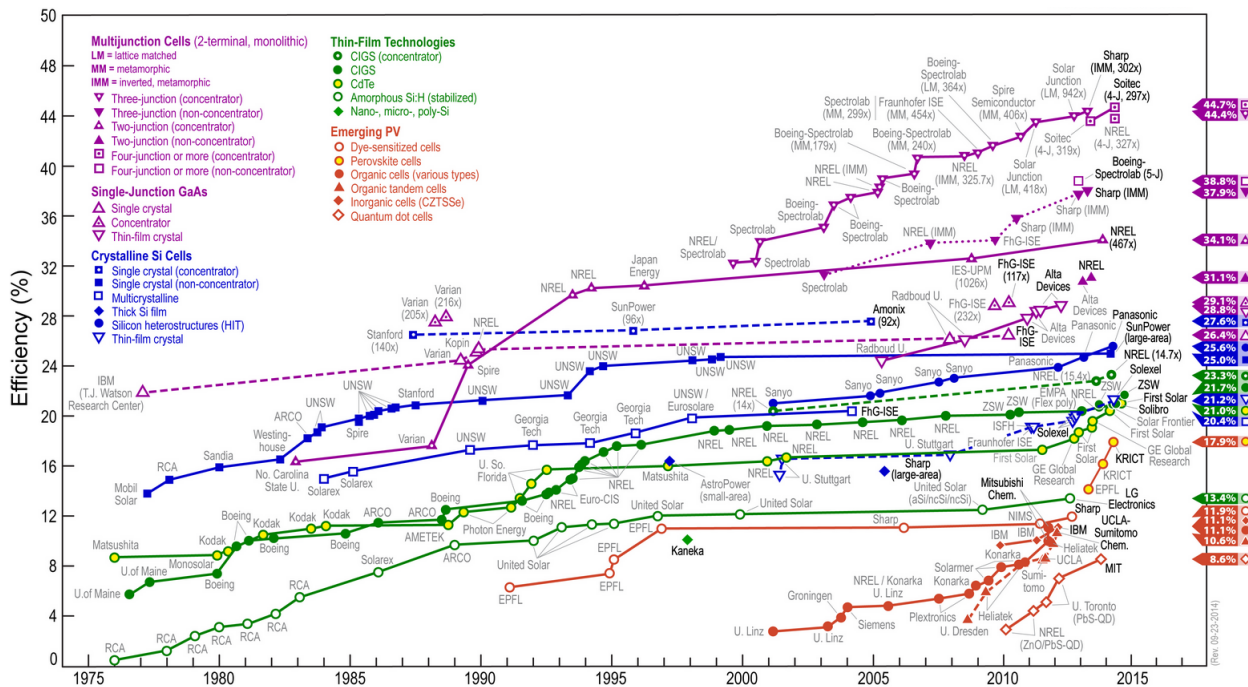


Figure 1.2: Record efficiencies for various types of research solar cells since 1975.

The world cumulative PV operating capacity surpassed the 100 GW installed electrical power mark in 2012 [5, 14] as shown in Figure 1.3 [5]. This was made possible due to a combination of economic incentive schemes, market development and technology cost

reduction. However, compared to conventional sources of energy such as hydro, the cost of PV energy is still high partly due to the high cost of production and low conversion efficiencies.

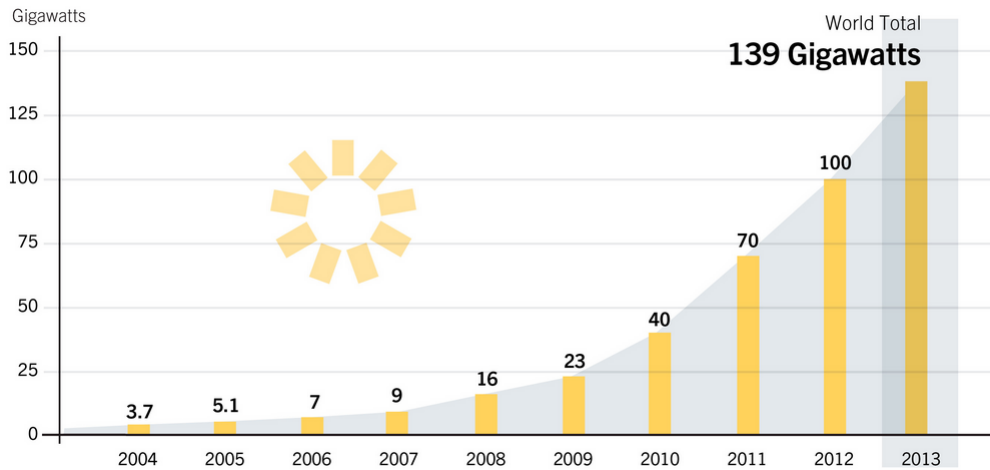


Figure 1.3: Cummulative installed global solar PV power from 2004 to 2013

In order to increase the use of terrestrial solar photovoltaics and successful growth of the PV industry, there is a need for significant reductions in levelized costs of electricity from PV and a move away from economic incentives and subsidies as these are not sustainable. Significant lowering of the levelized costs of electricity from PV can be achieved by a combination of a reduction in the semiconductor material consumption and increasing the solar cell efficiencies [15]. Reducing the amount of semiconductor material can be attained by using thin film based technologies and concentrating systems using optics to direct light towards smaller area solar cells while improvement in cell efficiencies calls for a clear understanding of the performance limiting factors. The variation in performance can be caused by spatial inhomogeneities in the semiconductor starting material itself or can be introduced in the material during the various device processing steps. The distributed variation of material properties or areas containing defects can cause the performance of solar cell devices to decrease. It is therefore important to investigate cell device and performance properties non destructively so as to identify any potential weak spots or spatial non-uniformities. The performance and hence the conversion efficiency of a PV device depends on the efficiency of every point of the photo-active surface. Improvements in cell design and construction are normally based on finding ways of improving cell efficiencies. However, though overall efficiency measurements may be important in assessing cell performance, it may be difficult from such measurements to deduce localised performance on the cell area or to determine the origin of non-uniformities that may be observed during cell test or operation [16]. A point-by-point characterisation of the photo-active surface is therefore a powerful tool for an accurate and effective description of the device. This can be done through a

point-by-point irradiation of the surface by means of a highly focused photon beam and measuring the induced current as a function of position to obtain a photo-response map. This allows spatial mapping of conversion efficiency and detection of local active defects which could be due to presence of impurities, processing heterogeneities or sites of excessive recombination such as grain boundaries and dislocations.

## 1.1 Concentrating photovoltaics

Optical concentration has been explored since the earliest days of the PV industry, as a means of increasing cell efficiency and leveraging the high cost of solar PV energy systems [17, 18]. Early concentrator cells were basically flat plate cells re-designed for higher current density but, designs developed specifically for concentrator applications later emerged. In Concentrating Photovoltaics (CPV), a large area broad spectral range of sunlight is focused onto small highly efficient solar cells using optical devices as illustrated in Figure 1.4.

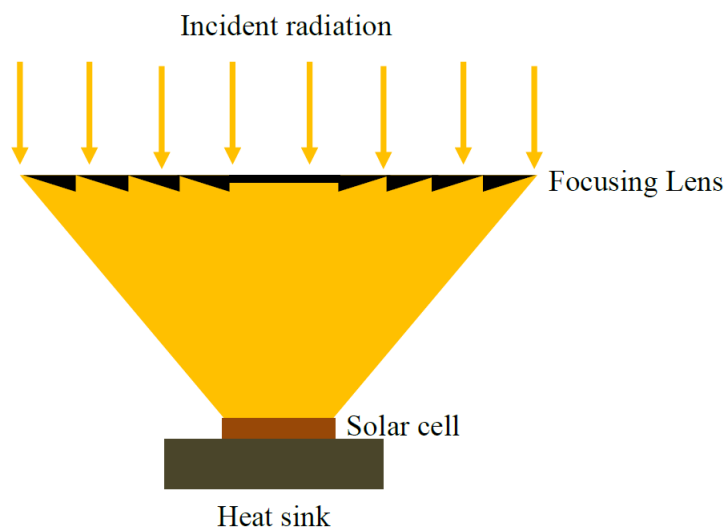


Figure 1.4: Principle of a CPV solar cell system using a Fresnel lens.

By concentrating sunlight, CPV technologies use less photovoltaic materials compared to conventional PV modules. The area of the solar cell receiver is reduced by the level of concentration while at the same time, the intensity is increased by the same level [19]. The cost of a large cell surface is replaced by the cost of the cheaper optics and other auxiliary components that are used to capture the incident radiation and focus it onto a smaller area solar cell, making it economically viable to use expensive and high quality single and multijunction solar cells. The optical system comprises of materials that are relatively inexpensive such as mirrors and plastic lenses. Concentrating light, however, requires direct sunlight rather than diffuse light, which limits CPVs to clear, sunny locations. It also means that, in most instances, tracking the sun is required to focus light

on to a solar cell throughout the day and year. This therefore means that achieving higher concentration ratios requires complex tracking systems and high precision control mechanisms. Sun tracking, however, increases the daily energy production of the CPV above that of non-tracking flat plate PV systems. The deployment of solar technologies is influenced significantly by local solar resources. Shown in Figure 1.5 [20] are regions around the world that experience a high degree of direct insolation.

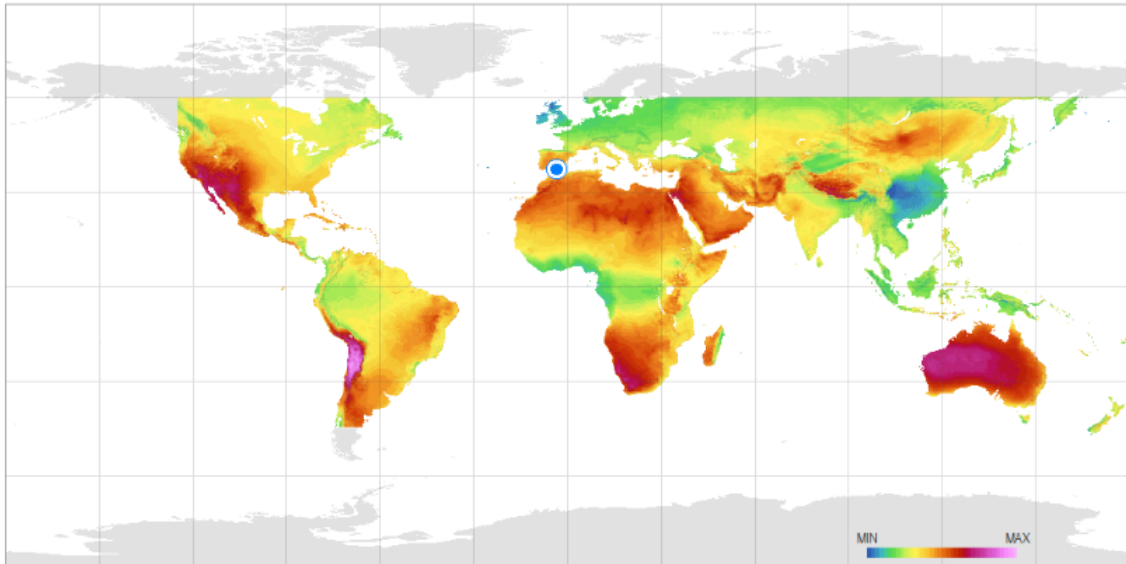


Figure 1.5: World map showing long term average levels of Direct Normal Irradiance (DNI).

Regions with very high DNI offer better locations for CPV deployment compared to conventional PV systems. These regions also have the highest available solar resource overall [21]. In the early days of the CPV technology, it was feared that the percentage of DNI was considerably lower than the solar resource available for flat plate systems, that make use of global radiation.

## 1.2 Thesis objectives and outline

### 1.2.1 Thesis objectives

The increased deployment of CPV systems worldwide and the expected growth of this field in Africa has opened up an increasing scope in the area of characterisation of CPV devices. High concentrator photovoltaic (HCPV) systems typically use multijunction solar cells while medium and low concentrator photovoltaic (LCPV) systems use either standard or specifically designed crystalline Si solar cells. The solar cells of a CPV module, when under concentration, operate under carefully optimized conditions in terms of the optical, electrical and thermal sub-systems of the module. Deviation from the



optimum conditions can lead to device degradation and sometimes premature failure. In addition, studies on the reliability of CPV cells operating in modules under outdoor conditions has not been tested to the same extent as compared to standard PV systems. It is therefore, essential to characterise concentrator solar cells with respect to photo-response and device parameter uniformity under solar spectral conditions before and after exposure to concentrated sunlight for extended periods of time in order to form a basis for quality control and maintenance. The objectives of this research were:

- To identify and characterise the current reducing features on CPV cells through photo-response mapping
- To determine performance and device parameters of CPV cells through parameter extraction
- To study the effect of change in the solar spectral content and intensity on the I-V parameters of spot illuminated solar cells

The above objectives were achieved by carrying out indoor measurements with laser sources as well as outdoor measurements under the solar illumination using the LBIC system that was designed and constructed. These measurements were taken using standard solar cells as well as concentrating solar cell devices at the Outdoor Research Facility (ORF), of the Department of Physics, Nelson Mandela Metropolitan University.

### **1.2.2 Content outline**

In Chapter 2, a brief introduction to solar cell device physics is given where the different recombination mechanisms that take place in solar cell devices are explained as well as performance and device parameters. Solar cell equivalent circuit models based on the single and double diode equations are presented. Concentrator solar cells are introduced and their classification based on the level of concentration presented. Silicon concentrator solar cells for use in low to medium concentrator systems and multijunction solar cells for use in high concentrating photovoltaic systems are also discussed.

Principles of LBIC and an overview of systems developed over time as well as system characterisation are given in Chapter 3. The Chapter also presents the LBIC scanning system that was developed for indoor and outdoor measurements in this study. The hardware and software development of the characterisation tool and experimental set up are outlined in detail. Results from a multi-crystalline silicon solar cell obtained using the system are presented and discussed.

In Chapter 4, an interval division algorithm for parameter extraction is presented. The Chapter discusses the fitting procedure in detail and its implementation in Labview.

Results of the parameter extraction procedure applied to dark and illuminated I-V measurements from a mc-Si solar cell are discussed. Parameter maps obtained by application of the algorithm to LBIC measurements are discussed to understand the effect of non-uniformity and local defects on device performance.

Chapter 5 discusses characterisation of the Back contact Back junction silicon concentrator solar cell and the InGaP/InGaAs/Ge concentrating triple junction (CTJ) solar cell in terms of photo-response mapping and parameter extraction. Photo-response maps obtained from Light Beam Induced Current and Solar-Light Beam Induced Current measurements are presented to map carrier generation uniformity over the cell surface and to identify localised current reducing features on or within the device. Parameter extraction from dark and illuminated I-V characteristics are presented and discussed. The parameters give a general idea about the functioning and or performance of the devices. Parameter maps are also presented to discuss local variation in device parameters that affects the overall performance of the devices.

In Chapter 6, the effect of change in the spectral content and intensity of the beam probe on the device and performance parameters of spot illuminated solar cells is discussed while Chapter 7 summarises and concludes the main results of this work and proposes some work for future investigations.

# Chapter 2

## Basics of solar cells and concentrator photovoltaic systems

### 2.1 Introduction

A solar cell is a semiconductor device that is designed and constructed to efficiently absorb and convert light into electrical energy through the photovoltaic effect, a physical phenomenon that establishes a voltage across a p-n junction (the interface between the n and p-type regions) by the absorption of photons. The fraction of solar energy that is converted into electrical energy is quantified by the efficiency of the solar cell, which in principle, depends on the generation and recombination of the charge carriers when incident photons are absorbed. The absorption of the incident photons in the semiconductor material that forms a p-n junction results in generation of charge carriers (electrons and holes) that are subsequently separated by the built-in electric field and collected at the terminals of the junction. Electrons are collected in the n-type region, and holes in the p-type region, resulting in the carrier separation and voltage generation across the device. The separated charge carriers flow through an external load connected to the terminals of the solar cell to generate electrical current. This chapter provides an overview of the fundamental operating principles and device physics of solar cells so as to understand the basics for PV device operation. The basic principles of carrier generation and recombination mechanisms are discussed as well as semiconductor diode characteristics. The current-voltage (I-V) characteristics and performance parameters as well the effect of parasitic resistance and temperature are discussed. Finally, an overview of concentrator solar cells for low and high concentrator photovoltaic systems based on silicon and III-V multijunction solar cells are briefly tackled.

### 2.1.1 Solar cells and the solar spectrum

Standard spectra are needed in solar cell research and development because the actual spectrum impinging on a solar cell in operation varies with location and time of the day as well as due to weather and seasonal changes. In order to evaluate the relative performance of solar cells and photovoltaic modules, reference standard solar spectra are needed so as to ensure that the solar cells and modules are exposed to the same agreed upon spectrum. The American Society for Testing and Materials (ASTM), the International Electrochemical Commission (IEC) and the International Standards Organisation (ISO) provide the standard spectra for PV performance and testing conditions [22]. Various standard reference spectra are defined depending on the type and application of the solar cell devices i.e. whether flat plate or concentrator cells or whether they are meant for terrestrial or space applications. For space applications, the AM0 is used while for terrestrial applications, two spectra are defined, one for flat plate modules and the other for concentrator solar cells applications. The AM1.5G, with an integrated power density of  $1000 \text{ Wm}^{-2}$  is used for flat plate modules while the AM1.5D is used mainly for concentrator solar cells. This spectra has an integrated irradiance of  $\sim 900 \text{ Wm}^{-2}$ . Shown in Figure 2.1 [23] are the different spectra in common use.

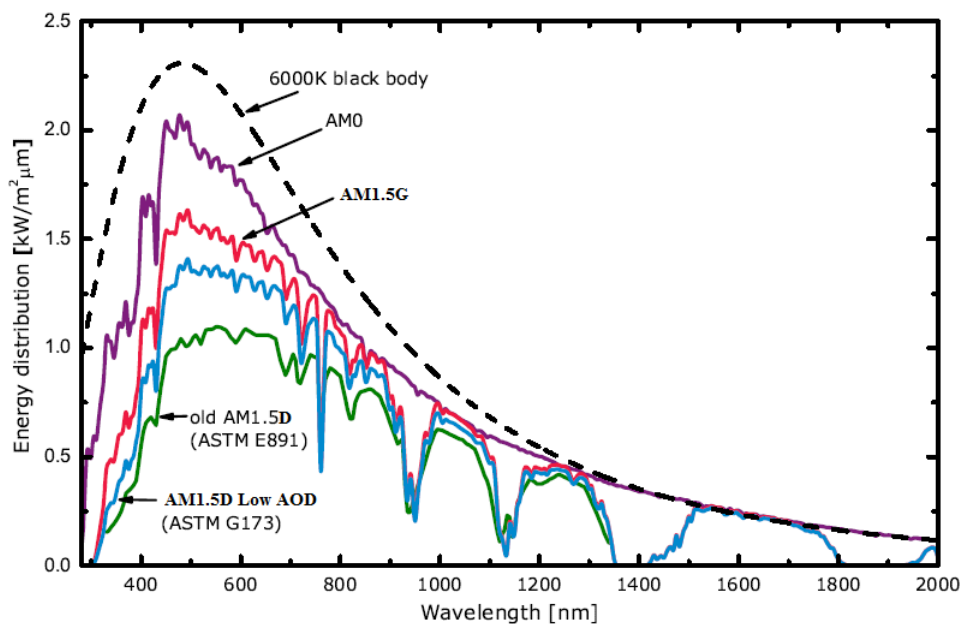


Figure 2.1: Solar spectra for space and terrestrial use.

Due to smaller acceptance angles, concentrator solar cells mainly absorb the direct solar irradiation. In regions of high annual direct normal irradiation, the AM1.5D may not be representative of the prevailing conditions, yet it is in such regions where concentrator solar cells are likely to be deployed [24]. As a result, a low aerosol optical depth (AOD) AM1.5D spectrum shown in Figure 2.1 was proposed in 1999 and is cur-

rently being used for concentrator solar cell measurements. This spectrum is seen as being more representative of the spectral conditions for concentrator photovoltaic (CPV) applications [25].

## 2.2 Device Physics

Semiconductor solar cells use p-n semiconductor diodes to absorb and convert light energy into electrical energy. A p-n semiconductor diode is formed when an n-type semiconductor is brought into contact with a p-type semiconductor to form a metallurgical junction. At this junction, holes which are the majority charge carriers in the p-type semiconductor diffuse across the junction into the n-type semiconductor leaving behind exposed negative charged ions, that are fixed in the crystal lattice and unable to move. Similarly, electrons which are the majority charge carriers in the n-type semiconductor diffuse into the p-type semiconductor leaving behind immobile positively charged ions. As a result of exposure of the oppositely charged ions, a built-in electric field develops, which limits the diffusion of holes and electrons. The built-in electric field leads to a built in electrostatic potential difference across the junction given by [26] .

$$V_{bi} = \frac{kT}{q} \ln \left( \frac{N_A N_D}{n_i^2} \right) \quad (2.1)$$

where  $N_A$  and  $N_D$  are the acceptor and donor concentrations respectively,  $n_i$  is the intrinsic carrier concentration,  $T$  is the absolute temperature,  $k$  is Boltzmann constant while  $q$  is the magnitude of the electronic charge. In thermal equilibrium, the charge carrier drift and diffusion currents balance each and so the net current is zero. The region between the exposed donor and acceptor ions is called the space charge region. This region is effectively depleted of both the holes and electrons and as thus, it is also commonly known as the depletion region. On either side of the depletion region away from the junction, there is no significant built-in electric field in thermal equilibrium. These regions are called quasi neutral regions. The more heavily doped quasi neutral region is called the emitter while the lightly doped region is called the base. The emitter and the base (absorber) have opposite dopant species. Absorption mainly occurs in the base as the emitter is usually very thin [27]. If a solar cell is illuminated, the photo-generated minority carriers will be separated by the built-in electric field at the p-n junction, i.e. electrons to the n-type material and holes to the p-type material where they become majority carriers. This charge separation causes current to flow across the junction (photo-generated current) and a voltage build up across the solar cell (photo-voltage) that forward biases the p-n junction.

When light is incident on a solar cell, it may be reflected, transmitted or absorbed. Pho-

tons with energy equal to or greater than the band gap energy of the semiconductor material will be absorbed leading to generation of charge carriers (electron-hole pairs). However, since electrons and holes normally occupy energy levels at the bottom of the conduction and valence bands, respectively, the excess energy received by the electron-hole pairs will be lost to the material lattice, thus increasing the energy of the lattice vibrations, which results in increase in temperature of the semiconductor. Photons with energy less than the band gap are transmitted through the material and do not contribute to charge carrier generation. The rate of carrier generation,  $G(x)$ , i.e the number of electron-hole pairs per second per  $cm^3$  as a function of position below the surface of the semiconductor material,  $x$ , is given by [27]

$$G(x) = (1 - s) \int (1 - r(\lambda)) f(\lambda) \alpha(\lambda) e^{-\alpha x} d\lambda \quad (2.2)$$

where  $s$  is the grid shadowing factor,  $r(\lambda)$  is the reflectance,  $f(\lambda)$  is the photon flux and  $\alpha(\lambda)$  is the absorption coefficient.

### 2.2.1 Bulk recombination

When a semiconductor is illuminated, it is no longer in thermal equilibrium due to the excess carrier pairs created by photo-generation. The photo-generated carriers tend to relax back to their equilibrium values through recombination. The rate of recombination of the excess charge carriers,  $\Delta n$ , is given by

$$\left( \frac{d\Delta n}{dt} \right)_{rec} = -\frac{\Delta n}{\tau} \quad (2.3)$$

where  $\tau$  is the carrier lifetime i.e. the average time which a carrier can spend in an excited state after electron-hole generation before it recombines. Thus smaller carrier lifetimes correspond to high recombination rates. The three basic types of recombination mechanisms which occur within the bulk of the semiconductor are radiative recombination (band to band), Auger recombination and the Shockley-Read-Hall recombination (recombination through traps or defects in the forbidden gap). These three recombination mechanisms differ in the way the excess carrier energy is dispersed, being mediated by photons, electrons and phonons respectively but may occur concurrently in which case the net recombination rate will be the sum of the individual recombination rates. Auger and radiative recombination mechanisms are also classified as intrinsic recombination mechanisms while the Shockley-Read-Hall is an extrinsic recombination mechanism. Intrinsic recombination mechanisms are always present in semiconductor materials even in ideal crystals.

### 2.2.1.1 Radiative recombination

Radiative recombination is the reverse process of optical absorption and is thus an inherent property of the semiconductor material. It is typically dominant in direct bandgap semiconductors (which are common among the III-V compounds) than in indirect types. In this process, an electron from the conduction band directly combines with a hole in the valence band, with the energy difference between the two states being released as a photon. The emitted photons may be absorbed again by the semiconductor material, through a process called photon recycling. However, such relatively low-energy photons are only weakly absorbed, and hence they are only reabsorbed to a significant extent if there is excellent light-trapping present. In indirect band gap materials such as silicon, some of the energy difference between the two states is shared with a phonon so as to conserve both momentum and energy. This makes radiative recombination inherently less probable in indirect semiconductors. The net radiative recombination rate,  $U_{rad}$ , is given by [26, 27]

$$U_{rad} = B (np - n_i^2) \quad (2.4)$$

where  $B$  is the radiative recombination coefficient for a given semiconductor, while  $n$  and  $p$  are electron and hole concentrations respectively. In an n-type material for low injection i.e when the excess charge carriers  $\Delta p = \Delta n$  are fewer than the majority charge carriers, the net radiative recombination rate can be expressed as [27]

$$U_{rad} \approx \frac{\Delta p}{\tau_{rad,p}} \quad (2.5)$$

where  $\tau_{rad,p} = \frac{1}{n_o B}$  is the minority carrier lifetime,  $n_o$  is the equilibrium electron concentration,  $\Delta p = p - p_o$  is the excess hole concentration and  $p_o$  is the equilibrium hole concentration. The expression for the p-type material can be similarly written.

### 2.2.1.2 Auger recombination

Auger recombination is an intrinsic recombination process that involves three particle interaction where an electron and a hole recombine, but instead of emitting the energy as heat or as a photon, the energy is transferred to a third carrier, an electron in the conduction band (or a hole in the valence band). The electron (or hole) then relaxes thermally to the conduction (or valence) band edge by emitting phonons. This process is intrinsic to all semiconductors and occurs regardless of the presence of any material imperfections. It is most effective when there is a high density of carriers in one of the bands or both i.e. when heavily doped or under high injection conditions. The net

recombination rate due to Auger recombination process is [27, 28]

$$U_{aug} = (A_n n + A_p p) (np - n_i^2) \quad (2.6)$$

where  $A_n, A_p$  are the Auger recombination rates for  $n$  and  $p$  materials respectively. The first term is dominant in a p-type material while the second term is dominant for an n-type material. Both terms are, however, important for a material in high level injection [28]. In an n-type material under low injection and under the assumption that  $A_n$  and  $A_p$  are comparable in magnitude, the net Auger recombination rate is given by [27]

$$U_{aug} \approx \frac{\Delta p}{\tau_{aug,p}} \quad (2.7)$$

where  $\tau_{aug,p} = \frac{1}{A_n n_0^2}$  is the hole lifetime in n-type material. Similarly, the expression for electron lifetime in p-type material is obtained.  $\tau_{aug}$  shows a stronger dependence on the injection level compared to  $\tau_{rad}$  and so Auger recombination will become the dominant mode of recombination for semiconductor materials under high injection levels such as concentrator solar cells, or for high dopant densities such as heavily doped emitter regions of silicon solar cells.

### 2.2.1.3 Recombination through defect levels

The presence of defects within a semiconductor crystal (from impurities or crystallographic imperfections such as dislocations and interstitials) produces discrete energy levels within the bandgap. Some of energy levels lie deep in the middle of the band gap. These defect levels or traps (introduced intentionally e.g. through doping or unintentionally) greatly facilitate recombination through a two-step process: a free electron from the conduction band first relaxes to the defect level, the electron then moves to the valence band where it recombines with a hole or a hole can jump up to the same defect level before the electron is thermally re-emitted into the conduction band. This extrinsic recombination mechanism strongly depends on the concentration of the impurities. The net recombination rate per unit volume per second through a single level trap (SLT) within the forbidden gap is given by the Shockley Read Hall (SRH) recombination equation [29, 30]

$$U_{SRH} = \frac{np - n_i^2}{\tau_{po}(n + n_1) + \tau_{no}(p + p_1)} \quad (2.8)$$

where  $\tau_{po} = \frac{1}{\sigma_p \nu_{th} N_t}$  and  $\tau_{no} = \frac{1}{\sigma_n \nu_{th} N_t}$  are the fundamental hole and electron lifetimes while  $\nu_{th}$  is the thermal velocity of charge carriers,  $N_t$  the density of recombination traps and  $\sigma_p$  and  $\sigma_n$  are the capture cross-sections for the specific trap,  $n_1$  is the electron density when the electron Fermi level is equal to the trap level while  $p_1$  is the hole density when the hole Fermi level is equal to the trap level.  $n_1$  and  $p_1$  introduce a dependence of the



recombination rate on the energy level of the traps and are defined as [30]

$$n_1 = n_i \exp\left(\frac{E_t - E_i}{kT}\right) \quad (2.9)$$

$$p_1 = n_i \exp\left(\frac{E_i - E_t}{kT}\right) \quad (2.10)$$

where  $E_i$  is the intrinsic Fermi level and  $E_t$  is the energy level of the trap. If carrier trapping is negligible i.e  $\Delta n = \Delta p$ , the SRH recombination lifetime,  $\tau_{SRH}$  can be expressed as [31, 32]

$$\tau_{SRH} = \frac{\tau_{no}(p_o + p_1 + \Delta n) + \tau_{po}(n_o + n_1 + \Delta n)}{n_o + p_o + \Delta n} \quad (2.11)$$

From Equation 2.11, it can be seen that the SRH lifetime is a function of the carrier injection level and the dopant density (through  $n_o$  and  $p_o$ ), as well as defect specific properties such as the concentration of traps, their energy level and their capture cross-sections. It also shows that traps with energies close to the centre of the bandgap (deep defects) are the most effective recombination centres. For a very large number of excess holes and electrons, the recombination rate is high but the carrier lifetime is longer. This is particularly important in the base region of solar cells, especially concentrator solar cells since the base region is the least doped.

## 2.2.2 Surface recombination

Semiconductor device surfaces and interfaces usually contain a large number of recombination centres due to the abrupt termination of the crystal lattice that leaves behind a large number of electrically active dangling bonds. As a result, surfaces and interfaces are more likely to contain impurities since they are exposed during the device fabrication process, leading to the presence of traps within the forbidden gap at the surface or interface. Recombination can therefore occur at solar cell surfaces and interfaces by the same mechanism as with the bulk traps. For a single defect at the surface, the net recombination rate is given by [33]

$$U_s = \frac{n_s p_s - n_i^2}{\frac{n_s + n_1}{S_{po}} + \frac{p_s + p_1}{S_{no}}} \quad (2.12)$$

where  $n_s$  and  $p_s$  are the concentrations of electrons and holes, respectively, at the surface,  $S_{po} = \sigma_p \nu_{th} N_{ts}$  and  $S_{no} = \sigma_n \nu_{th} N_{ts}$  where  $N_{ts}$  is the density of surface states per unit area  $\sigma_p$  and  $\sigma_s$  are the capture cross-sections for the specific defects. Generally, defect density is so high that the defect levels can be considered to be continuously distributed throughout the bandgap, and both their density and capture cross-sections will

be dependent on their energy level. The net surface recombination velocity  $S_{eff}$  is given by

$$S_{eff} = \frac{U_s}{\Delta n_s} \quad (2.13)$$

Surface recombination velocity is typically used for quantifying surface recombination processes, it affects the dark saturation current and the quantum efficiency of solar cells. For optimal operation of solar cell devices, surface recombination is minimised by passivation of the surface or introduction of a window layer that prevents minority carriers from reaching the surface. In addition, doping of the semiconductor surface minimises the excess concentration of minority carriers at the surface and hence reduces the recombination rate as seen from Equation 2.13.

In most practical cases two or more of the bulk recombination mechanisms and surface recombination described above may occur in a given sample at a given injection level and can be considered to occur independently. For independent processes, the net recombination rate is the sum of the contributions from individual mechanisms, resulting in an effective carrier lifetime  $\tau_{eff}$ , given by

$$\tau_{eff} = \left( \frac{1}{\tau_{rad}} + \frac{1}{\tau_{aug}} + \frac{1}{\tau_{SRH}} \right) + \frac{1}{\tau_{surface}} \quad (2.14)$$

or

$$\tau_{eff} = \frac{1}{\tau_{bulk}} + \frac{1}{\tau_{surface}} \quad (2.15)$$

High bulk recombination rates limit the open circuit voltage and reduce the fill-factor in low efficiency devices [28] and so should be minimised to improve the performance of the device. In addition, injection level dependent surface recombination rates have also been shown to reduce solar cell efficiency significantly [34].

### 2.2.3 Semiconductor diode characteristics

When an n-type material and p-type material are brought into contact to form a metallurgical junction, an electric field is set up that opposes the diffusion of holes and electrons until equilibrium is established. When an external voltage,  $V$ , is applied, it can be shown that the concentration of minority charge carriers at the edges of the depletion region is given by

$$p_n(x_n) = \frac{n_i^2}{N_D} e^{\frac{qV}{kT}} \quad (2.16)$$

$$n_p(x_p) = \frac{n_i^2}{N_A} e^{\frac{qV}{kT}} \quad (2.17)$$

where  $p_n(x_n)$  and  $n_p(x_p)$  are the concentrations of holes and electrons at the edge of the depletion region of the n and p-type materials respectively while  $x_n$  and  $x_p$  locate the

edges of the depletion region in the  $n$  and  $p$ -type materials respectively. The concentration of minority carriers at the edge of the depletion region is thus seen to increase exponentially with applied voltage. If the quasi neutral regions are uniformly doped and the majority carrier currents are small, the minority carriers will flow mainly by diffusion since the electric field is negligible in this region. Using the minority carrier diffusion equations and applying appropriate boundary conditions, it can be shown that the total current (due to holes and electrons) throughout the semiconductor diode is given by

$$I = I_o \left( e^{\frac{qV}{kT}} - 1 \right) \quad (2.18)$$

where

$$I_o = A \left( \frac{qD_e n_i^2}{L_e N_A} + \frac{qD_h n_i^2}{L_h N_D} \right) \quad (2.19)$$

is the saturation current,  $A$  is the cross-sectional area of the diode,  $D_e$  and  $D_h$  are the electron and hole diffusion coefficients, respectively, which depend on the mobility of the carriers through the semiconductor material while  $L_e$  and  $L_h$  are the minority carrier diffusion lengths for electrons and holes, respectively. The diffusion length, which should be long enough to ensure that the generated carriers reach the solar cell contacts before they recombine, is related to the diffusion coefficient and the minority carrier lifetime through the relation  $L = \sqrt{D\tau}$ . Equation 2.18 gives the ideal diode equation in the dark. However, practical solar cells do not obey the ideal diode equation. The non-ideal diode equation is approximated by the introduction of an ideality factor  $n$  in Equation 2.18 to give

$$I = I_o \left( e^{\frac{qV}{nkT}} - 1 \right) \quad (2.20)$$

The ideality factor is a measure of the quality of the junction and the type of recombination in the solar cell. If recombination is dominated by minority carrier recombination in the quasi neutral regions, the ideality factor has a value close to 1. However, when other recombination mechanisms occur,  $n$  can have a value close to 2. Under illumination, it can be shown that the current-voltage (I-V) characteristics of a p-n semiconductor diode are given by

$$I = I_o \left( e^{\frac{qV}{nkT}} - 1 \right) - I_L \quad (2.21)$$

where

$$I_L = qAG(L_e + W + L_h) \quad (2.22)$$

is the light generated current,  $W$  is the width of the depletion region. Equation 2.22 shows that only charge carriers generated within the depletion region and within one diffusion length on either side of the depletion region contribute to the light generated current. Simulated dark and light I-V characteristics are shown in Figure 2.2.

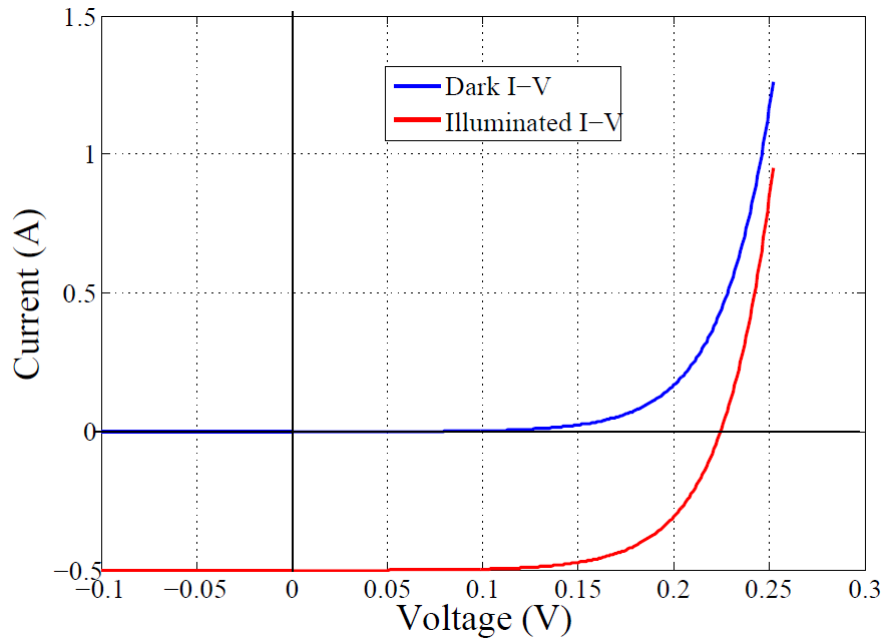


Figure 2.2: I-V characteristics of a diode in dark and under illumination.

The light diode I-V characteristic is identical to the dark I-V characteristic but is shifted down by the photogenerated current  $I_L$ .

### 2.2.4 Solar cell parameters

When a solar cell is illuminated, the incident photons are absorbed by the solar cell to generate a photo-current, which is superimposed upon the dark current.

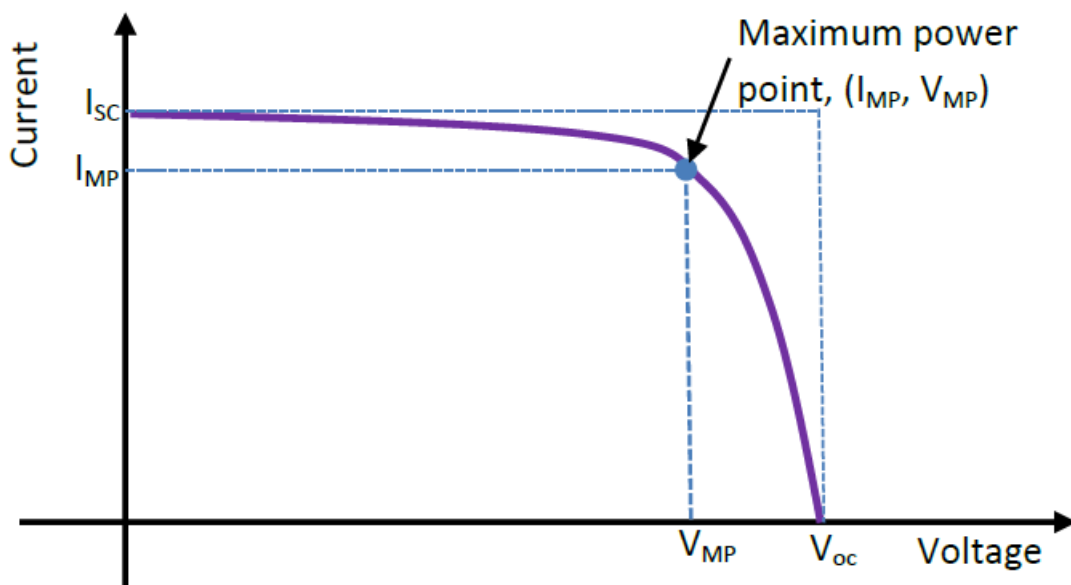


Figure 2.3: The Light I-V characteristic of a solar cell in the first quadrant showing the solar cell performance parameters.

The solar cell characteristics can then be modelled by a superposition of light-induced current and the I-V characteristic of the p-n junction. From the light I-V curve, solar cell performance parameters such as the open circuit voltage ( $V_{oc}$ ), short circuit current ( $I_{sc}$ ) can be obtained. These and other figures of merit are illustrated in Figure 2.3.

#### 2.2.4.1 Open circuit voltage

At open circuit voltage, the output current is zero. Hence Equation 2.21 can be modified to yield Equation 2.23

$$V_{oc} = \frac{nkT}{q} \ln \left( \frac{I_L}{I_o} + 1 \right) \quad (2.23)$$

Equation 2.23 shows that  $V_{oc}$  increases with decrease in  $I_o$  which is determined by the carrier recombination in the quasi neutral regions as well as the depletion region. The carrier recombination in both regions depends on the intrinsic carrier concentration,  $n_i$ , which is a function of temperature i.e.

$$n_i = 2 \left( m_n^* m_p^* \right)^{\frac{3}{4}} \left( \frac{2\pi kT}{h^2} \right)^{\frac{3}{2}} e^{-\frac{E_G}{2kT}} \quad (2.24)$$

where  $m_n^*$  and  $m_p^*$  are the effective masses of electrons and holes, respectively,  $E_G$  is the band gap while  $h$  is Planck's constant. The effective masses weakly depend on temperature while the band gap varies with temperature according to Equation 2.25

$$E_G(T) = E_G(0) - \frac{\alpha T^2}{\beta + T} \quad (2.25)$$

where  $\alpha$  and  $\beta$  are constants specific to the semiconductor. Thus increase in temperature increases  $n_i$  which in turn increases in  $I_o$  thus leading to a decrease in  $V_{oc}$ .

#### 2.2.4.2 Short circuit current

Current through a solar cell when the voltage across the cell is zero is the short circuit current, ( $I_{sc}$ ). It is the maximum current that can be extracted from the solar cell and depends on the photon flux density incident on the solar cell, which is determined by the spectrum of the incident light. Ideally  $I_{sc}$  is equal to the light generated current  $I_L$ . Low energy band gap and high diffusion length of the minority carriers are favourable for high short circuit current. Short circuit current is also determined by the cell's quantum efficiency, which is the fraction of the incident photons that produce electron-hole pairs at a given wavelength. Short circuit current is weakly temperature-dependent, it increases slightly with increase in temperature.

### 2.2.4.3 Maximum power output

The power output of the solar cell is given by

$$P = IV \quad (2.26)$$

and is maximum at the maximum power point defined by  $I_{mp}$  and  $V_{mp}$ , the current and voltage, respectively, at which  $P = P_{max}$ , the maximum power output from the solar cell. The maximum power point defines the largest rectangle for any point on the I-V curve.  $P_{max}$  is given by

$$P_{max} = I_{mp}V_{mp} \quad (2.27)$$

### 2.2.4.4 Fill factor and efficiency

A measure of the squareness (quality of the shape) of the I-V curve is called the fill factor,  $FF$ . It is the ratio of the areas of the rectangles defined by  $V_{mp}$ ,  $I_{mp}$  and  $V_{oc}$ ,  $I_{sc}$  and is always less than one. The  $FF$  is given by Equation 2.28

$$FF = \frac{P_{max}}{V_{oc}I_{sc}} = \frac{V_{mp}I_{mp}}{V_{oc}I_{sc}} \quad (2.28)$$

Empirically, the ideal fill factor is given by Equation 2.29 [26]

$$FF = \frac{v_{oc} - \ln(v_{oc} + 0.72)}{v_{oc} + 1} \quad (2.29)$$

where  $v_{oc} = \frac{q}{nkT}V_{oc}$  is the normalised value of the open circuit voltage. The higher the  $FF$ , the more the I-V curve resembles a constant current source with maximum voltage and the higher the electric power that can be extracted.

Probably, the most important performance indicator of a solar cell is the efficiency,  $\eta$ , defined as the ratio of the power output to the power input or in other words, the ratio of the electrical energy generated by the device to the light energy incident on the device. Solar cell efficiency is reported at maximum power condition and calculated as given by Equation 2.30

$$\eta = \frac{P_{max}}{P_{inc}} = \frac{V_{mp}I_{mp}}{P_{inc}} = \frac{FFV_{oc}I_{sc}}{P_{inc}} \quad (2.30)$$

where  $P_{inc}$  is the incident power.  $P_{inc}$  is an important experimental parameter to compare efficiencies of solar cell devices which therefore calls for standard test conditions to be used. For flat plate modules, the AM1.5G spectrum with an integrated irradiance of  $1000 \text{ W m}^{-2}$  at  $25^\circ \text{C}$  is used. One of the major reasons for low efficiency of solar cells is due to the fact that each photon, irrespective of its energy, generates one electron-hole pair. The electron and hole pair generated quickly relaxes back to the edges of the respective carrier bands emitting phonons, which have low energy but relatively high

momentum compared to a photon. This results in dissipation of energy as heat. In addition, recombination of carriers which takes place in the bulk of the semiconductor as well as the surfaces reduces the efficiency of solar cells.

### 2.2.4.5 Parasitic resistance

The diode equation (Equation 2.21) does not take into consideration the effect of parasitic resistances (series and shunt resistance) which are always present in real solar cells. The series resistance can be due to the movement of current through the emitter and the base of the solar cell i.e. base and emitter sheet resistances, the contact resistance between the metal contact and the semiconductor and the resistance of the top and rear metal contacts. Shunt resistances are due to current leakage across the p-n junction, non peripheral regions in the presence of crystal defects and precipitates of foreign impurities in the junction as well as leakage currents across the edge of the cell [26]. When these parasitic resistances are incorporated, the diode equation in the first quadrant is given by

$$I = I_L - I_0 \left( e^{\frac{q(V+IR_s)}{nkT}} - 1 \right) - \frac{V + IR_s}{R_{sh}} \quad (2.31)$$

where  $R_s$  and  $R_{sh}$  are the series and shunt resistances, respectively.

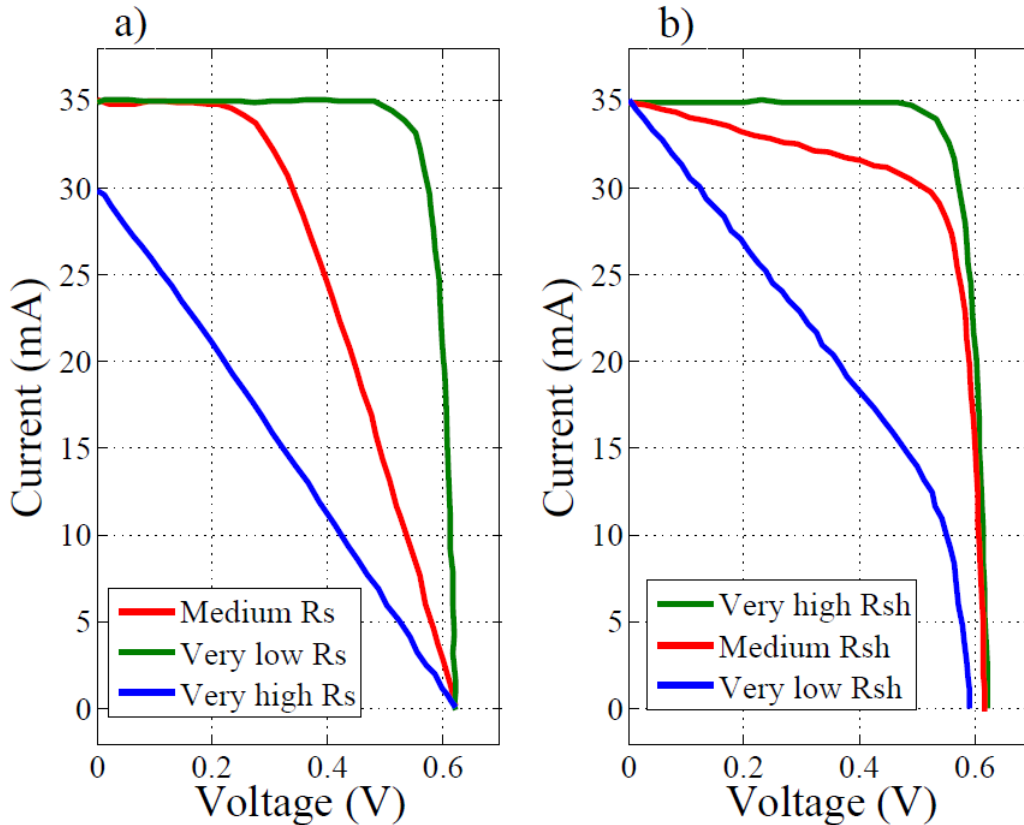


Figure 2.4: Simulated effect of: a) series resistance b) Shunt resistance, on I-V curves of solar cells.

The series resistance affects the short circuit current by biasing the dark diode, causing the current through the load (short circuit) to be less than the photo-generated current. Series resistance, however, does not affect the solar cell at open circuit voltage, as illustrated in Figure 2.4(a), since the overall current flow through the solar cell, and therefore the voltage drop across the series resistance is zero [35, 27]. The shunt resistance reduces  $V_{oc}$  but does not affect  $I_{sc}$ , as illustrated in Figure 2.4(b), since at short circuit conditions, the short circuited path provides the lowest resistance compared to the leakage path [27, 35]. The current path through the shunt resistance when the circuit is opened at the load lowers the bias across the diode, hence degrading  $V_{oc}$ . Generally, resistive effects in solar cells reduce the efficiency of the solar cell through power dissipation in the resistances. For typical values of shunt and series resistance, the major impact of parasitic resistance is to reduce the fill factor of the device. The series resistance degrades the fill factor by increasing the bias across the diode. Since the diode current varies exponentially with the diode bias, parasitic diode current increases greatly even when there are very small changes in series resistance. The effect of series resistance can be approximated by [26]

$$FF = FF_0 \left( 1 - R_s \frac{I_{sc}}{V_{oc}} \right) \quad (2.32)$$

where  $FF_0$  is the ideal fill factor as defined by Equation 2.29. Shunt resistance degrades the fill factor by diverting some of the photo-generated current that would otherwise go through the load. Its effect on fill factor can be approximated by [26]

$$FF = FF_0 \left\{ 1 - \left( \frac{v_{oc} + 0.7}{v_{oc}} \right) \frac{FF_0 V_{oc}}{R_{sh} I_{sc}} \right\} \quad (2.33)$$

At low light levels, the photo-generated current is low and any current loss to the shunt will have a significant impact. In high quality solar cells,  $R_s$  is very low while  $R_{sh}$  is as high as possible.

### 2.2.5 Temperature effect

Increasing the temperature of a solar cell reduces the bandgap according to Equation 2.25. The decreased badgap results in more absorption of light of longer wavelength, leading to an increase of  $I_{sc}$ . However, the parameter most affected by an increase in temperature is the  $V_{oc}$  due to the temperature dependence of  $I_o$ . The temperature dependence of  $I_o$  can be expressed as [26]

$$I_o = BT^\gamma e^{-\left(\frac{E_{GO}}{kT}\right)} \quad (2.34)$$



where  $E_{GO}$  is the band gap linearly extrapolated to absolute zero,  $B$  is a temperature independent constant while  $\gamma$  incorporates all possible temperature dependencies of the other material parameters. An increase in temperature thus increases the saturation (recombination) current and results in a decrease in  $V_{oc}$  as seen from Equation 2.23. Although  $I_{sc}$  increases with increasing temperature, the decrease of  $V_{oc}$  plays a more dominant role, which results in the decrease of  $\eta$  as temperature increases. Figure 2.5 demonstrates the effects of temperature on the I-V characteristic of a solar cell.

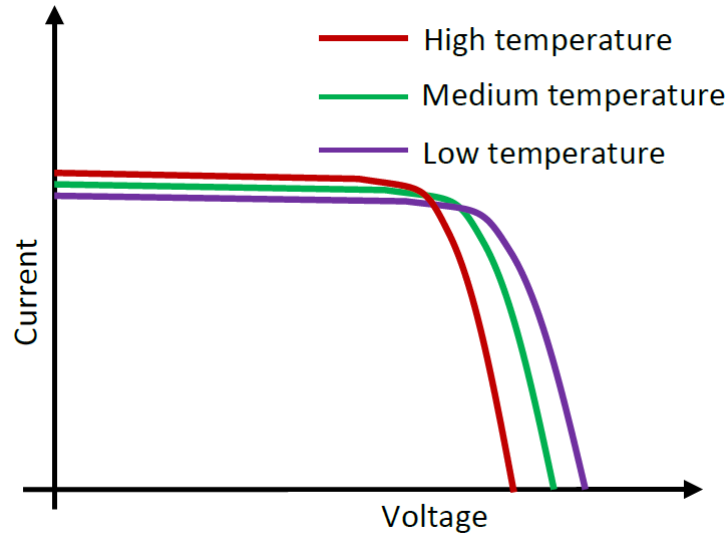


Figure 2.5: Effect of temperature on I-V characteristics of a solar cell.

## 2.3 Solar cells under concentration

### 2.3.1 Effect of illumination intensity

Operating solar cells under concentration can result in higher conversion efficiencies since both current and voltage increase with light intensity. If a solar cell is well optimised and in low injection conditions so that minority carrier recombination rates are linear, the short circuit current ( $I_{sc}$ ) increases linearly with the level of concentration (concentration ratio)  $X$ , as long as  $X$  is not very large (typically  $X < 100$ ). The level of concentration refers to the ratio of the solar radiation incident on a solar cell at a given concentration to the solar radiation at one sun irradiance. This ratio is normally expressed in terms of number of 'suns'. The one sun ( $1X$ ) irradiance is normally taken to be equal to  $1000 \text{ Wm}^{-2}$  [35]. Thus,

$$I_{sc}^X = XI_{sc} \quad (2.35)$$

where  $I_{sc}^X$  is the short circuit at a concentration level of  $X$  suns while  $I_{sc}$  is the short circuit current at 1-sun condition. Since  $V_{oc}$  varies logarithmically with short circuit current (Equation 2.23), then  $V_{oc}$  varies logarithmically with  $X$  according to Equation 2.36

$$V_{oc}(X) = \frac{nkT}{q} \ln \left( \frac{XI_{sc}}{I_o} + 1 \right) \approx V_{oc}(1) + \frac{nkT}{q} \ln X \quad (2.36)$$

where  $V_{oc}(1)$  is the one sun  $V_{oc}$ . At low concentration levels and for a solar cell with minimal series resistance, higher  $V_{oc}$  results in higher  $FF$ . However, as the concentration level increases, the resulting high current density leads to an increase in resistive losses that result in a decrease in  $FF$  and efficiency. Thus for a given series resistance of the solar cell, efficiency increases initially with concentration due to increase in  $V_{oc}$  with concentration until the effect of series resistance losses dominates after which the efficiency decreases with increase in concentration [35]. Since concentrator photovoltaic (CPV) solar cells typically operate at high current densities, series resistance plays a very significant role in their performance and therefore the metal grid configuration of CPVs must be carefully designed to minimise the series resistance losses. Thus one of the main differences between the fabrication technology of CPVs and standard solar cells is the requirement for CPVs producing higher current densities to have very low series resistance.

### 2.3.2 Effect of concentration on recombination

Under concentrated light conditions, the photo-generated minority charge carrier density may exceed the doping density, which leads to high injection conditions. Under high injection conditions, the excess minority charge carrier concentration is much higher than the thermal equilibrium majority charge carrier concentration but the excess hole density must be equal to the excess electron density, for charge neutrality to exist i.e.  $\Delta n = \Delta p \gg n_0, p_0$  [36, 37]. In the limit where concentration of free electrons is equal to the concentration of free holes i.e.  $n = p$ , and assuming  $n \gg n_1$  and  $p \gg p_1$ , Equation 2.8 reduces to [30]

$$U_{SRH} \approx \frac{n}{\tau_{po} + \tau_{no}} \quad (2.37)$$

The SRH recombination rate is still proportional to the carrier concentration but the carrier lifetime is higher since the local carrier lifetimes generally increase with increase in carrier concentration. This is because carrier generation rate dominates carrier recombination rate, which improves charge carrier lifetime [35]. If the SRH recombination is the dominant recombination mechanism at high injection levels, superposition should still hold but the short circuit current may increase even faster than the concentration level due to the longer carrier lifetime at high injection. For radiative and Auger recom-

bination mechanisms, Equations 2.4 and 2.6 also reduce to [30]

$$U_{rad} = Bn^2 \quad (2.38)$$

$$U_{aug} = An^3 \quad (2.39)$$

in the limit  $n = p$ . Radiative and Auger recombination mechanisms therefore become non-linear under high injection conditions and if they are the dominant recombination mechanisms at such injections levels, the superposition principle will no longer hold [30]. In this case, the dark current term will increase with generation rate but  $V_{oc}$  will increase more slowly than is predicted by Equation 2.36. Thus a change in the intensity dependence of  $V_{oc}$  can be used to differentiate between the dominating recombination mechanisms at different injection levels. For  $n = p$  and if  $E_{Fn} - E_{Fp} \approx qV$ , where  $V$  is the voltage across the p-n junction, while  $E_{Fn}$  and  $E_{Fp}$  are the quasi Fermi levels for the electrons and holes respectively, then [38]

$$np = n^2 = n_i^2 e^{\frac{qV}{kT}} \quad (2.40)$$

or

$$n = n_i e^{\frac{qV}{2kT}} \quad (2.41)$$

Consequently, recombination will vary as  $\sim e^{\frac{qV}{2kT}}$  for SRH,  $\sim e^{\frac{qV}{kT}}$  for radiative and  $\sim e^{\frac{3qV}{2kT}}$  for Auger recombination process. This corresponds to ideality factors of 2, 1 and  $\frac{2}{3}$  for SRH, radiative and Auger recombination mechanisms at high injection levels. The ideality factors for different recombination mechanisms in a solar cell at different injection levels are summarised in Table 2.1.

Table 2.1: Ideality factors for different recombination mechanisms at different injection levels.

Recombination mechanism	Injection level	Ideality factor
SRH	Low	1
SRH	High	2
Radiative	Low	1
Radiative	High	1
Auger	Low	1
Auger	High	$\frac{2}{3}$
Surface	Low	1
Surface	High	2

## 2.4 Quantum efficiency and spectral response

The quantum efficiency,  $QE$ , of a solar cell is the ratio of the number of electron-hole pairs produced by an incident photon of a given wavelength. We distinguish between internal and external quantum efficiencies, which differ in terms of consideration of reflection from the cell surface. The internal quantum efficiency ( $IQE$ ) only considers photons that are not reflected from the cell surface and refers to the fraction of photons transmitted into the material that result into electron-hole pairs while External Quantum efficiency ( $EQE$ ) refers to the ratio of the electron-hole pairs produced to the number of incident photons.  $EQE$  considers all photons that are incident on the solar cell surface. The expressions for  $EQE$  and  $IQE$  are given in Equations 2.42 and 2.43, respectively [39].

$$EQE(\lambda) = \frac{I_{sc}}{q} \frac{hc}{P_{in}(\lambda)} \quad (2.42)$$

where  $P_{in}(\lambda)$  is the incident photon energy and  $\lambda$  is the wavelength.

$$IQE(\lambda) = \frac{1}{1 - R(\lambda)} EQE(\lambda) \quad (2.43)$$

where  $R(\lambda)$  is the reflection coefficient at  $\lambda$ .  $IQE$  is higher than  $EQE$ , low  $IQE$  values indicate high recombination in the semiconductor material. A typical quantum efficiency characteristic is shown in Figure 2.6 where lower  $QE$  for both short and long wavelength radiations is observed.

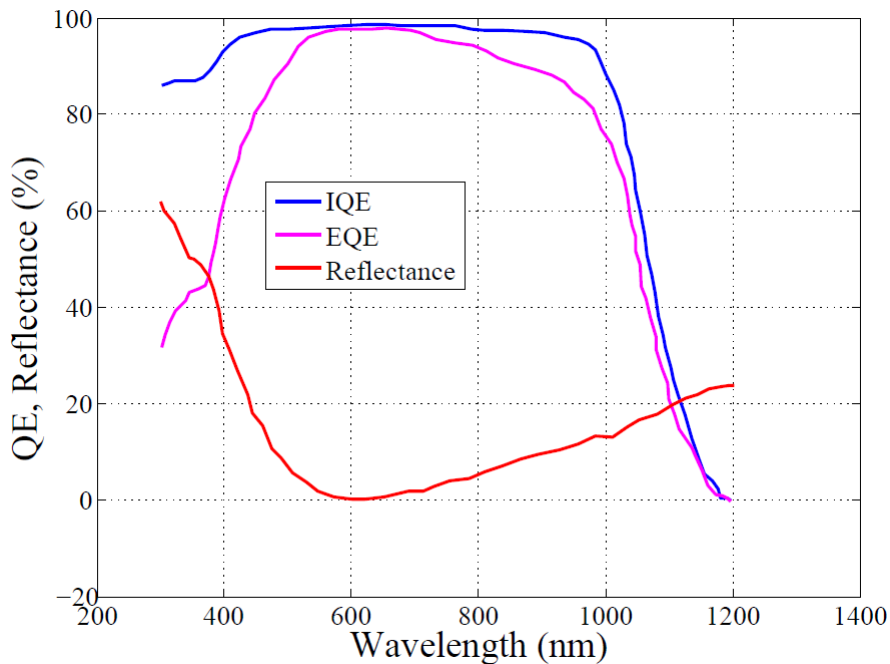


Figure 2.6: Typical quantum efficiency and reflectance curves of a semiconductor material.

The low  $QE$  at shorter wavelengths is due to strong recombination at the front surface while at longer wavelengths, it results from rear surface recombination and low absorption of the long wavelength radiations. Related to the quantum efficiency is the spectral response,  $SR(\lambda)$  of the solar cell. The spectral response can be used to analyse how photons of different wavelengths contribute to the short circuit current. It is the ratio of the photocurrent generated by a solar cell to the power incident on the solar cell at a given wavelength and can be expressed as [40].

$$SR(\lambda) = \frac{q\lambda}{hc} QE(\lambda) \quad (2.44)$$

where  $c$  is the speed of light in a vacuum. The spectral response can thus be internal or external. The short circuit current can be determined from the spectral response of the cell and the incident spectrum through the relation [27]

$$I_{sc} = \int SR(\lambda) f(\lambda) d\lambda \quad (2.45)$$

where  $f(\lambda)$  is the incident spectrum. The spectral response of a solar cell gives an indication of the extent to which a solar cell is able to convert the absorbed solar radiation into photo-generated current at different radiation wavelengths.

## 2.5 Solar cell equivalent circuit models

As already mentioned, a solar cell is a p-n junction. When exposed to light whose photo-energy is greater than the band gap of the semiconductor material, a photo-current proportional to the incident radiation is generated. The current generated by the solar cell is given by Equation 2.31. In order to understand the performance and operation of a solar cell, the solar cell equation (Equation 2.31) can be modelled as a current generator in parallel with a diode representing the light generated current and the dark recombination current mechanisms respectively. This model is commonly referred to as the single diode model, which is a modified Shockley diode equation incorporating a diode quality factor to take into account the quality of the junction and the effect of the different recombination mechanisms. The equivalent circuit diagram of the single diode model is shown in Figure 2.7.

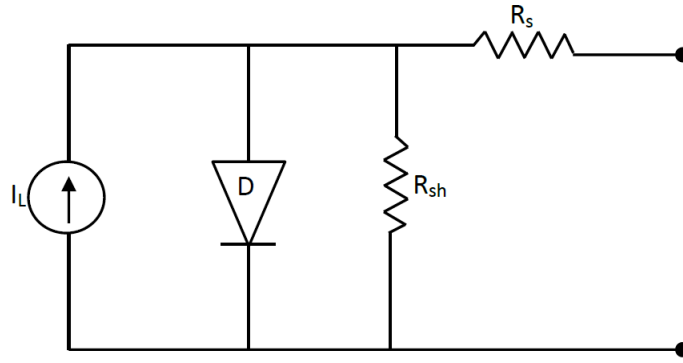


Figure 2.7: Single diode equivalent circuit model.

In order to account for radiative recombination in the quasi-neutral region and the SRH recombination in the space charge region, the double diode model, which simulates the space-charge recombination effect by incorporating a separate current component with its own exponential voltage dependence is used. This model shown in Figure 2.8 consists of two parallel connected diodes,  $D_1$  in which only band to band recombination takes place, and  $D_2$  in which only recombination through defects occurs in the space charge region [41]. Under illumination, the double diode equation is given by

$$I = I_L - I_{01} \left( e^{\frac{q(V+IR_s)}{n_1 kT}} - 1 \right) - I_{02} \left( e^{\frac{q(V+IR_s)}{n_2 kT}} - 1 \right) - \frac{V + IR_s}{R_{sh}} \quad (2.46)$$

where  $I_{01}$  is the dark saturation current due to recombination in the quasi neutral region,  $n_1$  is the ideality factor for  $D_1$  while  $I_{02}$  is the dark saturation current in the space charge region and  $n_2$  is the ideality factor for  $D_2$ .

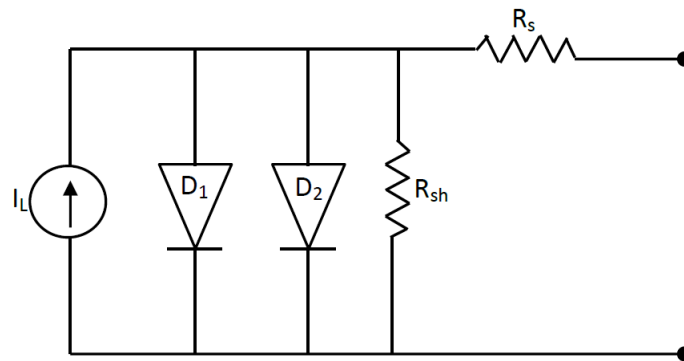


Figure 2.8: Double diode equivalent circuit diagram.

If recombination through defects is not neglected, one must then consider that at small voltages, recombination through defects dominates while at large voltages, band to band recombination dominates [41].

## 2.6 Concentrator photovoltaic systems

Generation of electrical energy using solar cells is desirable but the cost of solar energy conversion into electrical energy using current photovoltaic technologies is still expensive and therefore prohibitive. Alternative technologies to bring the cost down are therefore being sought in order to make solar energy as competitive as the conventional energy sources. The use of concentrating systems to concentrate the solar light onto a small area of the solar cell is therefore considered. In CPV systems, optical devices are used to concentrate the light onto small and high efficient photovoltaic solar cells thus reducing the area of the active material required to generate a given amount of energy [42, 43]. In this way, expensive solar cell material is replaced by low cost optical devices while at the same time increasing the intensity of light reaching the solar cell. CPV systems can be classified according to the level of concentration of the solar radiation incident on the solar cell. According to this classification, CPV systems fall into three groups i.e. Low concentration (LCPV) that have a concentration level between 1 and 40 suns ( $1 - 40X$ ), medium concentration (MCPV) that have a concentration level between 40 and 300 suns ( $40 - 300X$ ) and high concentration (HCPV) that have a concentration level between 300 and 2000 suns ( $300 - 2000X$ ) [43]. Generally, LCPV and MCPV use high efficiency silicon solar cells while HCPVs use solar cells based on III-V semiconductor materials [44]. In addition to reducing the solar cell active material, CPV systems also offer a possibility of increasing the solar cell efficiency.

### 2.6.1 Silicon concentrator solar cells

Silicon concentrator solar cells are a promising alternative to the conventional PV technology as the solar cells can be made smaller according to the concentration ratio, which results in the use of less photo-active material. The use of conventional silicon solar cells in concentrator solar systems is limited by the increase in resistive losses that lead to a reduction in efficiency under concentration. In conventional solar cells, it is difficult to obtain very low series resistances due to the presence of sheet resistance of the front side emitter that arises from the lateral current flow in the diffused regions, which must be kept low for good quantum efficiency [45]. For use in concentrator systems, silicon solar cells specially designed are fabricated using technologies that produce high efficiency solar cells. The technologies used should produce solar cells that maintain high bulk minority carrier lifetime, low surface recombination velocity, excellent reflection control and light trapping and good design of metallisation to minimise optical and resistance losses [45, 46]. High efficiency silicon solar cells with efficiencies  $\sim 27\%$  have been achieved under concentration using the back contact solar cell technology [47]. However, the initial designs were too complex for low concentration applications and

the fabrication costs for this technology were quite high, making the final solar cell device quite expensive and therefore unlikely to be economically competitive [48, 49]. Back contact solar cells have both positive and negative electrical contacts at the rear of the cell. This helps to reduce the shading and resistive losses from the gridlines and allows easy interconnection since the front surface need not to be accessed with interconnects [50, 46]. In addition, it allows for an optimised solar cell packing density that increases the total active area efficiency of the module and also gives an attractive visual appearance of the modules, an aspect that is much appreciated by designers and architects for building integration photovoltaics [51, 50, 52]. Back contact solar cells can be grouped into three categories i.e back contact back junction solar cells (BC-BJ), the emitter wrap through (EWT) and metallisation wrap through (MWT).

### 2.6.1.1 Back contact-Back junction silicon solar cells

The back contact-back junction (BC-BJ) solar cells, also known as the interdigitated back-contact (IBC) solar cells have both positive and negative electrical contacts and the collecting junction at the rear of the cell. Because the collecting junction is situated at the rear of the solar cell, charge carriers generated at the front surface have to traverse the entire wafer thickness to the rear side, which therefore requires such a solar cell to have high carrier diffusion lengths [53]. The basic structure of an IBC solar cell is shown in Figure 2.9 [54].

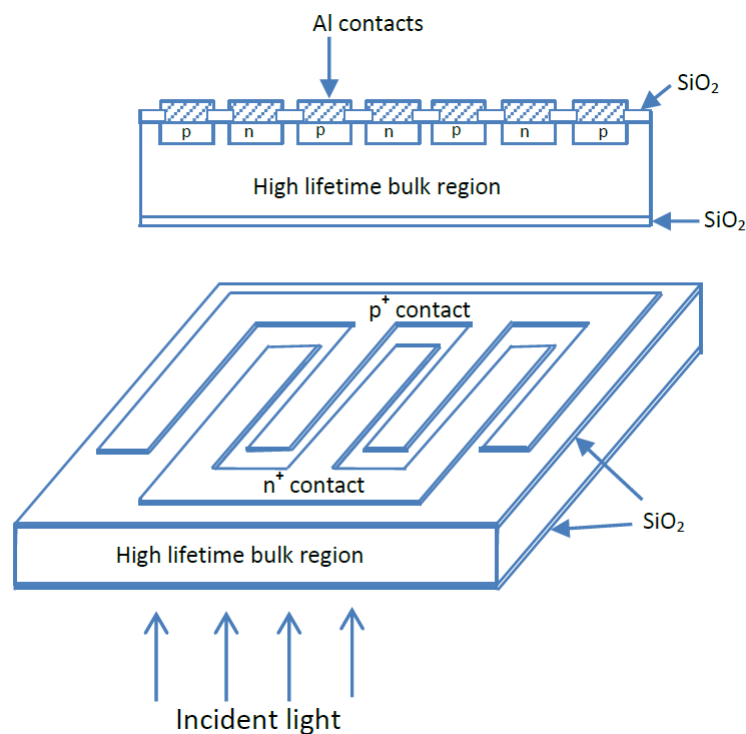


Figure 2.9: Cross-section and structure of an IBC solar cell.



They are usually fabricated on n-type Czochralski grown silicon (Cz-Si) due to the higher minority carrier lifetimes of n-type as compared to the p-type Cz-Si with similar impurity concentrations [55]. This therefore means that a  $p^+$  emitter is required to form a p-n junction. Since electrical contacting and hence extraction of charge carriers occurs on the rear side of the solar cell device, shadowing losses due to the metal grid on the front surface are completely eliminated, resulting into an increased photo-current and efficiency of the device [56]. Thus for high current collection efficiency, the minority carrier diffusion length should be much bigger compared to the thickness of the cell and the front surface should be well passivated to minimise surface recombination due to the high minority charge carrier concentration levels especially under concentrated light [56, 57]. However, because the rear surface is not completely covered by a collecting emitter, recombination in regions without the emitter occurs, reducing the short circuit current of the device, an effect referred to as electrical shading. It is a result of a reduced minority charge carrier collection probability due to an increased recombination in the non-collecting base region that consists of the back surface field (BSF) and generally an undiffused gap region. Electrical shading losses depend on the geometry of the metallisation fingers, base doping concentration and the passivation quality of the rear surface [58, 59]. The rear surface of IBC solar cells can be independently optimised for low series resistance and high fill factors, while the front surface is optimised for anti-reflection and passivation properties to achieve maximum optical coupling and high short circuit currents. Conversion efficiencies of up to 24.2% have been achieved using an n-type CZ-Si wafer [60].

### 2.6.1.2 Emitter wrap through silicon solar cells

In the emitter wrap through (EWT) solar cells, the front surface collecting junction (emitter) is connected to the interdigitated contacts at the back of the solar cell using laser drilled and emitter diffused holes (vias) through the substrate [61] as shown in Figure 2.10 [62]. Due to the presence of collecting junctions on both sides of the cell, the EWT concept is considered particularly suited for materials with low bulk diffusion lengths, since the average minority carrier distance to the emitter is significantly reduced. In addition, since carrier collection in an EWT cell can occur at both the front and back junctions, high current densities can be collected resulting in higher collection efficiency with medium quality base silicon compared to the IBC solar cell [63, 12]. However, large area EWT cells with screen printed metallisation have high series resistance that limits the fill factor, though efficiencies up to 21.4% have been reported on FZ Si [48]. If EWT solar cells are properly designed, very low series resistance can be achieved without the need for high vias density.

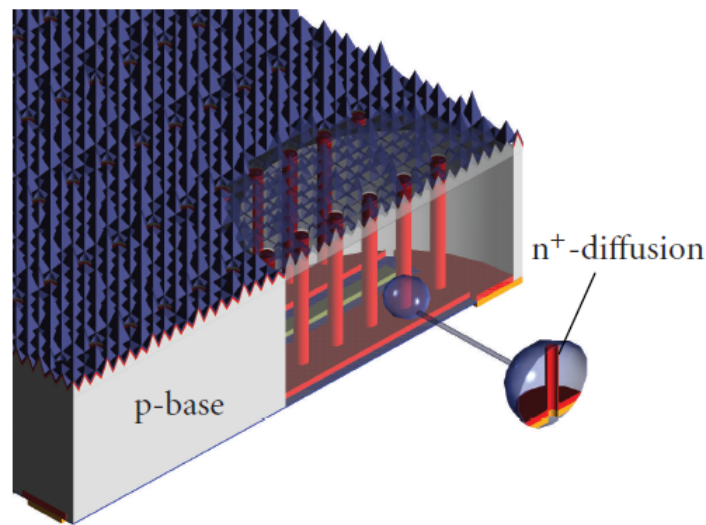


Figure 2.10: Schematic illustration of an emitter wrap through (EWT) Silicon solar cell.

### 2.6.1.3 Metal wrap through.

These cells are characterised by the presence of a metal grid and the emitter on the front surface in combination with the presence of interconnection pads for both polarities on the rear surface [50, 51]. The front side metal fingers are connected to the busbar on the rear side through the laser drilled holes, which are filled with metal as shown in Figure 2.11 [62].

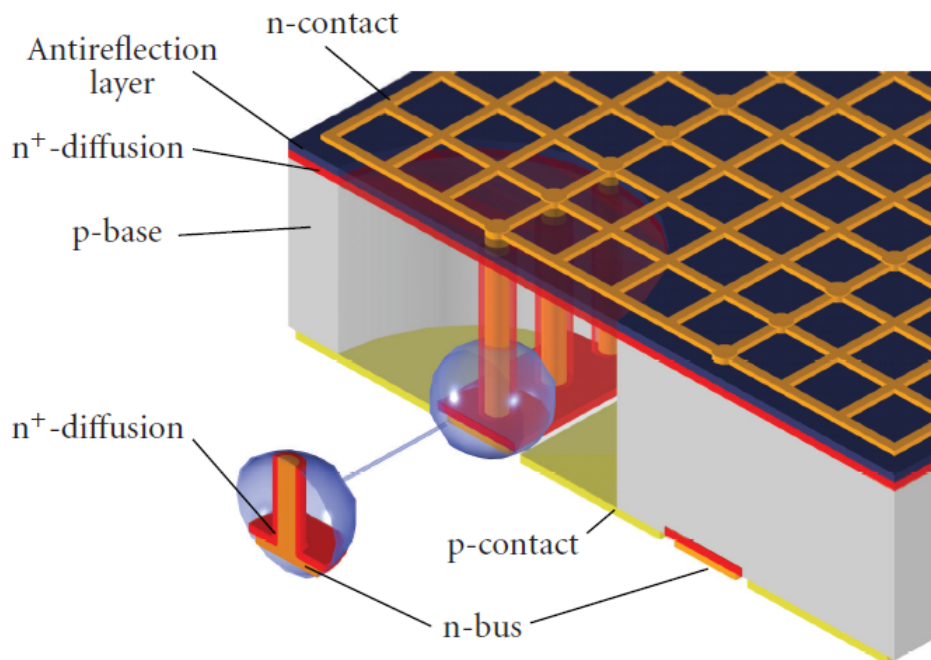


Figure 2.11: Structure of a Metal Wrap through (MWT) solar cell.

Compared to EWT, the conduction in the holes of metal wrap through (MWT) cells is

high because of the application of metal inside the holes [64]. As a result, a limited number of holes will be sufficient to enable a good fill factor for MWT cells, making the processing easier than for EWT. Just like EWT cells, the MWT solar cell design does not require long carrier lifetimes material like the BC-BJ cells, and can therefore be produced on conventional multi-crystalline silicon wafers. Compared to the conventional solar cell production technology, only two additional steps are required i.e. laser via drilling and rear contact isolation, which is an advantage, compared to other rear contact cell technologies. MWT solar cell efficiencies of up to 19% for Cz-Si and up to 17.5% for mc-Si have been reported [65, 66].

### **2.6.2 Multijunction concentrator solar cells**

The highest conversion efficiencies attained for solar cells so far have been achieved with the multijunction approach using solar cells made of III-V semiconductor materials. Multijunction solar cells consist of multiple semiconductor layers (subcells or junctions) of different band gaps stacked in such a way that the front surface is transparent to radiations absorbed by the subsequent layers. This is attained by stacking the different semiconductor layers in such a way that the top (front) subcell has the highest band gap while the subsequent subcells have decreasing band gaps, with the bottom (rear) subcell having the lowest band gap. This ensures that high energy photons are absorbed in the top subcell and generate electron-hole pairs while the less energetic photons pass through to the lower subcells where they are absorbed resulting into generation of more electron hole pairs. Due to the longer minority carrier lifetime of electrons than holes in most III-V materials, each subcell in the multijunction is doped as a thin n-type emitter on a thick p-type base [67, 68]. Each subcell is efficiently tuned to absorb a given range of wavelengths of the solar spectrum with the subcells having overlapping quantum efficiencies that collectively absorb a wider range of wavelengths from the solar spectrum. This helps to reduce transmission and thermal losses commonly present in conventional single junction solar cells and therefore increase the conversion efficiency [69]. Figure 2.12 [70] shows the AM1.5 spectrum highlighting the parts of the spectrum that can be theoretically absorbed by a silicon solar cell (Figure 2.12(a)) and a triple junction solar cell (Figure 2.12(b)).

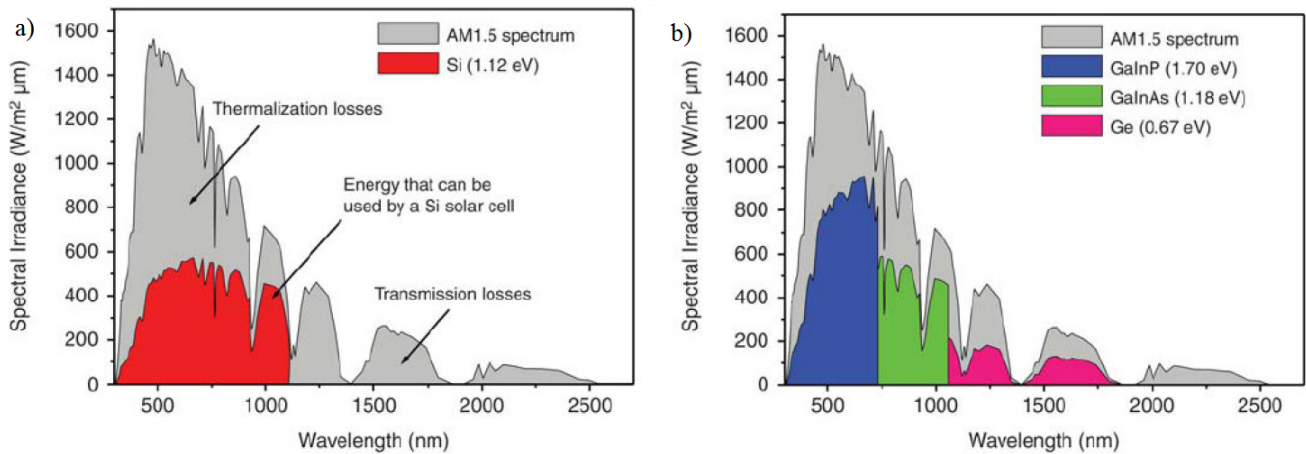


Figure 2.12: Spectral losses in: a) Silicon solar cell, b) InGaP/InGaAs/Ge triple junction solar cell.

The maximum solar irradiance that can be absorbed by the silicon solar cell and the InGaP/InGaAs/Ge triple junction solar cell is shown in the figure where a reduction in thermalisation and transmission losses is realised by using a triple junction solar cell.

The subcells in multijunction solar cells can be mechanically stacked or monolithically grown to form a two terminal device in which each junction in the stack must be transparent to radiations with energy below their band gaps. This sets constraints, especially on the subcell substrates and back contact metallisations to be used through which the radiations must pass [71]. These constraints, are, however, not insurmountable and different approaches have been used to overcome them.

### 2.6.2.1 Mechanically stacked multijunction solar cells

Mechanically stacked multijunction solar cells consist of multiple subcells with different band gaps, each fabricated on its own substrate and then stacked using adhesives on top of each other as shown in Figure 2.13 [72]. Each subcell has its own contacts and can be connected separately. This makes these devices more flexible as subcells with different band gaps can be connected together without the need to worry about lattice mismatch issues and also have low spectral sensitivity compared to monolithically grown multijunction devices [73]. In addition, the subcells do not necessarily have to be connected in series which eliminates the need for current matching, thus allowing full exploitation of the current generated by each subcell in the solar cell device.

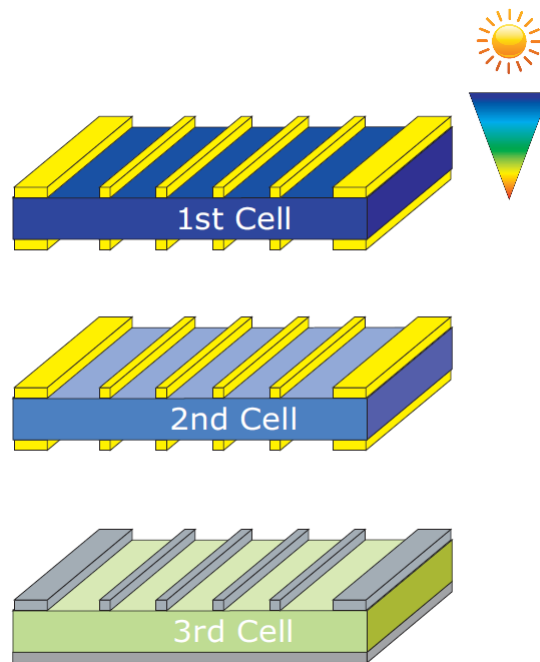


Figure 2.13: Mechanically stacked multijunction solar cell.

However, technological difficulties in maintaining the optimum optical coupling between the subcells, the complex electrical architecture required due to individual subcell connection and a higher series resistance due to multiple lateral current flows have made the devices more complex to manufacture [73]. In addition, since the subcells are manufactured separately with each subcell having its own substrate, it makes these devices more bulky and expensive to make. Efficiencies of more than 38% have been attained with mechanically stacked multijunction solar cells using the spectrum splitting technique [74].

### 2.6.2.2 Monolithic multijunction solar cells

In monolithic multijunction solar cells, the subcells are epitaxially grown one upon another on a single substrate to form a two terminal device in which the subcells are connected in series. Since most multijunction solar cells made of thin n-doped emitter on a thick p-doped base, connecting such n-on-p subcells in series would result to p-on-n diodes between the subcells, which would then block current flow between the subcells. Series connection of the subcells is thus realised using interband tunnel diodes as shown in the schematic diagram in Figure 2.14 [75].

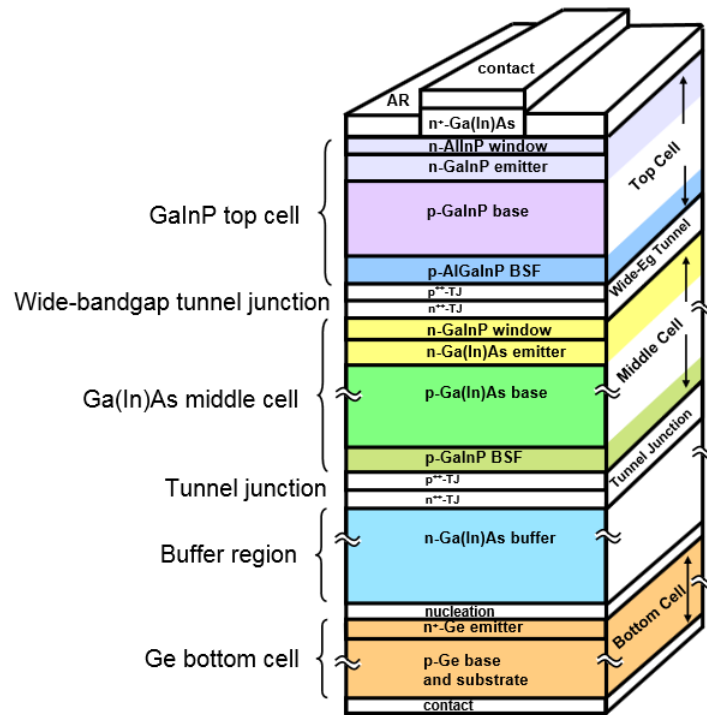


Figure 2.14: Schematic diagram of a monolithic concentrating triple junction (CTJ) solar cell.

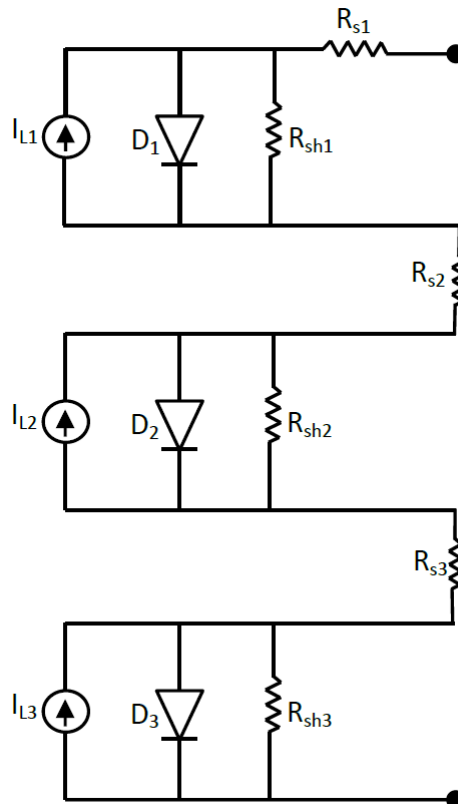


Figure 2.15: Equivalent circuit model of a CTJ solar cell.

The two terminal equivalent circuit model for the CTJ, with each junction modelled with

a single diode, is shown in Figure 2.15. The interband tunnel diodes joining the subcells are modelled as resistors and incorporated into the series resistances of the subcells [76]. Tunnel diodes generally consist of thin degenerately doped p-on-n layers connected in reverse polarity between the subcells. They provide low electric resistance to current flow and have high optical transmissivity. The I-V characteristic of a tunnel junction diode is shown in Figure 2.16 [68].

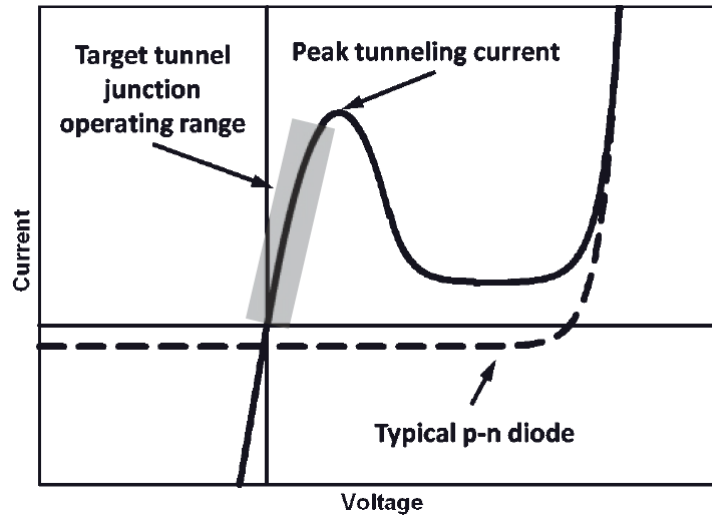


Figure 2.16: I-V characteristic of a tunnel diode as compared to a typical p-n junction diode

At low voltages, high current densities flow and the I-V characteristic is essentially ohmic. However, current flow decreases after the characteristic peak tunneling current density. At significantly higher voltages, the current density increases again and the tunnel diode behaves like a normal p-n junction diode as shown in Figure 2.16. The operating range of a tunnel diode is therefore between 0 V and the voltage at the peak tunnelling current density. Tunnel diodes for multijunction solar cells should have high peak current densities. These are achieved by using thin, heavily doped layers of relatively low band gap semiconductors.

Because the subcells are connected in series, the current between the subcells must be matched since the current generated by the device is limited by the subcell producing the lowest current i.e. the output current  $I$  from the device is given by

$$I = \min \{I_i\} \quad (2.47)$$

where  $I_i$  is the current generated by subcell  $i$ . The current generated by each subcell is in turn determined by its spectral response and the spectral content of the beam incident on it i.e.

$$I_i = \int SR_i E_i(\lambda) \quad (2.48)$$

where  $SR_i$  is the spectral response of subcell  $i$  and  $E_i$  is the spectrum incident on it. The device voltage  $V$  is given by [72]

$$V = \sum_i V_i \quad (2.49)$$

where  $V_i$  is the subcell voltage. Current matching for a given spectrum is attained through selection of appropriate band gaps for the subcells as well as through subcell thinning. However, any changes in the spectral content of the incident beam may lead to current mismatch between the subcells thus affecting the current output of the device. The monolithic multijunction solar cell is therefore very sensitive to fluctuations in the spectrum with time due to changing atmospheric conditions and the position of the sun [75]. In addition to current matching, the subcells and the substrate should be lattice matched to minimise defects or dislocations that may act as recombination centres. This creates another constraint as some semiconductor materials with suitable band gaps that can be optimally current matched are not lattice matched thus limiting the potential efficiency of the device. One way to mitigate the current mismatch constraint has been through the growth of lattice mismatched (metamorphic) devices using graded buffer layers between the subcells [77]. The graded buffer layer gradually alters the lattice constant from the substrate to that of the subsequent subcell. However, highly metamorphic materials have a large lattice mismatch ( $\sim 1.7 - 2.4\%$ ) which makes it difficult to grow the subsequent subcells [78]. In addition, during the growth, the buffer layer relaxes. This relaxation introduces defects and dislocations that propagate along the growth direction thus negatively affecting the performance of the subsequent subcells and hence the overall performance of the device [77]. This is, however, being addressed through inverted metamorphic growth, in which the solar cell device is grown upside down, with the top subcell grown lattice matched to the substrate, followed by the graded buffer layer and then the metamorphic subcell as illustrated in Figure 2.17 [78]. This preserves the material and device quality of the lattice matched, high band gap subcells and shields them from the dislocation defects from the metamorphic layers. In addition, the substrate is removed thus lowering the total weight of inverted metamorphic solar cell device. However, the removal of the substrate increases the complexity of the processing and fabrication of the cell which ultimately results in yield losses and increases the cost of the final product [77]. Currently, the state of the art multijunction solar cell is the monolithic lattice matched InGaP/InGaAs/Ge triple junction solar cell. The structure, however, does not have the optimum band gap configuration and is highly current mismatched [79]. Efficiencies of more than 40% under concentration have been attained for monolithic multijunction solar cells based on lattice matched and metamorphic solar cell technologies [79, 80, 81].



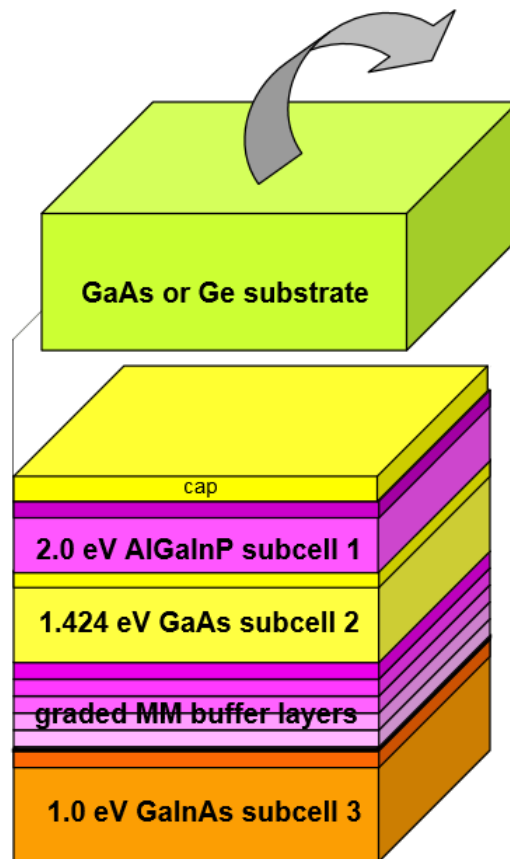


Figure 2.17: Schematic diagram of a 3-junction inverted metamorphic solar cell.

### 2.6.2.3 Effect of current mismatch on I-V characteristics

For a series connection of subcells whose individual I-V characteristics are described by  $V(I)$ , the operating voltage is the sum of the subcell voltages as given in Equation 2.49 while the short circuit current,  $I_{sc}$ , is taken to be that of the current limiting subcell for subcells without significant current leakage or reverse bias breakdown. Figure 2.18 (a) shows the individual I-V curves for the three subcells as well as the resulting I-V curve for the triple junction illustrating how the voltages of series-connected subcells add up at a given current. In the Figure, the bottom subcell has the highest current while the middle subcell has the lowest current and is therefore the current limiting subcell. A mismatch step is observed in the reverse bias region and its position depends on the reverse bias I-V characteristic of the limiting subcell. If the current limiting subcell has a low reverse breakdown voltage, the mismatch step occurs in the power quadrant of the I-V curve as shown in Figure 2.18 (b). The effect of current mismatch in monolithically grown multijunction solar cells is a big a challenge especially under outdoor conditions due to the continuously changing solar spectrum and can result in drastic performance losses.

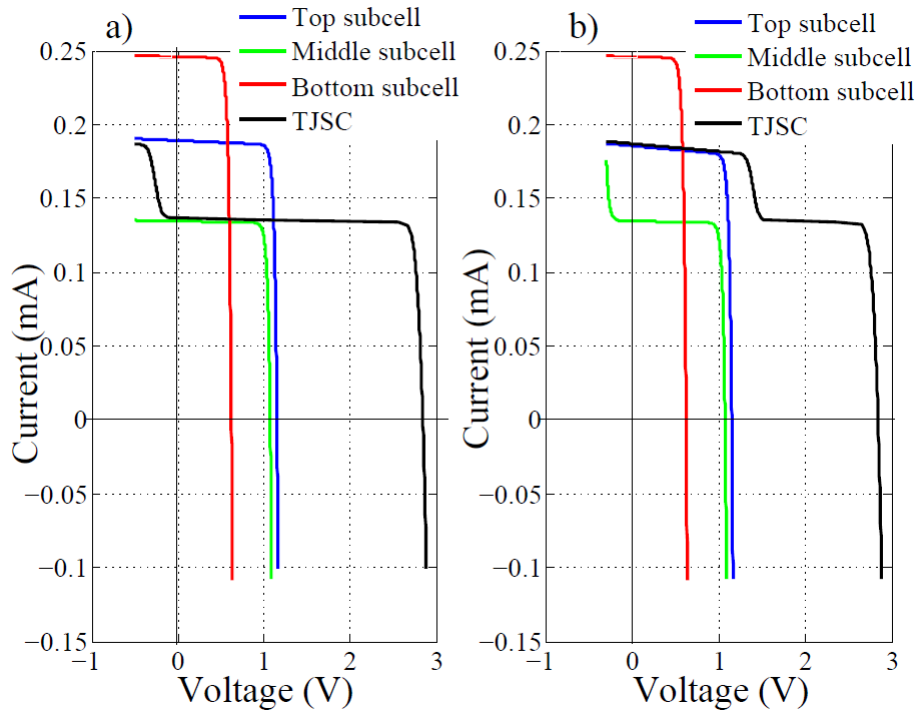


Figure 2.18: Simulated subcell I-V characteristics and the combined.

## 2.7 Conclusion

The basic theory and operating principles of solar cells have been presented in this chapter. Principal recombination mechanisms such as bulk and surface recombination processes have been discussed and expressions for their recombination rates presented. The ideal diode equation was derived and generalised for practical solar cells so as to incorporate the effect of the quality of the junction and parasitic resistances that affect the performance of solar cell devices. Solar cell equivalent circuit models based on the single and double diode models were presented. These models are used to describe the behaviour of the I-V characteristics from which device parameters  $I_o$ ,  $R_{sh}$ ,  $R_s$ ,  $n$  and performance parameters  $V_{oc}$ ,  $I_{sc}$ ,  $P_{max}$ ,  $FF$ ,  $\eta$  can be extracted. The effect of parasitic resistances as well as temperature on the I-V characteristic and hence performance of the device was demonstrated. Concentrator photovoltaic systems and their classification based on the level of concentration have been discussed. Back contact silicon concentrator cells were presented and discussed as an example of solar cells that can be used for low to medium concentration, while multijunction solar cells based on III-V semiconductors are used for high concentration PV systems. A back contact back junction silicon solar cell and an InGaP/InGaAs/Ge triple junction solar cells will be further studied and characterised in the subsequent chapters.

# Chapter 3

## LBIC mapping technique and system development

### 3.1 Introduction

The performance of opto-electronic devices is affected by spatial distribution of inhomogeneities in semiconductor materials used to fabricate them. In photovoltaic (PV) devices, these inhomogeneities may occupy very minute areas of the device but may affect current generation over a large area surrounding the affected region and hence affect the overall performance and efficiency of the device [82]. Diagnostic techniques that reveal spatially resolved material characteristics (electrical or optical) with a high spatial resolution are therefore necessary to identify the causes of these spatial variations. Such spatial variations can be examined non-destructively by focusing a laser beam onto the cell surface and measuring the photo-generated current as the beam is moved across the cell surface in a raster scan. This technique is known as the Light Beam Induced Current (LBIC) mapping technique. When solar light is used as a beam probe instead of laser light, then we have the Solar-Light Beam Induced Current (S-LBIC) mapping technique. In this case, the system has to be mounted on a two-axis sun tracker since the direct beam solar radiation is required as a beam probe. The LBIC technique generally involves shining the light beam onto the solar cell surface and measuring the photo-generated current across the terminals of the solar cell as a function of position of the light beam. The measured current across the solar cell terminals is then used to generate topographical images of the solar cell at different experimental conditions. LBIC mapping is usually carried out under short circuit current conditions and allows determination of the diffusion length of the solar cell material from local photo-generated current measurements. It should be noted that since the solar cell is spot illuminated, the current measured across the cell contacts indicates the whole solar cell material's response to point illumination [83]. For a given spectrum of light of a given

intensity incident on a solar cell, the current generated is determined by the absorption and generation properties as well as the electrical properties of the solar cell device at the point of incidence. At defect regions such as grain boundaries, the photo-generated current is reduced due to enhanced charge carrier recombination. LBIC measurements are normally performed with low intensity beams to avoid saturation of minority charge carriers which may result in changes in the local transport properties. However, some measurements have been carried out at high intensity levels with beam diameters of  $\sim 1 \mu\text{m}$  resulting into the high injection regime. In the high injection regime, the influence of the majority charge carriers on the current transport mechanism have to be considered together with the minority carrier current flow [84]. In addition, more recombination centres in the illuminated surface and in the bulk can be activated resulting in degradation of the device performance [85]. For single junction devices, it is desirable to perform LBIC measurements using monochromatic sources so as to ensure that the generation rate is the same for all the generated charge carriers [86], though white light from sources such as halogen lamps with a monochromator have been used as well as solar light as used in the S-LBIC [87]. In this Chapter, an overview of the LBIC mapping technique and systems as well as system characterisation are given. We describe the LBIC system that was designed and built to characterise different solar cell devices, including concentrator solar cells. Results of photo-response mapping of a mc-silicon solar cell device are also presented and discussed.

## 3.2 Overview of LBIC systems

Since the late 1970's, the laser scanning technique has been in use for mapping photocurrent generation uniformity in PV devices especially polycrystalline silicon solar cells [16, 88, 89]. In the 1980's, mapping of defects in PV devices was performed using a two dimensional laser scanner that used oscillating mirrors to move the incident beam in a raster pattern over the cell surface [90]. However, the two mirror laser scanner is not suitable for quantitative studies of very small areas due to difficulties in aligning and maintaining a highly focused spot over such an area [82]. In addition, for large area scans, the distance between the deflecting device and the incident point is not constant which creates problems related to maintenance of correct focusing [91]. In general, instead of moving the beam across a fixed solar cell using a set of steering mirrors or by moving the light source, the light beam probe can be fixed while the cell is moved using translation stages. Systems based on this mode of scanning tend to be slower compared to those using beam deflection since the scanning speed is determined by the speed of the translation stages. With current availability of high precision stepper motors, the translation stage approach is preferred since one can position the solar cell with a re-

peatability to the same position of less than  $1\ \mu\text{m}$ . The laser scanning technique has developed over years to a standard characterisation technique for process development of different PV devices due to advancement in technology and the growing demand for higher efficiency PV systems and has come to be known as the LBIC technique. Most of these systems are designed for small area systems at single cell level [91, 92, 87] although large area systems for full size commercial PV modules have also been developed [93]. Various research groups globally have developed LBIC systems with different capabilities. Some of the recent designs are highlighted.

Hiltner *et al.* (2000) [94] developed a high-resolution and high-sensitivity laser stepping apparatus at Colorado State University (USA) to characterise grain boundaries and local defects in thin film polycrystalline solar cells. Their system featured a diffraction limited laser spot size at different wavelengths in the red and infrared wavelength regions that could attain a spatial resolution of  $\sim 1\ \mu\text{m}$ . X-Y translation stages were used to move the solar cell sample under a fixed light beam which was sinusoidally modulated so as to allow lock in detection of the photo-current. Photodiodes were incorporated into the system to monitor the intensity of the incident beam as well as reflection from the sample. Beam steering mirrors were used to align the beam probe on to the microscope objective lens. From their system, they were able to obtain apparent quantum efficiency maps with high resolution and to probe single grains in selected devices.

Carstensen *et al.* (2003) [92] developed an advanced LBIC measurement system called CELLO that was used to determine all local parameters of a large area silicon solar cell. In their set up, halogen lamps were used to bias the solar cell device while a sinusoidally modulated infrared beam was used as a beam probe. From their results, they were able to identify material and process induced defects, obtain local series and shunt resistances maps, lateral diffusion of minority carriers as well as local I-V characteristics.

Martin *et al.* (2004) [91] designed a versatile computer controlled high resolution LBIC system capable of obtaining submicrometer resolution quantum efficiency images. Beam focusing was highly automated with focusing algorithms that enabled them to compute the optimum distance at which the focusing lens would be positioned with respect to the sample for optimum performance. The system was capable of simultaneously obtaining LBIC and specular reflection images at a resolution of  $0.5\ \mu\text{m}$ .

A large area LBIC system was developed at the Centre for Renewable Energy Systems Technology (CREST), Loughborough University, UK [95, 96] with a capability to scan solar cell modules of dimensions up to  $1.5\ \text{m} \times 1.5\ \text{m}$ . The system was able to give detailed current maps from which spatial variation of structural defects of the modules could be identified.

Vorster *et al.* (2007) [97], at Nelson Mandela Metropolitan University (NMMU), South

Africa, developed an LBIC system that uses concentrated solar spectrum as a light source (S-LBIC) by placing the measurement system on a two-axis sun tracker. The system was designed so as to be able to accommodate laser beam sources (LBIC) in place of the direct solar beam for indoor measurements and was initially developed to study concentrator photovoltaic solar cells (CPVs) but could also be used to study conventional solar cells under high saturation conditions [83]. By dynamically biasing the device under test, they were able to identify defects under different bias conditions and to obtain point-by-point I-V measurements from which device and performance parameter maps were obtained.

Though the LBIC technique is a very useful technique for mapping spatial distribution of photo-generated current on large area samples, its disadvantage is the low spatial resolution compared to other techniques such as the electron beam induced current (EBIC) [98, 99]. The minimum spot sizes that can be obtained with this technique are  $\sim 0.5 \mu\text{m}$ . This is an obstacle when one wants to probe features far below the sub-micron level.

### 3.3 LBIC system characterisation

The spatial distribution of inhomogeneities determines the overall performance of PV devices. Minute defect areas on a solar cell can considerably deteriorate the performance of the device and if connected to other well performing solar cells in a module can lead to a significant reduction in the power output of the module. The defects may be local sites of excessive recombination such as grain boundaries or dislocations, or can be shunts which are characterised by an increase of the local dark current. Improvement of PV devices performance therefore calls for characterisation of the spatial variation of the electronic properties responsible for cell performance on a point-by-point basis. The LBIC technique is used to map the spatial distribution of defects through a point-by-point illumination of the surface using a highly focused irradiation beam. The photo-generated current is plotted as a function of position to give a two-dimensional map of the current signal. Each data point on the map is generated by the current from the sample as the beam probe scans over the sample device. By dynamically biasing the device at each measurement point from reverse bias to a voltage slightly greater than its  $V_{oc}$ , point-by-point I-V characteristics are obtained to which parameter extraction algorithms are applied to extract point-by-point I-V parameters. For a given intensity and wavelength of the beam probe, the magnitude of the current generated at each point represents the material's response to the incident beam at that point. Due to the strong dependence of the LBIC signal on the laser intensity, laser stability is of utmost importance as any variation in the intensity would cause uncertainty in the measurement. In order to obtain a high resolution photo-response map, the beam probe should be op-

timally focused as this will determine the spot size of the beam probe. However, it is equally important that the system be free of mechanical and or optical fluctuations so as to ensure precise control of the illumination position and photonic stability of the beam probe [91].

### 3.3.1 Beam diameter

The beam probe diameter (spot size) partly determines the spatial resolution of the system and is related to the focal length of the lens and the size of the pre-focused beam [100]. Smaller spot diameters are obtained by optimising the focal length of the objective lens. The beam diameter is measured at the plane where the solar cell is placed by running line scans over a sharp edge or a busbar of the solar cell. The beam diameter can be obtained by measuring the distance over which the signal suddenly changes at the sharp edge or bus bar as illustrated in Figure 3.1.

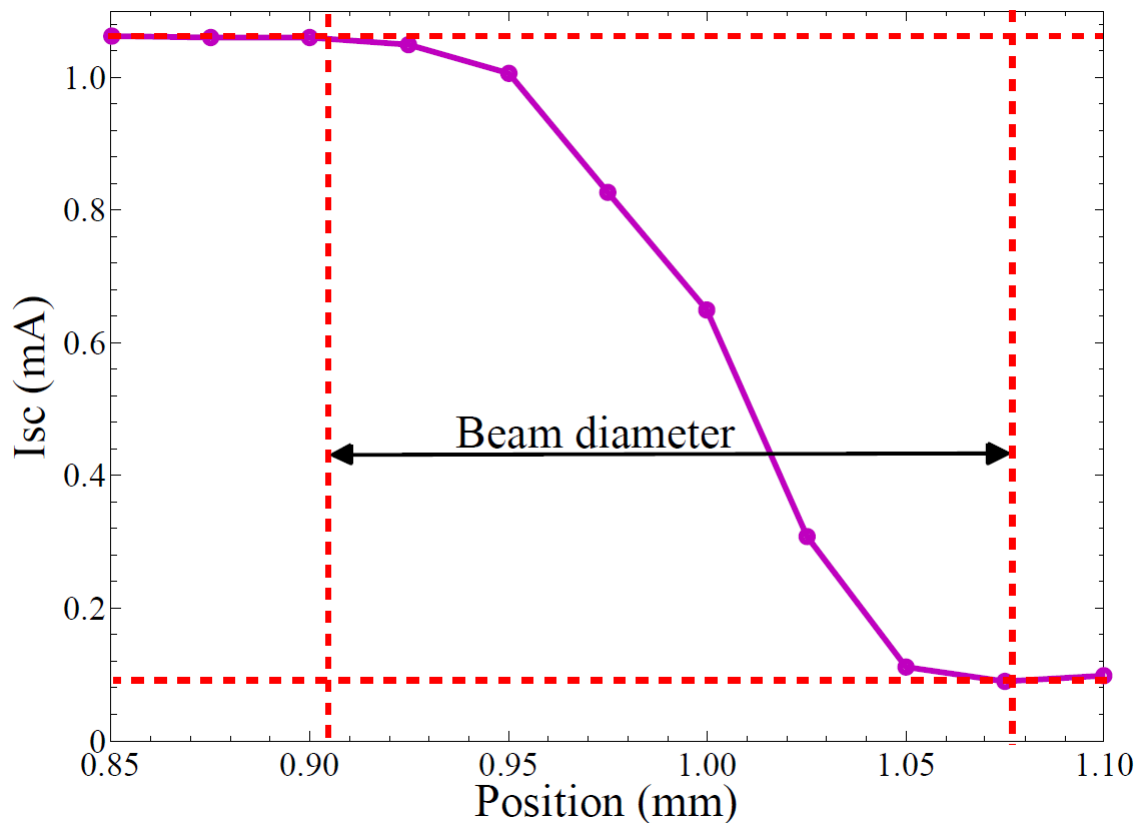


Figure 3.1: Short circuit current variation across a bus bar. The scan distance between the points when the current changes from maximum to minimum across the bus bar edge is the beam diameter.

In our set up, the spot size of a  $660\text{ nm}$  wavelength laser was obtained by determining the distance covered by the beam probe as it was scanned across the edge of a bus bar when the signal level reduced from the maximum value at the edge of the solar cell

active area to the minimum value at the bus bar, as shown in Figure 3.1. From these measurements, the average beam diameter was  $\sim 170 \mu m$ .

### 3.3.2 Generation volume

When a solar cell is spot illuminated, the distribution of the electron-hole pair generation within the sample is given by the generation volume profile. Various models have been used to describe the generation volume profile of charge carriers within a semiconductor under the influence of light or electron beam radiation [89, 101, 102, 103]. The carrier generation properties of light however, differs from carrier generation by electrons since a single photon can only generate a single electron-hole pair as opposed to many carriers generated by a single electron. The generation volume depends on wavelength and determines the density and position of the charge carriers relative to the junction. For an  $n$  doped material in low injection conditions, the excess minority carrier distribution can be described by the continuity equation (Equation 3.1):

$$D_p \nabla^2 \Delta p(r) - \frac{\Delta p(r)}{\tau_p} + g(r) = 0 \quad (3.1)$$

where  $D_p$  is the diffusion constant of minority charge carriers,  $\Delta p(r)$  is the density of excess minority charge carriers,  $\tau_p$  is the minority charge carrier life time while  $g(r)$  is the generation volume function for the electron-hole pairs induced by light or electron beam. For LBIC measurements with a Gaussian laser beam incident on a solar cell device as illustrated in Figure 3.2,  $g(r)$  can be expressed as [104]

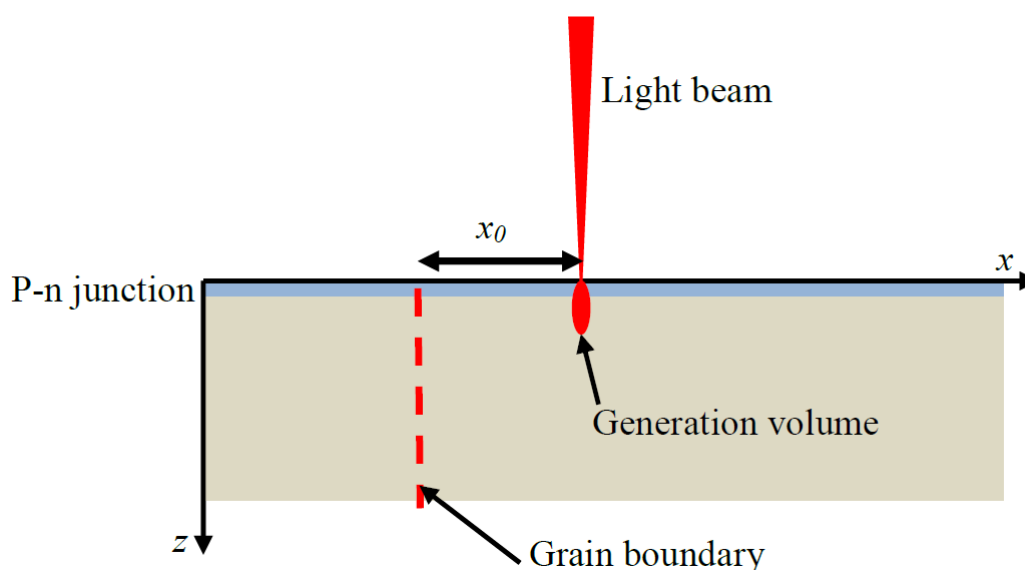


Figure 3.2: Schematic illustration of the generation volume of a solar cell device.



$$g(r) = g_0 e^{-\left(\frac{x^2+y^2}{\sigma^2}\right)} e^{-(\alpha z)} \quad (3.2)$$

where  $g_0 = \phi\eta\alpha(1 - R)$  and  $\alpha$  is the absorption coefficient for the laser wavelength,  $\eta$  the quantum efficiency,  $\phi$  is the maximum flux density of the laser beam,  $R$  the reflection coefficient while  $\sigma$  is the beam radius. The beam radius is defined as the radius at which the amplitude of the beam decreases by a factor  $\frac{1}{e}$ . The light beam carrier generation is not uniform over the generation volume but is highest closest to the surface and the beam axis [105]. The measured current collected at the junction is given by Equation 3.3

$$I = qD_p \int dx \int dy \left( \frac{\partial \Delta p}{\partial z} \right)_{z=0} \quad (3.3)$$

where  $q$  is the magnitude of the electronic charge and the junction is assumed to be an infinitely recombinative surface [104].

### 3.3.3 Beam probe intensity

The intensity and spectral composition of the beam determines the generation profile. The magnitude of the photo-generated current in a single junction solar cell is directly proportional to the intensity of the incident beam of a particular wavelength as long as the power of the incident beam is low enough to avoid high injection that could lead to changes in the local transport properties [86] and or thermal effects. Typical laser beam power used in this thesis for LBIC measurements using a 660 nm wavelength laser was 4 mW, corresponding to an injection of  $\sim 1.3 \times 10^{16}$  photons per second. If the active surface is uniform and larger than the spot size of the beam, the magnitude of the photo-generated current will be independent of the focusing level since the number of incident photons is constant irrespective of the level of focusing [106]. However, localised inhomogeneities such as variations in the series and shunt resistances of the device will influence the strength of the photo-generated current. Due to the strong dependence of the photo-generated current on the intensity of the beam, it is important that the laser output is stable to avoid uncertainties in the measured signal that could be misinterpreted as localised defects.

### 3.3.4 System resolution

The system resolution is an optimisation of the scanning time for a given area and the diameter of the beam. The scanning time for a given area is determined by the scanning step size which is itself related to the spot size (diameter) of the beam probe while the diameter of the beam probe is determined by the focusing system. Generally, the spatial resolution is limited by the spot size and the scanning step size. The smaller the step

size, the higher the resolution. However, the step size should not be much smaller than the spot size for a better resolution to be obtained. The scanning time can range from few seconds to tens of hours depending on the resolution. LBIC permits very high spatial resolution but is time consuming. As a result, low resolution maps are usually taken first to identify regions of interest, from where high resolution maps are then taken. It should be noted, however, that most of the LBIC systems for research purposes are not optimised for scanning time. In principle, the resolution is also limited by the diffusion length of the minority carriers in the material, especially for materials with large diffusion length and low absorption coefficient such as silicon [94]. As the beam enters the material, divergence occurs leading to an effective spot size which increases as the beam penetrates the material.

### 3.4 System development

The LBIC system was locally designed and built at the Centre for Energy Research (CER), Department of Physics, Nelson Mandela Metropolitan University (NMMU), to measure the spatial uniformity of the solar cell response to light when the solar cell device is spot illuminated using laser light as a beam probe. This was realised by placing the sample cell under a fixed laser beam while moving the sample in a raster pattern using a computer controlled sample positioning system. The apparatus in general consists of three sub-systems i.e. the Optics , sample positioning and the electronics sub-systems. The details of the system are shown schematically in Figure 3.3.

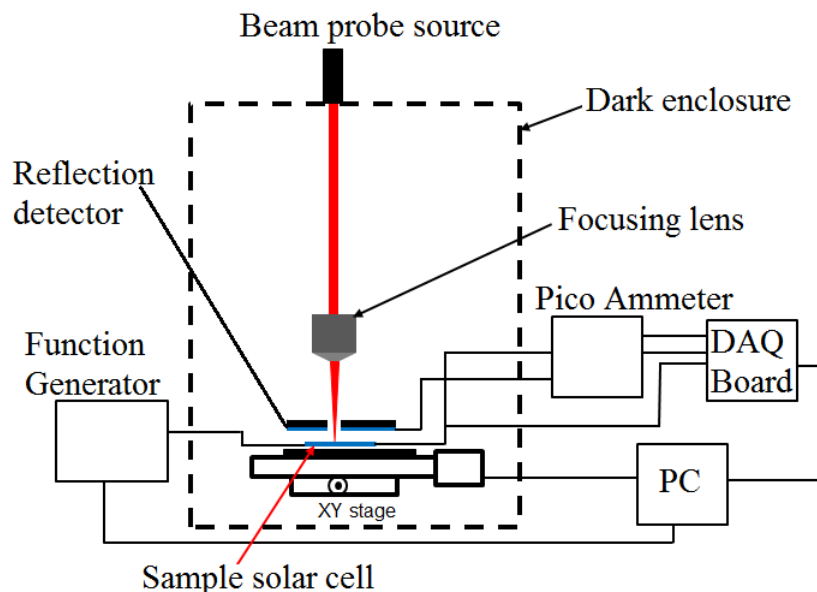


Figure 3.3: Schematic diagram showing the main components of the LBIC system.

The measurement system was compactly designed so that it can be adapted for outdoor

measurements using the sun as the beam probe (S-LBIC) by placing it on a two axis sun tracker as shown in Figure 3.4.

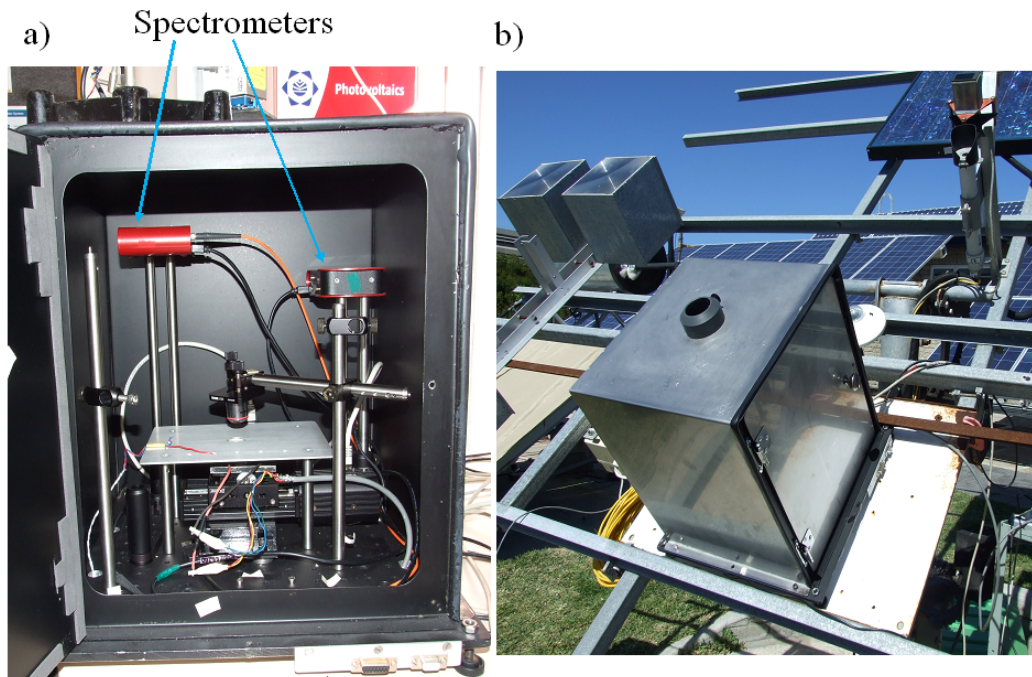


Figure 3.4: LBIC system built for indoor and outdoor measurements: a) Showing main components in a dark enclosure b) System on a two axis tracker for S-LBIC measurements.

In addition, adjustments could be made by incorporating a beam splitter and spectrometers so as to be able to perform spectral measurements. To minimise the effect of external light sources, the system is placed in a dark enclosure with a small opening on top where the light source is placed. External or background light, if not controlled or minimised can affect the photo-response of the solar cell device under investigation, leading to unexpected results.

### 3.4.1 Optics sub-system

The optics sub-system comprises of the laser diodes and the focusing lens. The laser diodes used are coherent cube lasers from Coherent CUBE™ [107] (785 nm/40 mW, 660 nm/60 mW and 445 nm/40 mW) with built in photodiodes to monitor the laser output power level and the temperatures of the diode and its base. The laser system, mounted on a heat sink for cooling and operated in continuous wave (CW) mode, was fixed above the translation stages, thus allowing for the sample to be moved under a stationary laser beam while scanning. In order to control the output power level using a computer, a USB interface was used. Control of the power output of the lasers ensures that the beam probe power is low enough to avoid carrier saturation due to high injection as well

as heating of the sample under investigation. Choice of the wavelength of the laser used is also important since it determines the penetration depth of the incident photons. The penetration depth also depends on the absorption coefficient of the material. In general, longer wavelengths (lower photon energies) penetrate deeper into the material before they are absorbed than shorter wavelengths. In addition, use of light sources of different wavelengths to scan the sample can help to reveal defects at different depths within the sample, thus allowing the investigation of different layers of the solar cell device. The focusing lens used for LBIC measurements is a  $4\times$  microscope objective with a numerical aperture of 0.1 and a working distance of  $18.5\text{ mm}$ . This large working distance allows room for cell contacts and mounting of the reflection detector above the sample solar cell. For S-LBIC measurements, a  $15\times$  reflective microscope objective from Thor-Labs [108] was used. This reflective objective focusing lens system consists of reflective surfaces that focus light without introducing chromatic aberration. It has a numerical aperture of 0.3 and a working distance of  $24.1\text{ mm}$ . An appropriate spot size was obtained by manually adjusting the position of the lens relative to the sample to optimise its focal length.

### 3.4.2 Sample positioning

Accurate positioning of the solar cell is very important for LBIC measurements. To realise this, positioning of the sample under a fixed light beam was achieved using two identical computer controlled VT-80 translation stages from PI Micos, Germany [109]. The translation stages are equipped with integrated limit switches and motorized with 2-phase bipolar stepper motors. A back-lash free re-circulating ball bearing along with a back-lash compensated lead screw ensures quiet and smooth motion. Command programming and configuration is executed via a RS232 interface, which allows setting of the motion parameters of the translation stages and point-to-point moves. Each stage has a travel limit of  $51.47\text{ mm}$ , a uni-directional repeatability down to  $0.4\text{ }\mu\text{m}$  and a maximum speed of  $13\text{ mms}^{-1}$ . The two stages are fixed into an XY assembly as shown in Figure 3.5 and tuned for optimum performance using a computer controlled custom made LabView program.

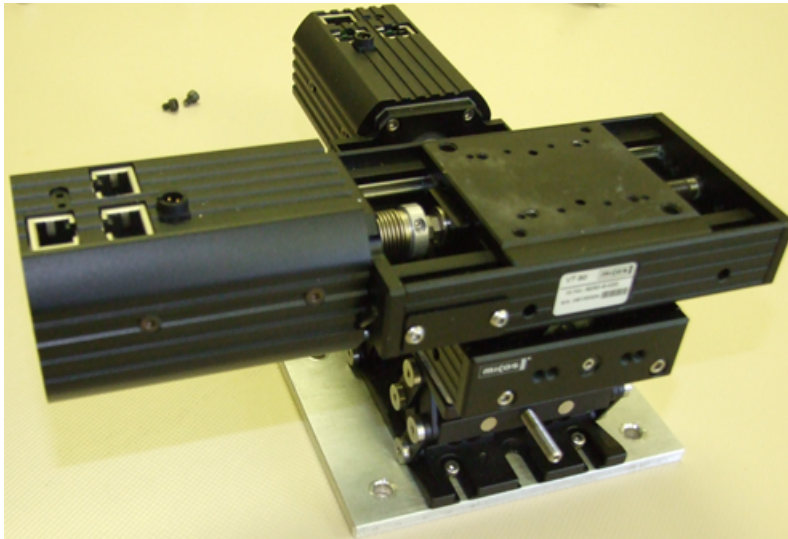


Figure 3.5: XY translation stages.

### 3.4.3 Electronics sub-system

The photo-generated current from a solar cell may vary depending on the incident beam's spot size, intensity and with position on the surface of the solar cell device, and the solar cell technology. Good control of the input impedance of the current detection electronics is therefore very important to avoid changes in measured current due to loading errors. Small currents such as those generated by a single solar cell may be difficult to measure without amplification. A Stanford Research Systems SR570 low noise current pre-amplifier, with a  $50\ \Omega$  output impedance was used for current amplification. It has sensitivity settings from  $1\text{ pAV}^{-1}$  to  $1\text{ mAV}^{-1}$  that can be selected in a 1, 2, 5 sequence. In addition, an input current offset is available to avoid overloading the amplifier with a DC offset current. The pre-amplifier has two identical RC filters whose cutoff frequencies and configuration (high pass or low pass) are controlled from the front panel. These filters were used to minimise the level of noise in the measured signal. More specifications about the amplifier can be found in the amplifier manual [110]. In order to measure the voltage dependence of the photo-generated current, the solar cell was dynamically biased with a sinusoidal wave pattern using an Agilent  $20\text{ MHz}$  Function waveform generator. It is a programmable wave function generator that uses a USB computer interface and has an output impedance of  $50\ \Omega$ . It was used to dynamically bias the solar cell at a voltage step interval of  $0.01\text{ V}$  and frequency of  $10\text{ Hz}$ . The biasing rate was optimised to limit capacitive transient effects [87].

### 3.4.4 Computer control and data acquisition

Integrated into the system is the Labview scanning program that controls the translation stages using an RS232 interface. Biasing of the solar cell using the Function waveform generator and data acquisition with a National Instruments simultaneous sample and hold data acquisition device are integrated into the scanning program and are controlled through a USB interface.

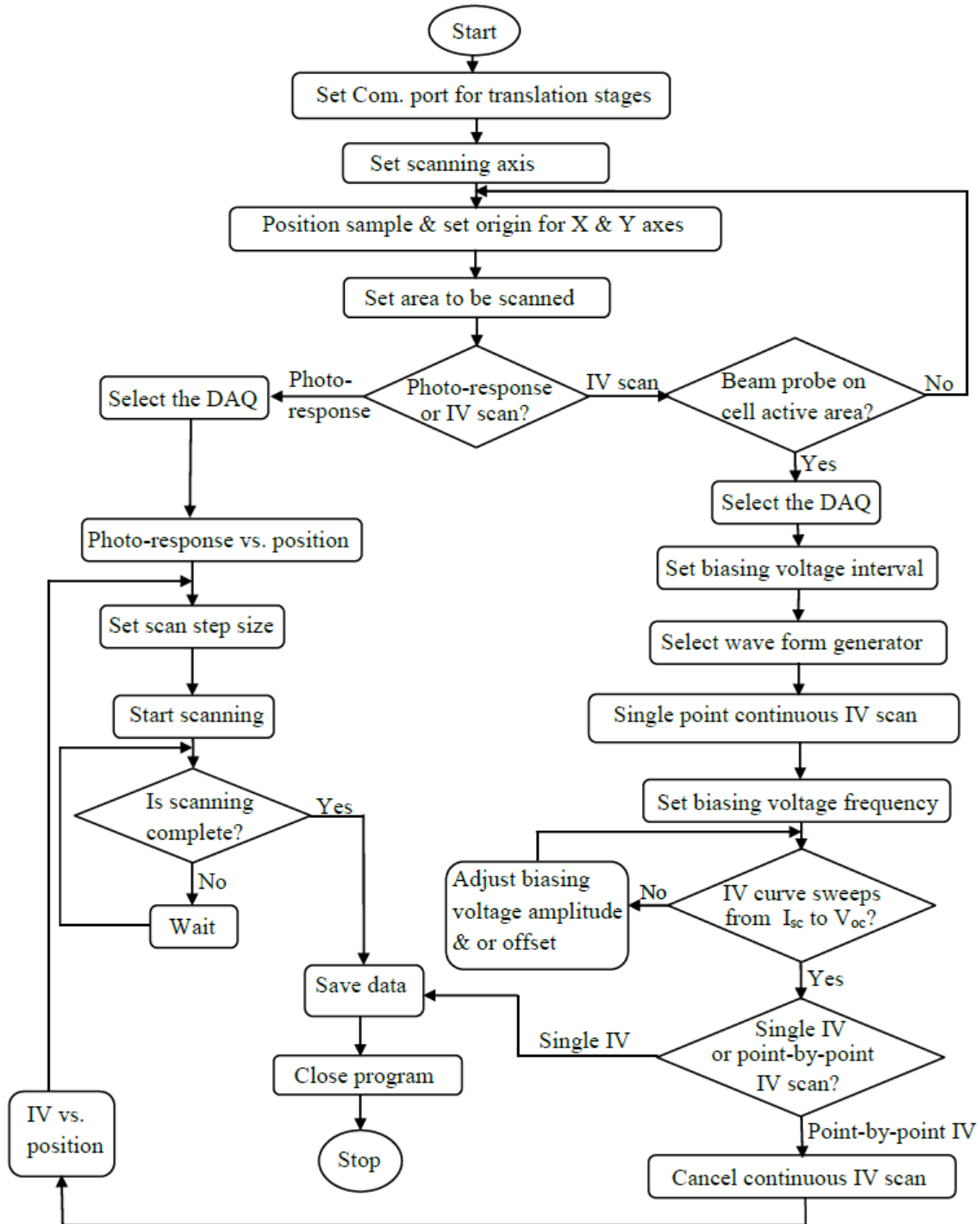


Figure 3.6: Flow diagram for the scanning program.



Shown in Figure 3.6 is a flow chart diagram showing a sequence of steps through which the program is ran to take a scan. A screenshot of the front panel of the main window for the program is shown in Figure 3.7.

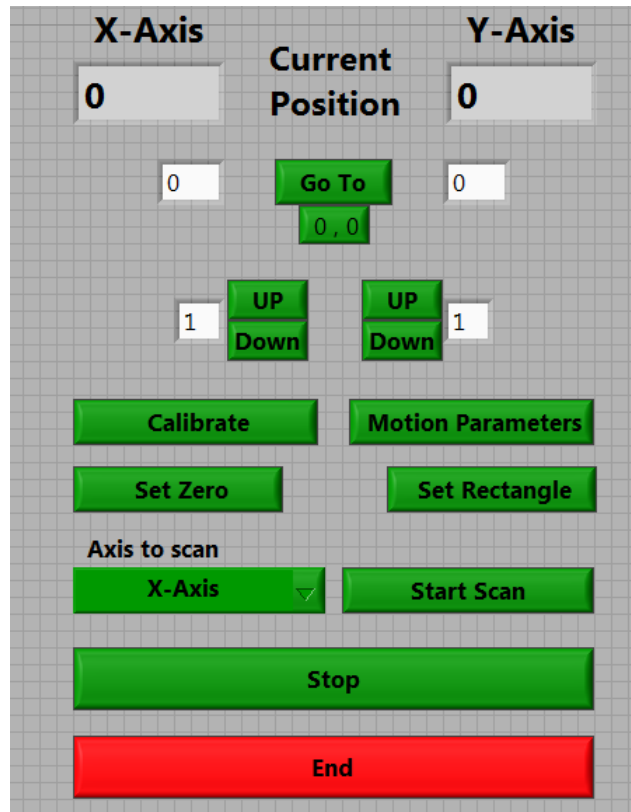


Figure 3.7: Front panel of the main window of the Labview scanning program.

When the program is started, it prompts the user to select the Virtual Instrument Software Architecture (VISA) resource name (com.port) for the translation stages to start communication between the computer and the translation stages. Once communication has been established, the user can, if necessary, calibrate the translation stages and adjust the motion parameters such as velocity and acceleration using the “Calibrate” and “Motion Parameters” buttons shown in Figure 3.7 as well as setting the scanning axis. The sample position is adjusted using the “UP/DOWN” or “Go To” buttons to ensure that it is well positioned relative to the beam probe, before setting the starting point (origin for the axes) using the “Set Zero” button. After setting the origin for the axes, the sample is moved using the “UP/DOWN” or “Go To” buttons to select the area to be scanned, which is then set using the “Set Rectangle” button. If I-V measurements are to be taken, the user should ensure that the incident beam is focused on the active area of the sample. By clicking on the “Start Scan” button, the program prompts the user to select the DAQ device, biasing voltage interval and the VISA resource name for the waveform generator, before opening another window from which the type of scan to be performed is selected. This window is shown in Figure 3.8.

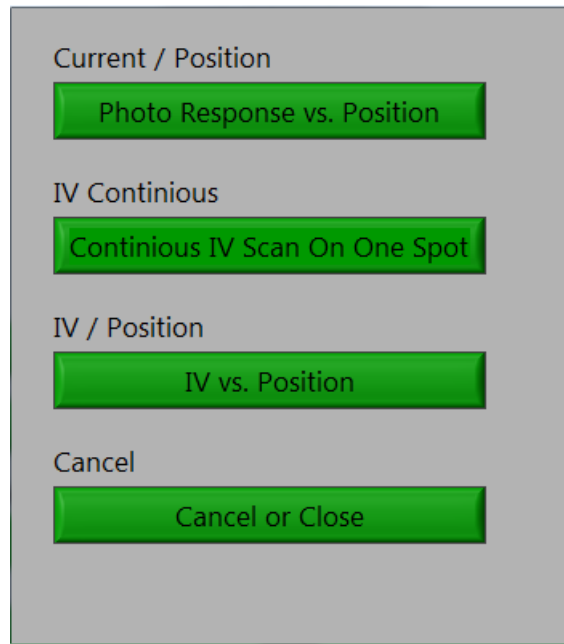


Figure 3.8: Screenshot of the scan type selection window.

It should be noted that the photo-response scan is performed with no voltage bias applied to the sample. To perform point-by-point I-V measurements (“IV vs. Position”), a continous I-V scan on a single spot is first carried out to set appropriate biasing frequency and to ensure that the I-V curve is sweeping from  $I_{sc}$  to  $V_{oc}$ . This is done by adjusting the biasing voltage amplitude and or the voltage offset from the continous I-V curve window shown in Figure 3.9.

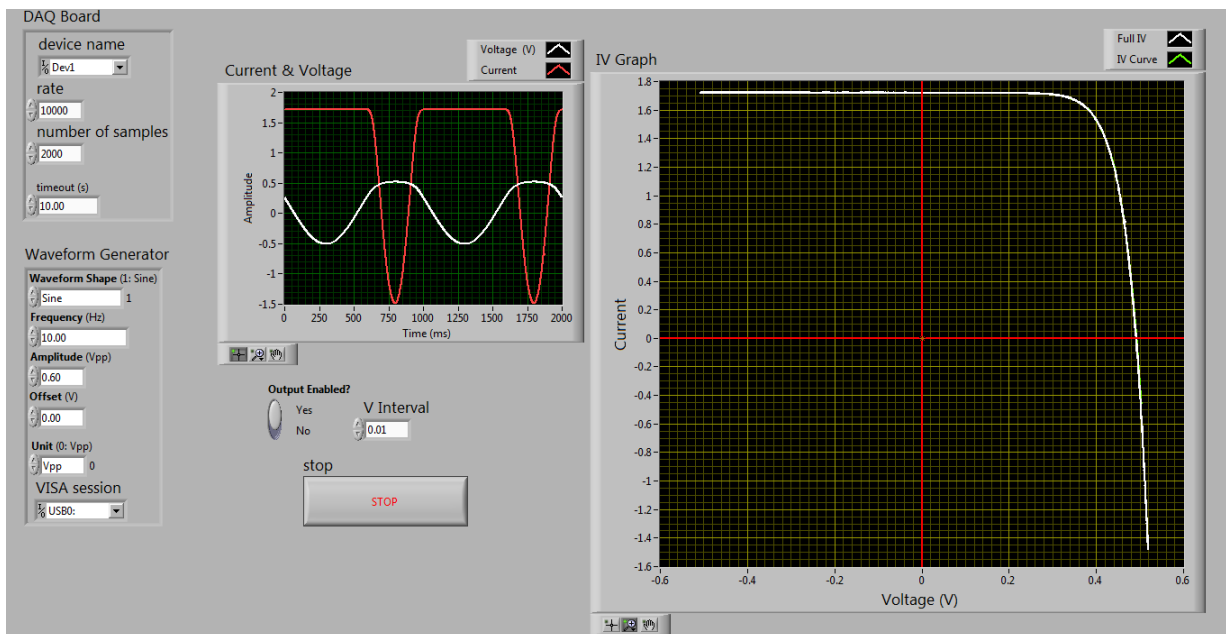


Figure 3.9: Screenshot of the single spot continous I-V curve measurement window.

Once this is done and the user is satisfied with the shape of the I-V curve, the continous



I-V curve measurement is stopped, which will prompt the user to save the data. The single I-V data can be saved or the scan cancelled without saving the data, which will close the single spot continuous I-V measurement window, taking the user back to the scan type selection window (Figure 3.8). From this window, point-by-point I-V measurements are performed using the “IV vs. Position” button that opens another window from where the user will specify the scanning step size and start the scan or cancel the scan if necessary. This window has an option that allows the user to change the scanning axis, if necessary. Once the scanning is completed, the program prompts the user to save the data and stop the program or start another scan.

### 3.4.5 Reflection measurements

Reflection from the sample reduces the amount of radiation that can be absorbed and thus reduces the short circuit current of the solar cell. The magnitude of photo-induced current measured by the reflection detector largely depends on the intensity of the reflected beam which is in turn determined by the reflecting surface. By comparing the reflected signal from the reflection detector with the photo-response map from the sample under study, information about surface features of the sample can be obtained. This information can be used to locate and determine the presence of optical impediments and to distinguish them from other current reducing features such as shunts. The reflection detector used in this study was a  $155 \times 80 \text{ mm}^2$  multi-crystalline silicon (mc-Si) solar cell fixed  $10 \text{ mm}$  above the sample and with  $\sim 4 \text{ mm}$  diameter hole at its centre for the incident beam to pass through to the sample solar cell. This is shown in Figure 3.10.

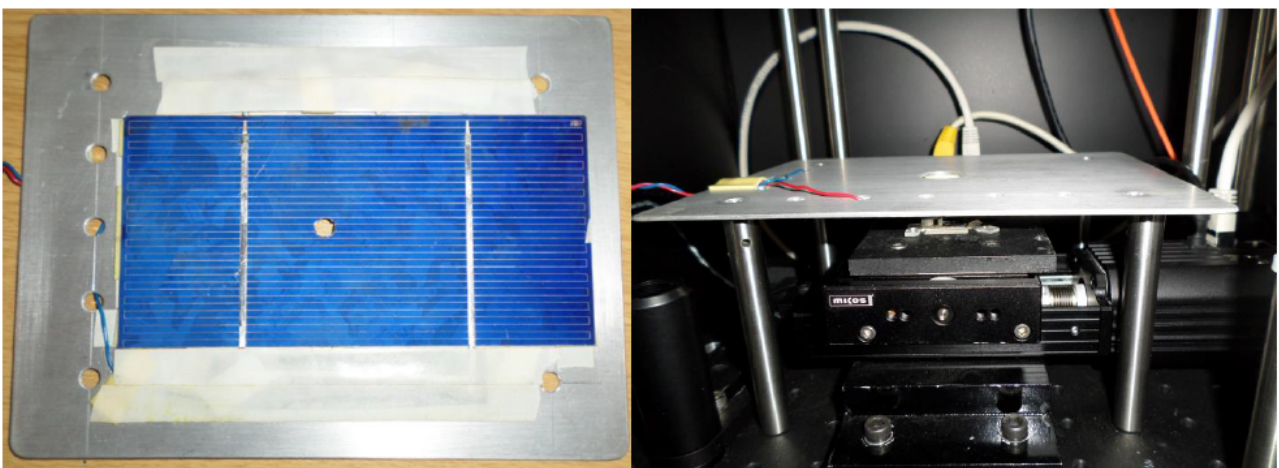


Figure 3.10: Reflection detector before and after mounting above the stage.

### 3.5 Spot illuminated solar cell model

When a solar cell is spot illuminated, only a small area of the cell as given by the diameter of the beam probe is illuminated while the bulk part of the cell is in the dark, with little or no photo-generation at all. This can be considered as two subcells i.e. the “illuminated subcell” and the “dark subcell”, connected in parallel, with each subcell represented by the single diode model as shown in the equivalent circuit diagram in Figure 3.11.  $R_{shL}$  and  $R_{shD}$  in the circuit diagram represent the shunt resistances for the illuminated and dark subcells respectively while  $R_{sL}$  and  $R_{sD}$  are the corresponding series resistances. If the shunt resistances for the dark and illuminated subcells are combined into a lumped shunt resistance  $R_{sh}$  and similarly for the series resistances into a lumped series resistance,  $R_s$ , the  $I - V$  characteristic of a spot illuminated solar cell can be expressed by a two diode model as

$$I = I_L - I_{oL} \left[ e^{\frac{q(V+IR_s)}{n_L kT}} - 1 \right] - I_{oD} \left[ e^{\frac{q(V+IR_s)}{n_D kT}} - 1 \right] - \frac{V + IR_s}{R_{sh}} \quad (3.4)$$

where  $I_L$  is the light generated current,  $I_{oD}$  and  $I_{oL}$  are the saturation currents for the dark and illuminated subcells respectively while  $n_D$  and  $n_L$  are the corresponding ideality factors. Though the model does not fully account for all the carrier transport and recombination paths, it is a useful starting point to understanding solar cells’ behaviour under spot illumination.

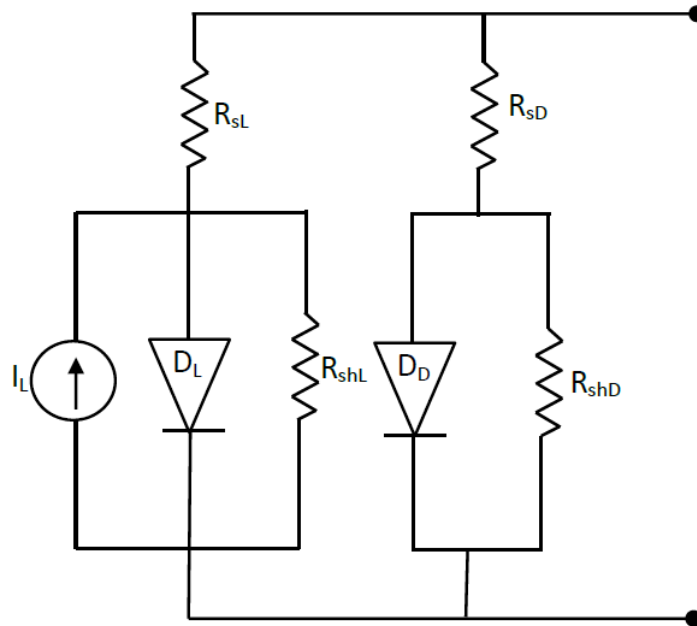


Figure 3.11: Equivalent circuit diagram of a spot illuminated solar cell.

Since the beam spot is always very small compared to the bulk of the solar cell in the dark, the diode recombination properties of the dark subcell may be regarded as con-

stant with respect to beam position. It should be noted that for spot illumination of a solar cell, the current measured indicates the whole solar cell material's response to being spot illuminated and depends on the size of the beam spot. Integration of current obtained at all measurement points over the cell surface may therefore not necessarily give the current measured under full cell illumination due to differences in the generation volume and the possibility of the beam spot overlapping certain areas, depending on the scanning step size.

### 3.6 Multi-crystalline silicon solar cell photo-response mapping

Multi-crystalline silicon (mc-Si) contributes more than 50% of the total Si for PV applications and this percentage is expected to rise tremendously [111]. It is mainly produced from a low grade feedstock that consists mainly of materials that do not meet the specifications of the microelectronics industry and quite often, contain a high concentration of impurities and electrically active defects like dislocations and grain boundaries (GBs) which act as sites of excessive recombination.

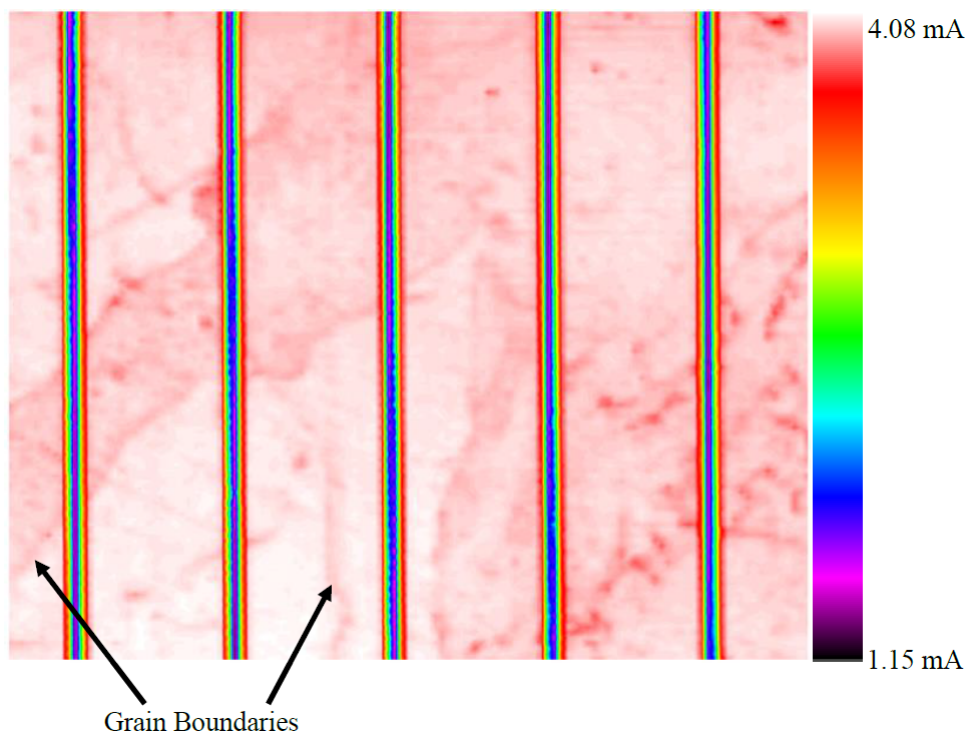


Figure 3.12: Short circuit current ( $I_{sc}$ ) map of a mc-Si showing grain boundaries.

These defects and impurities are detrimental to the minority carrier lifetime and thus to the efficiency of these solar cell devices. In addition, the defects may be localised shunt regions that affect the fill factor and the  $V_{oc}$  of the device and so need to be identified

and characterised. In this section, a  $40 \times 40 \text{ mm}^2$  sample cell cut from a  $155 \times 80 \text{ mm}^2$  mc-Si solar cell was used for LBIC measurements. Variations in spatial uniformity of the mc-Si solar cell device were examined in terms of photo-response uniformity using a  $660 \text{ nm}$  wavelength laser. The results of the  $I_{sc}$  mapping are shown in Figure 3.12 in which the metallic current collection grids (fingers) at the surface of the cell are clearly visible due to the shadowing effect. The finger metallisation act as optical blockages that reflect the incident light as revealed by an increase in the reflection detector signal at these positions in the reflection map shown in Figure 3.13. Also observed are grain boundaries which appear as irregular lines with reduced photo-current in the  $I_{sc}$  map. The different grains show variations in the current collection which is attributed to the differences in light absorption as well as crystal grain orientation that result in more incident light being scattered.

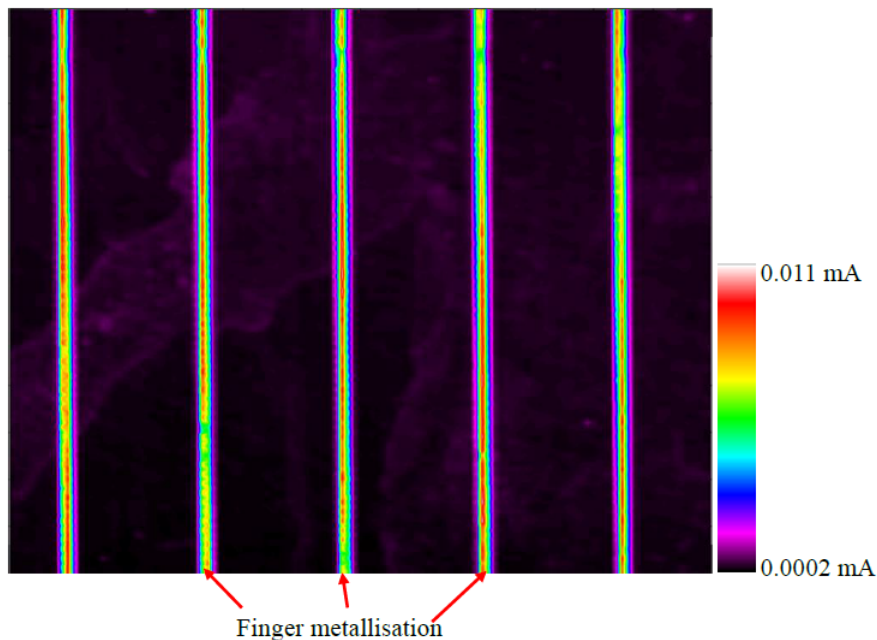


Figure 3.13: Reflection map of a mc-Si solar cell.

When the light beam is incident on the solar cell surface in the vicinity of the grain boundary, some of the generated minority carriers recombine at the grain boundaries, leading to a local reduction in the number of photo-generated charge carriers collected by the p-n junction and hence a reduction in the photo-response. The GB interface states play a dominant role in determining the electronic and photovoltaic properties of mc-Si by acting as traps and recombination centres for the photo-generated carriers due to the presence of deep or shallow levels, depending on the level of impurity decoration [112]. It is also observed in Figure 3.12 that the contrast along the GBs is not uniform. This is attributed to the fact that GBs act as sinks for impurities. Their level of activity can therefore be explained in terms of impurity accumulation in the GB strain field [39].

GBs affect the performance directly by a current and voltage drop due to recombination or indirectly by a voltage drop induced by local fixed charges [104]. The impact of GBs on device performance has been studied by various authors [89, 103, 104, 113] and their effects and transport properties have shown to involve complex phenomena such as an injection dependant potential barrier induced by charged defects at the GB which influences its recombination strength [114]. Donolato [89] derived an expression to describe the LBIC or EBIC (electron beam induced current) contrast,  $C(x_0)$ , across a semiconductor grain boundary given by

$$C(x_0) = \frac{[I_0 - I(x_0)]}{I_0} \quad (3.5)$$

where  $I_0$  is the background current at a large distance from a grain boundary,  $I(x_0)$  is the beam-induced current in the vicinity of a grain boundary as illustrated in Figure 3.2. The GB line itself therefore does not give a contrast but its the surrounding environment that gives it a contrast. It should be noted, however, that due to the difference in electrical activities of GBs, their influence on LBIC profile differs. In general, the effects of GBs depend on the microstructure, grain size distribution, junction depth as well as doping [115].

## 3.7 Conclusion

In this Chapter, various LBIC systems that have been developed over time have been reviewed. Their development was partly driven by the need to improve the resolution of the systems as well as availability of new technologies that have resulted in improvement in scanning speeds and accuracy. The LBIC mapping technique has proved to be an effective technique that reveals spatial inhomogeneities in PV systems and devices, it is non-destructive and has a relatively high resolution. The spatial resolution of the system is partly determined by the scanning step size and the diameter of the focused beam. The Chapter also described the LBIC/S-LBIC system that was designed and compactly built to be used for indoor and outdoor measurements. A model for a solar cell under spot illumination was presented and discussed. Photo-response mapping results for a mc-Si solar cell obtained using the system were also presented and discussed. The system was used to obtain indoor measurements using lasers as beam probes and outdoor measurements (S-LBIC) to characterise concentrator solar cells whose results are presented in Chapter 5.

# Chapter 4

## Solar cell parameter extraction

### 4.1 Introduction

Improving the efficiency of solar cells requires an understanding of the physical processes that determine their performance. Solar cell performance is normally assessed by measuring the I-V characteristics under specific conditions and then extracting the I-V parameters from the measured data. The solar cell I-V characteristics are often described by the diode models, as given by Equations 2.31 and 2.46. The model parameters are closely related to the internal physical mechanisms that occur in the solar cell and so their knowledge is important in understanding the processes involved. Solar cell parameter extraction has been a research topic for many years and several articles have reviewed different parameter extraction methods over time. Generally, there are two approaches that have been used to extract solar cell parameters from I-V measurements taken either in the dark [116, 117] or under illumination [118, 119, 120, 121], viz: analytical techniques [122, 123, 124, 125] and numerical extraction techniques [126, 127, 128]. Extraction of I-V parameters based on numerical techniques use algorithms to fit computed I-V characteristics to the measured ones, which may require significant computational effort due to the non-linearity and implicit nature of these equations. Besides, their accuracy depends on the fitting algorithm and the fitting criterion used [127]. Analytical extraction techniques which are normally preferred as they are fast may be inaccurate since they are normally based on simplified formulae [127]. Accurate extraction and interpretation of solar cell parameters is important in improving the device quality and design during fabrication and in device modelling and simulation. In addition, optimisation efforts and quantitative studies to assess the capabilities of various solar cell technologies under various test and operating conditions benefit greatly from accurate extraction and interpretation of the model parameters [124]. In this chapter, an interval division algorithm for the extraction of solar cell parameters from I-V measurements is presented. Results obtained for a mc-Si solar cell in the dark

and under illumination are presented and discussed.

## 4.2 Parameter extraction algorithm

In order to extract device and performance parameters from the matrix of I-V measurements obtained using the LBIC/S-LBIC mapping technique, a curve fitting interval division algorithm based on the diode models was used. The algorithm which was developed in Labview, imports the measured I-V data sets and simulates the I-V curve using either the single diode model given by Equation 2.31 or the double diode model given by Equation 2.46. The simulated I-V curve parameters are then programatically adjusted until the measured and simulated I-V curves are fitted within a set tolerance limit ( $tol$ ) of the parameters. A small  $tol$  value minimises the computational error and enables the algorithm to converge to a more accurate set of parameters but may increase the computational time. The fitting procedure of the interval division algorithm is given in the flow chart in Figure 4.1. Generally, the interval division algorithm obtains solar cell parameters by successively dividing the interval between measured and calculated data sets using a user defined dividing factor. It is based on the Newton iteration method with some modifications as given in Equation 4.1 [120]:

$$f(x+1) = f(x) - \frac{f(x) - f(e)}{l} \quad (4.1)$$

where  $f(x)$  and  $f(e)$  are the calculated and measured (experimental) values, respectively,  $l$  is a user defined factor (convergence factor) that determines the relative speed of convergence. The choice of  $l$  for each parameter is guided by the shape of the modelled curve relative to the measured one on visual inspection as well the speed of convergence. Each of the parameters of the single diode equation, namely:  $I_o$ ,  $R_{sh}$ ,  $R_s$ ,  $I_L$  and  $n$  are initialised and applied to Equation 2.31 to compute and plot the modelled I-V curve. The  $I_{sc}$  and  $V_{oc}$  (measured and modelled) are determined from the intercepts of the axes and compared. The magnitude of the slopes of the linear sections in the low voltage range (LVR) and the high voltage range (HVR) for the experimental and modelled data are also computed to obtain shunt and series slopes, respectively. The magnitude of the difference between modelled and experimental shunt slopes are used to update the modelled shunt resistance until a set criterion is met. Similarly, the difference between the series slopes is used to update the modelled series resistance. There are parameters, however, that cannot be obtained directly from the I-V curve such as the saturation current and the ideality factor. The ideality factor is a measure of the quality of the diode and generally determines the degree of curvature of the “knee” of the I-V curve. Since  $n$  cannot be directly obtained from the measured values, an indirect fitting method has to be identified. This is done by applying an exponential fit to the interpolated current

and voltage values at the “knee” of the I-V curve to obtain a damping factor value that determines the curvature.

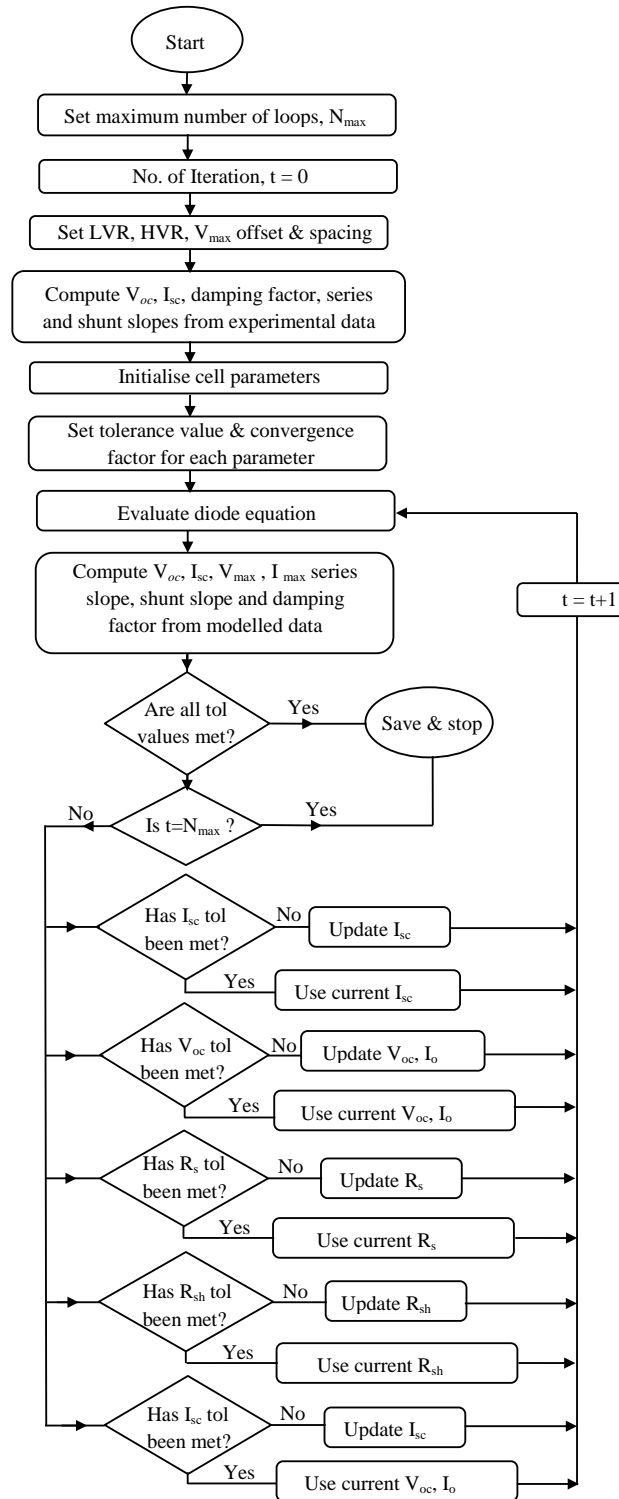


Figure 4.1: Interval division algorithm flow chart.

The range of the I-V values at the “knee” to which the exponential fit is applied are



determined by setting a voltage offset and spacing from the voltage at the maximum power point. The damping factors of the exponential fit for the measured and modelled I-V curves are then compared and the difference used to update the modelled value of  $n$  until a set tolerance limit is reached. In addition, since  $V_{oc}$  does not appear in the diode equation, other parameters that indirectly affect it (secondary fitting parameters) have to be identified. Adjusting the saturation current  $I_o$  of the modelled I-V curve results in a change in  $V_{oc}$ . The difference in  $V_{oc}$  obtained from the measured and modelled I-V curves is, therefore, used to update  $I_o$ . The measured and modelled (fitted) I-V curves are plotted on the same axis which allows visual inspection and monitoring of the curve fitting process. The program automatically saves the extracted parameters once the set tolerance limits have been met or the maximum number of iterations set has been reached before it terminates. A screen shot of the Labview Front Panel of the parameter extraction algorithm is shown in Figure 4.2.

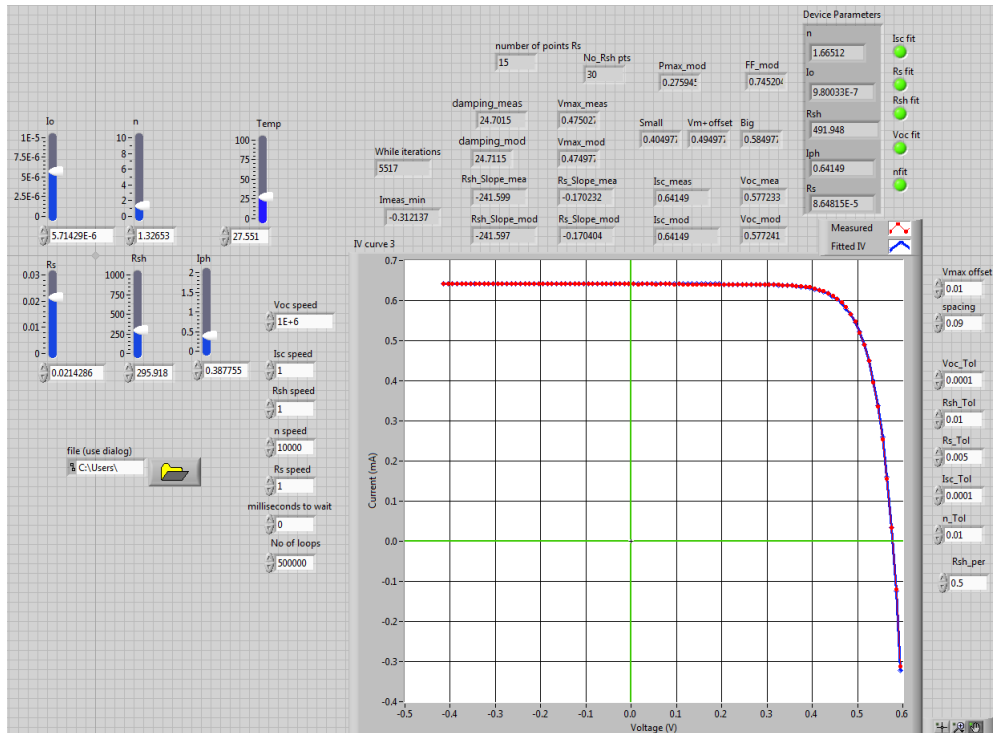


Figure 4.2: Screenshot of the Labview Front Panel for the Parameter extraction algorithm .

The parameter extraction algorithm was applied to I-V measurements of a multi-crystalline silicon solar cell obtained in the dark and under illumination conditions to test its performance and accuracy and the results are presented in the following section.

### 4.2.1 Goodness of fit

To test how well the calculated I-V curve fits the measured I-V curve, the goodness of fit,  $R^2$ , value is calculated. The  $R^2$  value is defined as

$$R^2 = 1 - \frac{SS_{res}}{SS_{tot}} \quad (4.2)$$

where  $SS_{res}$  is the sum of the squares of the residuals while  $SS_{tot}$  is the total sum of squares, which is proportional to the sample variance.  $SS_{res}$  and  $SS_{tot}$  are given by

$$SS_{res} = \sum_j (I_j^m - I_j^c)^2 \quad (4.3)$$

$$SS_{tot} = \sum_j (I_j^m - \bar{I})^2 \quad (4.4)$$

where  $I_j^m$  is the  $j^{th}$  measured current value and  $I_j^c$  is the corresponding calculated current value while  $\bar{I}$  is the mean measured current. Since the calculated goodness of fit is for the whole I-V curve, it gives an indication on how well the modelled I-V curve fits the measured I-V curve. Values of  $R^2$  close to 1 indicate a good fit.

## 4.3 Multi-crystalline silicon solar cell I-V parameters

The I-V characteristics of a multi-crystalline silicon solar cell in the dark and under illumination were obtained to extract device and performance parameters. These parameters give a basic indication of the functioning of the device and their extraction and interpretation is important for the quality control and evaluation of the performance of solar cell devices. The extracted parameters obtained using the interval division algorithm are presented and discussed.

### 4.3.1 Dark I-V characteristics

Dark I-V measurements are obtained by injecting carriers into the circuit with electrical means rather than with light sources. As a result, current flows into the cell as opposed to current flow out of the cell under illumination conditions. However, the electrical configuration still results in the cell's p-n junction being in forward bias as during typical operation and so dark I-V measurements can be used to analyse the electrical characteristics of a cell just like light I-V measurements [129]. Dark I-V measurements show how a solar cell device operates as a diode and are invaluable in obtaining information about device parameters which can be deduced from the shape and linearity of the measured curve at different current levels. They, however, do not provide information about

performance parameters.

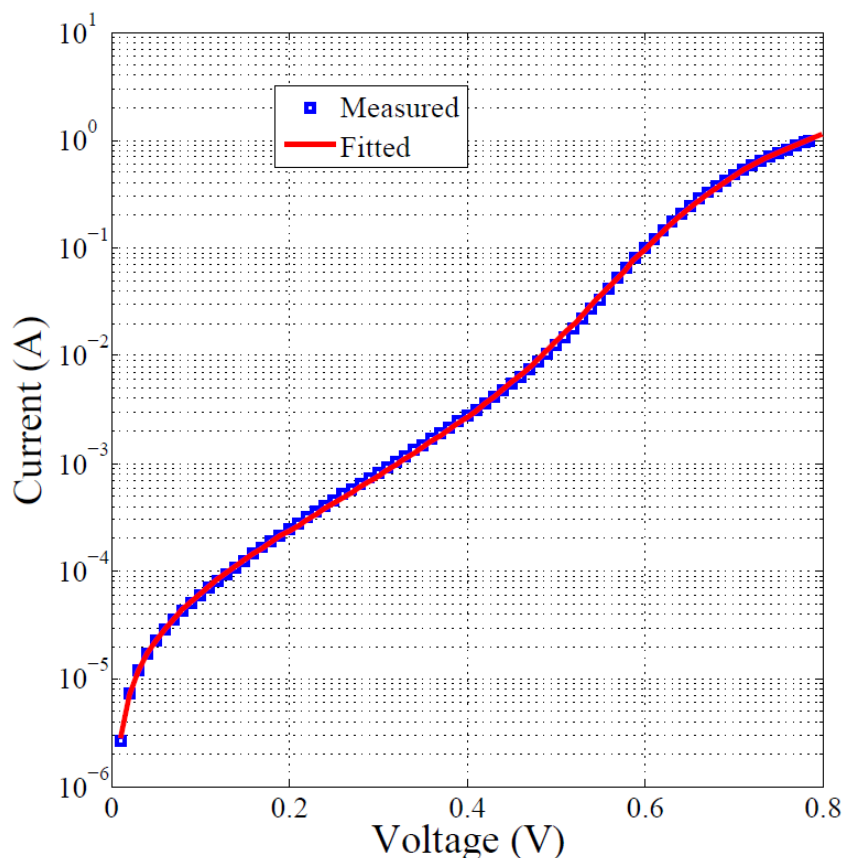


Figure 4.3: Measured and fitted Dark I-V curve for a mc-Si solar cell.

The curvature and slope of the curve in the low current region (LCR) are determined by the parameters  $R_{sh}$ ,  $I_o$  and  $n$  while  $R_s$  determines the shape in the high current region (HCR). Large curvature in the LCR and the HCR is an indication of low shunt and high series resistances, respectively, while an inflection in the curve around mid current level region may signify the presence of non-ideal carrier recombination losses [129]. To obtain dark I-V measurements, the mc-Si solar cell was put in a dark enclosure so as to eliminate light generated current and dynamically biased using an Agilent wave form generator with a sinusoidal wave at a frequency of 10 Hz. The measured I-V values were fitted to extract device parameters. The measured dark I-V curve exhibited a clear double diode I-V characteristic and so was fitted using the algorithm based on the double diode model. The results of the dark I-V curve fitting are shown in Figure 4.3 where we observe good agreement between measured and fitted I-V curves. The calculated  $R^2$  value was 0.999, which represents a 0.1% deviation. The influence of the series and shunt resistances in the high and low current regions is also clearly visible in the figure. The extracted parameters based on the double diode model are given in Table 4.1 where relatively low  $R_{sh}$  and high  $R_s$  values are obtained suggesting that current losses due to parasitic resistances could be substantial. At forward voltage bias range from 0 – 0.15 V,

the dark current is mainly determined by the shunt resistance while at biasing voltages from  $\sim 0.15 - 0.4 V$ , the current flow is dominated by carrier recombination in the space charge region (second diode) with an ideality factor of  $\sim 3.6$ . Between  $0.4 V$  and  $\sim 0.6 V$ , the dark current is dominated by the diffusion current (first diode current) with an ideality factor  $\sim 1.5$  as shown in Table 4.1.

Table 4.1: Extracted dark I-V device parameters for a mc-Si solar cell.

Parameter	$n_1$	$I_{o1}(A)$	$n_2$	$I_{o2}(A)$	$R_s(\Omega)$	$R_{sh}(\Omega)$
Extracted value	1.49	$1.62 \times 10^{-8}$	3.64	$2.98 \times 10^{-5}$	0.097	17.9

At high biasing voltages (greater than  $\sim 0.6 V$ ), the current flow is limited by the series resistance of the device and this shows up as a bending of the curve at very high forward voltage bias as shown in Figure 4.3. An ideality factor close to 1 for the diffusion current is expected [130, 131] while for the recombination current, the ideality factor should be close to 2. The high ideality factor for the diffusion current could be attributed to recombination mechanism in the quasi neutral region (QNR) that results from trap-assisted tunnelling and field-assisted recombination [116] at grain boundaries in mc-Si solar cells. Ideality factors greater than 2 for the recombination current have been previously reported by [132, 130, 133] working on crystalline silicon solar cells and possible explanations proposed. Breitenstein *et al.* [133] attributed the large ideality factor to the effect of multi-level recombination while Beier and Voss [132] have attributed it to the effect of the position and concentration of the recombination centres as well as the capture cross-section area for the charge carriers. The mechanism responsible for the large ideality factor for the recombination current in this case is not apparently clear.

### 4.3.2 Illuminated I-V characteristics

The current in an illuminated solar cell is conventionally described by the dark current-voltage characteristic shifted by the short circuit current according to the superposition principle. I-V measurements obtained under illumination are normally used to characterise solar cells and allow determination of device and performance parameters.

#### 4.3.2.1 Full cell illumination

Current-voltage measurements of a mc-Si solar cell were obtained on a clear day with the sample mounted on a two axis sun tracker. The global solar irradiance as recorded by the pyranometer on the plane of array (POA) was  $1050 Wm^{-2}$ , while the solar cell temperature as recorded by a thermocouple attached to the back of the solar cell was  $27.5^\circ C$ . A curve fitting algorithm based on the single diode equation discussed earlier

was then applied to extract device and performance parameters. The measured and the fitted I-V curves are shown in Figure 4.4

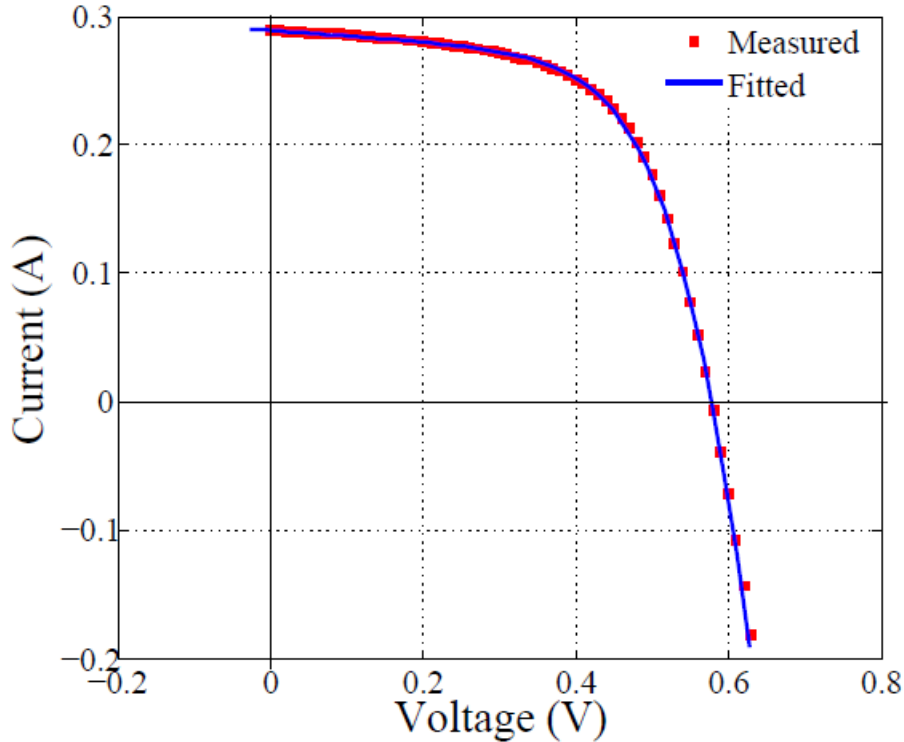


Figure 4.4: Measured and Fitted full cell illumination I-V characteristic of a mc-Si solar cell.

while the extracted parameters are shown in Table 4.2. Good agreement between the fitted and measured I-V curves is observed, with an  $R^2$  value of 0.997, implying that the single diode model is sufficient to describe the behaviour of the illuminated I-V curve.

Table 4.2: Extracted parameters for a mc-Si under full cell illumination.

Parameter	$n$	$I_o(A)$	$R_s(\Omega)$	$R_{sh}(\Omega)$	$I_{sc}(A)$	$V_{oc}(V)$	$FF$
Extracted value	2.30	$1.65 \times 10^{-5}$	0.095	23.34	0.29	0.58	0.62

The I-V curve and the extracted parameters show low shunt resistance, which could be due to the presence of shunt paths within the bulk material that result in current leakage across the junction. The low shunt resistance results in low device fill factor as shown in Table 4.2. The shunt paths may be process induced or due to material induced defects and can be detrimental to the performance of the device. The device also has high reverse saturation current and ideality factor greater than 2, which could be attributed to carrier recombination in the quasi neutral regions on either side of the junction.

### 4.3.2.2 Solar cell under spot illumination

Local variations in solar cell photo-response can be revealed by spot illumination of the device using LBIC imaging technique. These variations can be due to spatial non-uniformities in local properties of the device that determine its performance.

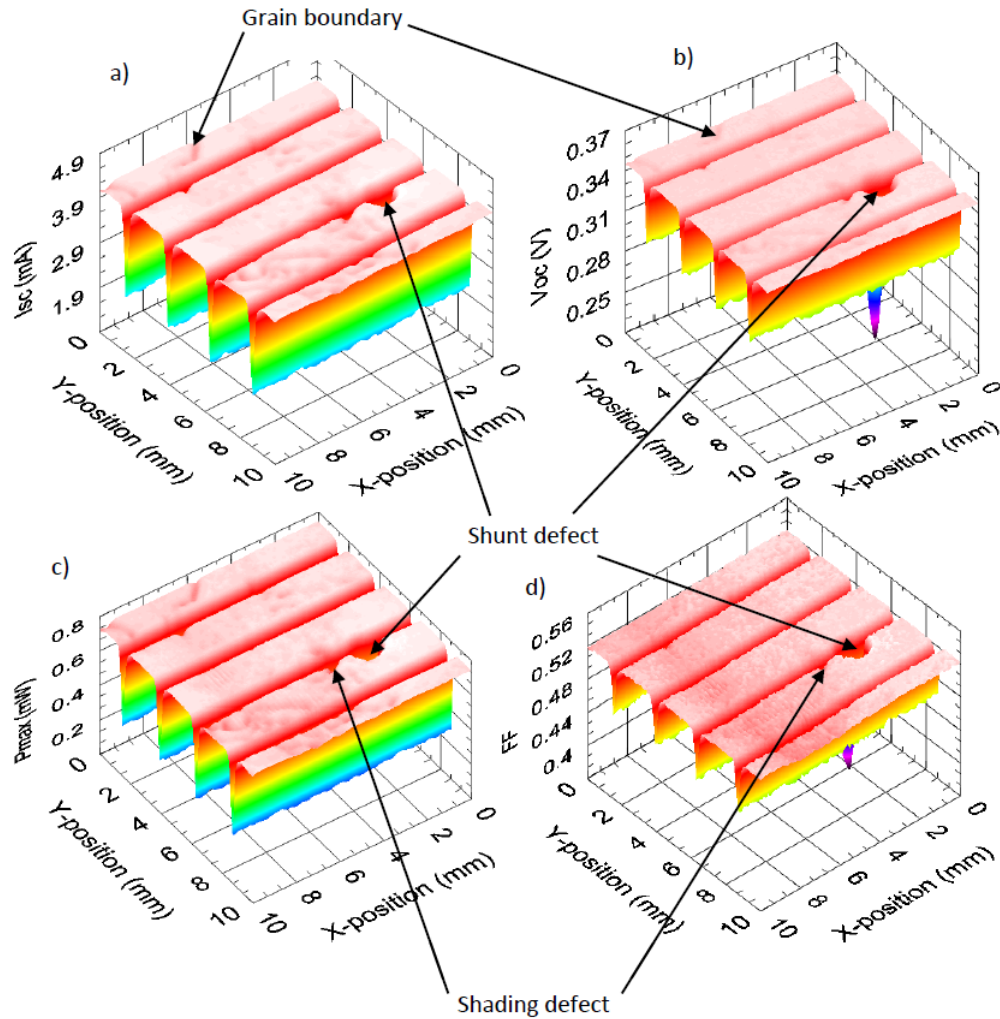


Figure 4.5: Performance parameters of a mc-Si solar cell.

By dynamically biasing the solar cell at each measurement point from reverse bias to a voltage slightly higher than its  $V_{oc}$ , localised point-by-point I-V measurements were obtained using a  $660\text{ nm}$  wavelength laser beam focused to a spot size of  $\sim 180\ \mu\text{m}$ . An area of  $8.1 \times 8.1\text{ mm}^2$  was scanned at a scanning step interval of  $0.1\text{ mm}$ , resulting into 6561 localised I-V curves. Curve fitting was performed on each of these localised I-V curves to extract I-V parameters, thus allowing for mapping of spatial variation of device and performance parameters. The results of device and performance parameters are shown in Figures 4.5 and 4.7. The performance parameter maps in Figure 4.5 show a reduction in the extracted parameters due to the finger grid metallisation as well as the grain

boundary and defects along a finger grid metallisation. The reduction in performance parameters at grain boundaries is due to increase in recombination as already discussed in sub-Section 3.6. A reflection map shown in Figure 4.6 reveals a surface defect (shading defect) that locally blocks the incident beam and results in an increase in reflection over the same area.

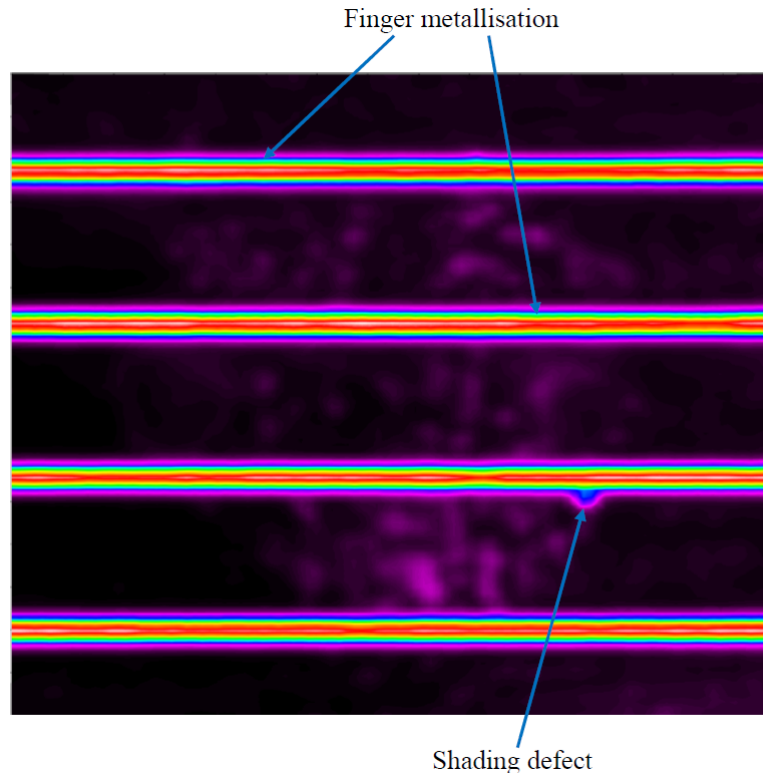


Figure 4.6: Reflection map of a mc-Si solar cell showing a surface defect.

Another performance reducing feature (shunt defect) close to this shading defect did not show any significant change in the measured reflection signal, an indication that this is not a surface but a shunting defect. Shunt defects in solar cells are mainly process induced, with material induced shunts being quite an exception [134]. Such a shunt appearing below the finger could be due to the finger metallisation paste penetrating through the emitter to the base material, which may result into a Schottky shunt defect. In Figure 4.7, the extracted device parameters are presented in which an increase in magnitude of the extracted parameters over the finger metallisation is observed. This increase is generally an artefact due to shading by the finger metallisation. As the light beam moves over a finger metallisation, the effective active area illuminated changes, resulting into current reduction. The maps, however, do not show any significant change in the extracted device parameters over the grain boundaries and the shading defect earlier identified. Grain boundaries that are not strongly recombinative, though visible in LBIC images, may not show measurable shunting effects. In Figure 4.7 (a) and (b), an increase in the ideality factor and saturation current at the shunt defect is observed.



An increase in saturation current over this defect is an indication of increase in recombination and is attributed to a higher density of localised defect states (recombination centres) that cross the p-n junction. Figure 4.7 (c) and (d) show the extracted parasitic resistances in which an increase in series resistance and a decrease in the shunt resistance due to the defect is observed. An increase in series resistance results in a decrease in the fill factor and maximum power as shown by Figure 4.5 (a) and (b), thus affecting the efficiency of the device. The decrease in the shunt resistance over the defect is a clear evidence of significant shunting, providing alternative shunting paths for the photo-generated charge carriers that results in current leakage across the p-n junction, thus lowering the maximum power out, open circuit voltage and the fill factor.

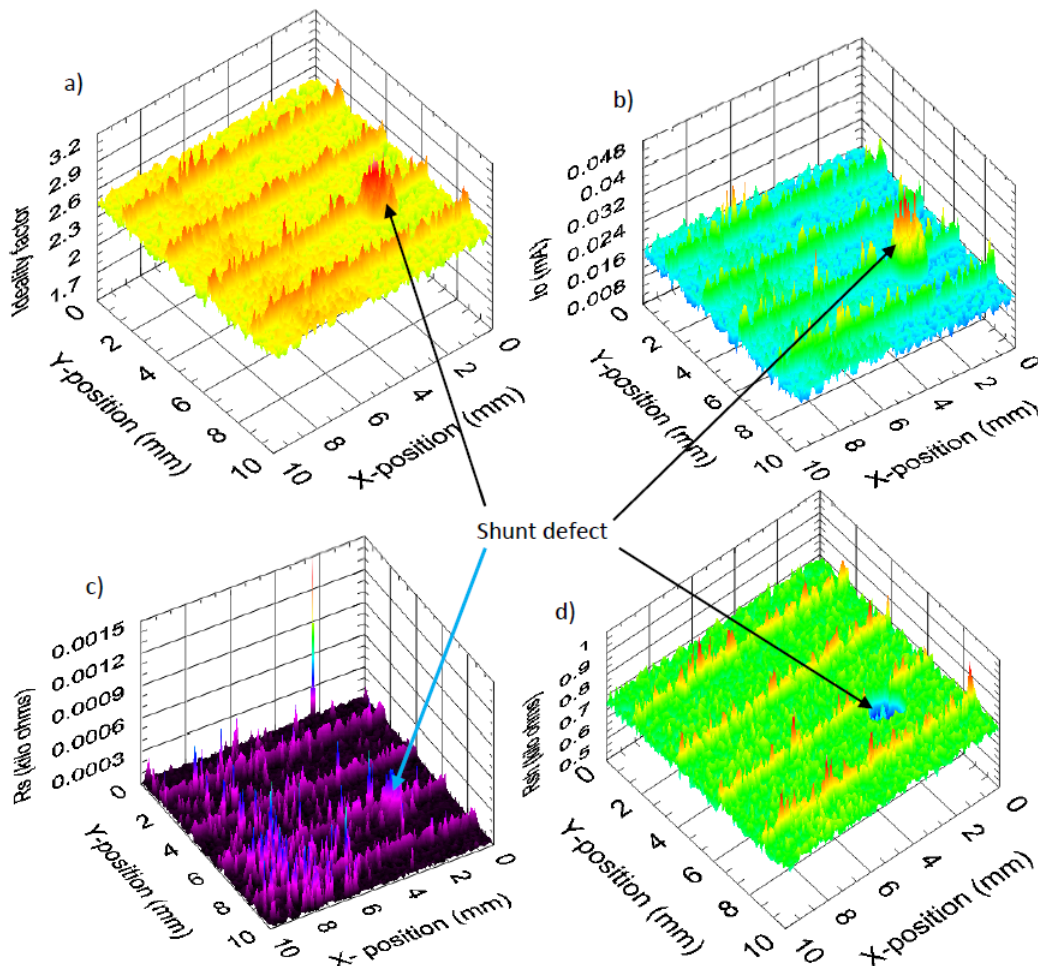


Figure 4.7: Extracted device parameters of a mc-Si solar cell.

## 4.4 Conclusion

An interval division algorithm for solar cell parameter extraction has been described and used to extract parameters for a mc-Si solar cell. The algorithm was applied to I-V



measurements obtained in dark and under illumination conditions to extract device and performance parameters. The parameters give an idea about the functioning of the device. Good agreement between measured and fitted I-V curves were obtained, with high  $R^2$  values, an indication that the algorithm can accurately model the I-V characteristics of the solar cell device. The curve fitting routine was applied to the I-V data matrix obtained using the LBIC mapping technique to extract device and performance parameter maps, from which spatial variations of the device and performance parameters were studied. The parameter maps revealed different types of performance degrading defects such as grain boundaries, optical blockages and shunts that could affect the performance of the device to different extents.

# Chapter 5

## Concentrator solar cell characterisation

### 5.1 Introduction

Solar cell characterisation is an important undertaking both during research work in a laboratory as well as on a production line during manufacturing processes. This is so as to evaluate the performance and improve or maintain the quality of solar cell devices. This may involve illuminating the solar cell and measuring the current and voltage under specific conditions to obtain efficiency and other performance indicators such as fill factor and maximum power. The performance of a solar cell depends on the conversion efficiency of every point of the photoactive material which is in turn affected by the presence of localised defects. High resolution mapping allows visualising and localising current reducing defects such as micro cracks and impurities that act as recombination centres, local optical blockages and shunts that may affect the cell efficiency and cell lifetime. These current reducing features may not be visually detectable. The solar cell may look uniform visually even when there are significant non-uniformities in photo-response over the cell area. The LBIC mapping technique can be used to identify and localise these current reducing features. The solar cell under study is moved in a raster pattern while being point illuminated by a fixed light source to generate a localised current. The generated current represents the solar cell material's response to the incident beam at that point. When the generated current is plotted as a function of position, a photo-response map that enables mapping of carrier generation uniformity over the cell surface is obtained. By dynamically biasing the device from reverse bias to a voltage slightly higher than its  $V_{oc}$ , I-V measurements are obtained from which device and performance parameters can be extracted. In addition, by using beam probes of different wavelengths, the generation depth can be investigated through calculation of photon penetration depth which depends on wavelength, thus making it possible to detect de-

fects within a device cross-section [135]. In this Chapter, characterisation of two types of concentrating solar cell devices: a Back contact Back junction silicon solar cell for low to medium concentration and an InGaP/InGaAs/Ge triple junction solar cell for high concentration is discussed. These devices are characterised in terms of photo-response mapping and parameter extraction.

## 5.2 Back contact Back junction silicon solar cell

Back contact silicon solar cells have attained reasonable efficiencies under laboratory conditions though the manufacturing costs are still quite high. Their efficiencies are limited to some extent by spatial non-uniformities due to localised defects and defects introduced during the manufacturing processes. These defects may introduce energy levels within the forbidden bandgap region that act as recombination centres for the photo-generated charge carriers, resulting in a reduction of the carrier lifetime. Such spatial inhomogeneities can be examined nondestructively by focusing a highly stabilised laser beam onto the surface of the solar cell and measuring the induced photocurrent point-by-point as the beam is moved in a raster pattern across the sample. The photo-generated current is associated with the intrinsic characteristics of the electron-hole recombination and the level of photon penetration into the active material and can therefore give information about photo-current generation uniformity, presence of defects and their recombination strength. Though the solar cell may look uniform on visual inspection, non-uniformities in photo-response may be present which could be due to manufacturing flaws or as a result of device degradation. In addition, extracted device parameters can give an idea about the nature of recombination mechanisms that are dominant within the device. Thus, information from photo-response mapping and parameter extraction can be used to improve manufacturing processes by exposing discontinuities in a cell's photo-response.

### 5.2.1 Photo-response mapping

Figure 5.1 shows the  $I_{sc}$  and reflection map of a back contact back junction (BC-BJ) silicon solar cell obtained using a 660 nm wavelength laser highlighting the importance of LBIC as a mapping technique to identify current reducing defects in solar cells. In this figure, we observe current reducing features highlighted with arrows and a dashed rectangle. Also observed are alternating regions of high and low photo-current generation. The defect shown by the rectangle is a surface defect that reflects the incident beam as confirmed by an increase in the reflection signal over the same area. This defect is a result of the removal of the anti-reflection coating layer due to poor handling of the solar

cell. The current reducing features shown by the arrows were not observed in the reflection detector signal, an indication that these are not surface defects but defects within the bulk of the solar cell device. Such defects could be due to impurities introduced during the device manufacture. Physical examination of the device could only reveal the damage to the anti-reflection coating that caused an increase in the reflection detector signal as already mentioned.

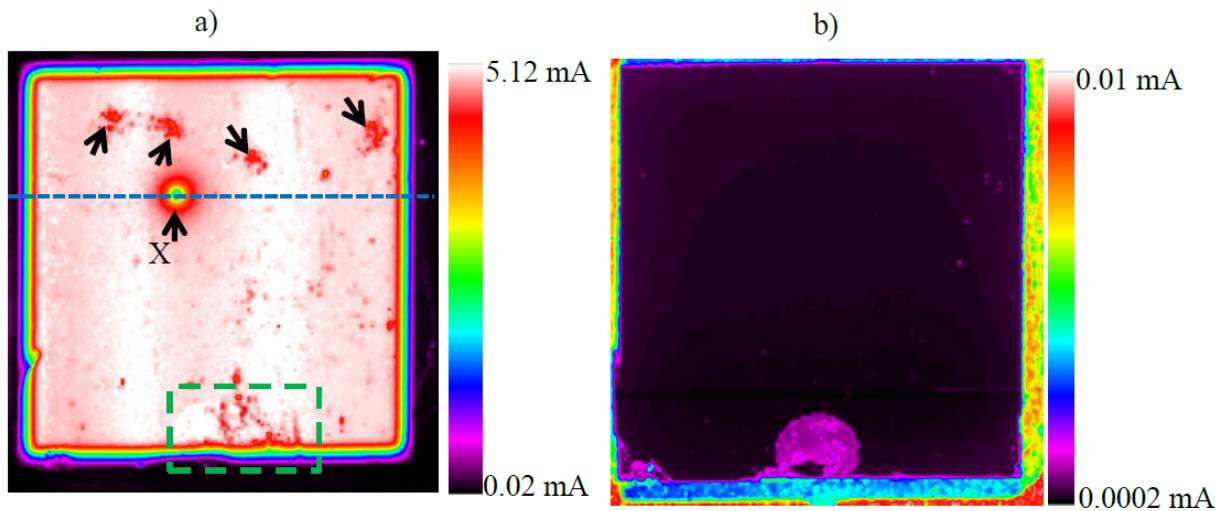


Figure 5.1: a)  $I_{sc}$  map, b) Reflection map of a BC-BJ silicon solar cell.

The feature marked X is more severe and could be acting as a shunt path that leads current away from the intended load. This could possibly be a precipitate or an inclusion introduced during the fabrication process.

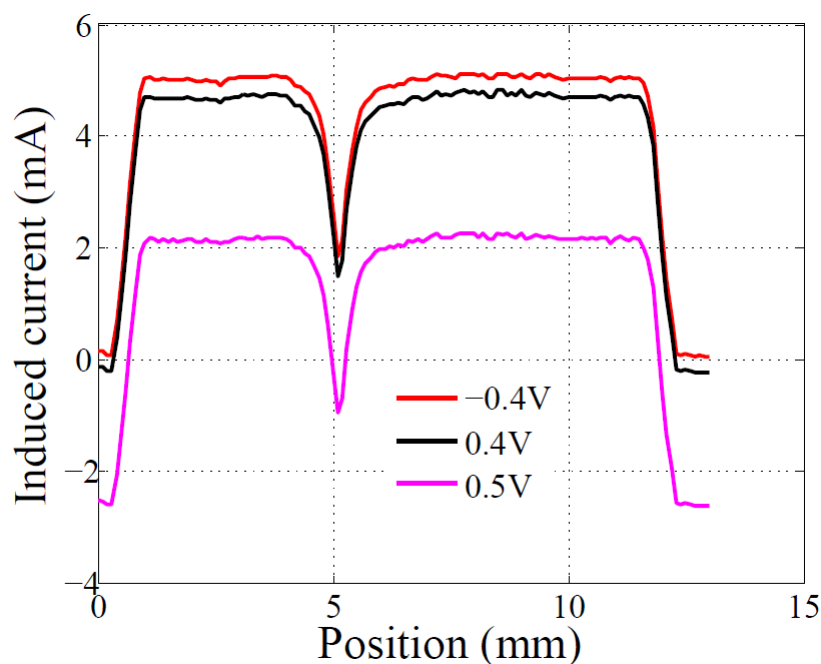


Figure 5.2: Line scan through a defect region at different biasing voltages.

Generally, shunts are mainly due to manufacturing defects rather than poor cell design and they provide an alternative current path for the photo-generated current thereby decreasing the cell efficiency by increasing the leakage current that lowers the maximum power output and the  $V_{oc}$  [136, 137]. The effect of shunting is particularly severe at low light levels since at such levels, less current is generated and so any loss will be detrimental. A line scan along the dotted line (Figure 5.1) showing the extent of current reduction due to this defect at different biasing voltages is given in Figure 5.2. The reduction in the measured induced current at the defect region at different biasing voltages is constant, meaning that its effect on photo-current generation is independent of the biasing voltage. The alternating regions of high and low photo-current generation observed in Figure 5.1 are due to electrical shading over the base fingers. Because the rear surface of the BC-BJ solar cell is not completely covered by a collecting emitter as illustrated in Figure 5.3 [58], recombination in regions not covered by the emitter reduces the  $I_{sc}$ , an effect referred to as electrical shading.

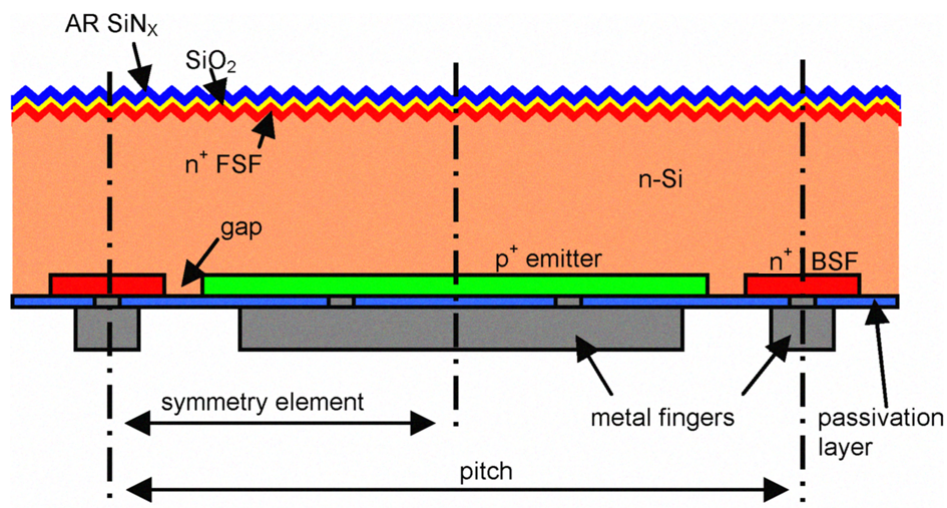


Figure 5.3: Schematic illustration of the two dimensional symmetry element of a BC-BJ silicon solar cell.

The photo-generated minority carriers in regions above the heavily doped back surface field ( $n^+$  BSF) have to travel laterally to the collecting emitter ( $p^+$  emitter). For industrial back junction solar cells, the width of the BSF is several times the cell thickness [11]. Since the lateral distance which the minority carriers have to diffuse in order to be collected by the p-n junction is much larger compared to the cell thickness, minority carrier collection in the region above  $n^+$  BSF is severely reduced resulting in a significant reduction in  $I_{sc}$  and a considerable loss in the device efficiency [137, 11]. In addition, enhanced recombination over the non collecting base region (undiffused gap and the BSF regions) which have high saturation current densities leads to reduction in  $I_{sc}$  over the base fingers [138].

## 5.2.2 I-V measurements and parameter extraction

I-V curve measurement is an essential characterisation technique for evaluating the behaviour and performance of solar cells and modules. By varying the applied voltage and measuring the corresponding current, I-V characteristics can be obtained from which performance indicators can be extracted. Current and voltage measurements of a Back contact Back junction silicon solar cell were obtained in the dark and under illumination conditions and a curve fitting algorithm described in Chapter 4 applied to extract device and performance parameters. The results are presented and discussed in this section.

### 5.2.2.1 Dark I-V measurements

The dark I-V characteristic curve obtained using a Keithley source measure unit (SMU) instrument is shown in Figure 5.4.

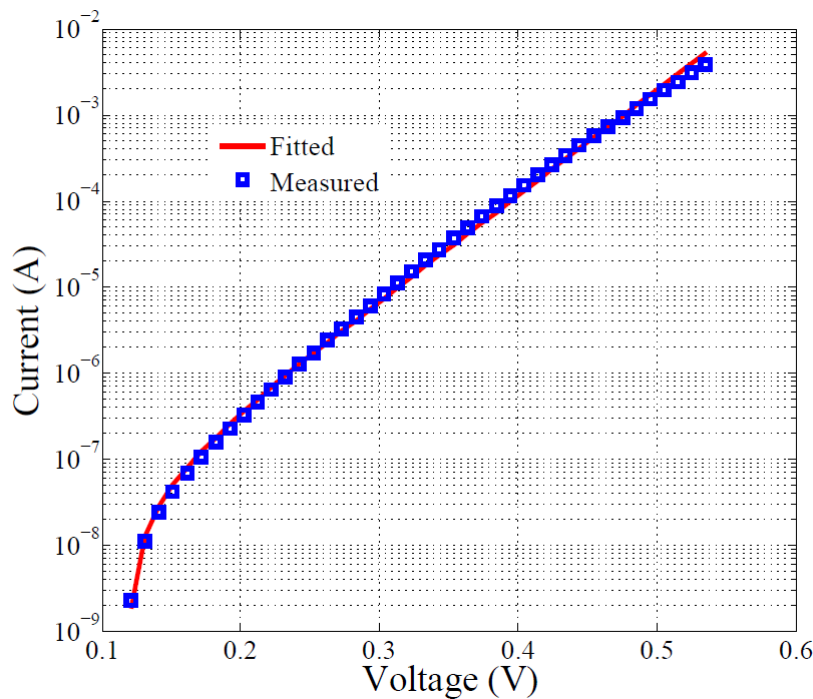


Figure 5.4: Dark I-V curve for a BC-BJ silicon concentrator solar cell.

The extracted device parameters are shown in Table 5.1.

Table 5.1: Extracted dark I-V parameters for a Back contact Back junction silicon concentrator solar cell.

Parameter	$n$	$I_o(A)$	$R_{sh}(\Omega)$	$R_s(\Omega)$
Value	1.36	$1.38 \times 10^{-9}$	$3.06 \times 10^6$	$1.33 \times 10^{-1}$

The dark I-V curve shows one linear region, indicating that the single diode model may be sufficient to describe the obtained I-V characteristic. The solar cell is characterised

by an ideality factor of  $\sim 1.4$  and a saturation current of  $\sim 1.4 \times 10^{-9} A$  which could possibly mean that the current generation in the device is dominated by recombination in the space charge region. Generally, ideality factors and saturation currents depend on the quality of the junction, with ideality factors greater than 1 an indication of low quality junction and normally considered as a signature of recombination losses [139]. In addition, the saturation current is affected by the diffusion length and carrier mobility as expressed in Equation 2.19. The device has a high shunt resistance that minimises leakage currents across the p-n junction as well as low series resistance. Such parameters are ideal for high performance concentrating devices to minimise resistive losses especially at high current densities. The series resistance reduces the fill factor of the solar cell according to the approximation proposed by Green [26]:

$$FF = FF_o \left( 1 - R_s \frac{I_{sc}}{V_{oc}} \right) \quad (5.1)$$

where  $FF_o$  is the ideal fill factor in the absence of parasitic resistances.

### 5.2.2.2 Full cell illuminated I-V measurements

Full cell illumination I-V measurements were carried out at solar noon on a clear sky day. The recorded plane of array irradiance as measured by the pyranometer mounted on the two axis tracker was  $940 Wm^{-2}$ .

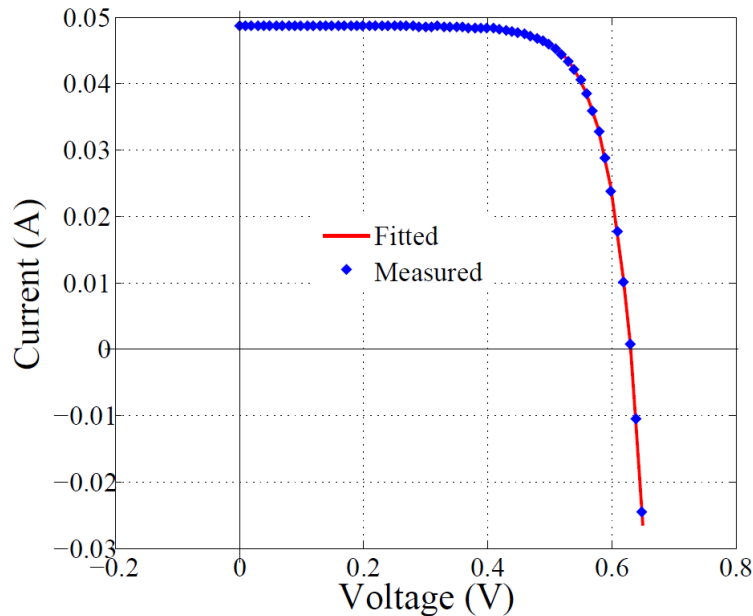


Figure 5.5: Full cell illumination I-V curve of a BC-BJ silicon solar cell.

Figure 5.5 shows the measured and fitted I-V curve, with an  $R^2$  value of 0.99998. The extracted parameters are given in Table 5.2.

Table 5.2: Extracted full cell illumination parameters for a Back contact Back junction silicon solar cell.

Parameter	$n$	$I_o(A)$	$R_{sh}(\Omega)$	$R_s(\Omega)$	$I_{sc}(A)$	$V_{oc}(V)$	$FF$
Extracted value	1.723	$3.55 \times 10^{-8}$	$1.21 \times 10^6$	$4.38 \times 10^{-2}$	0.0487	0.631	0.751

The extracted parameters show very high shunt resistance and low series resistance that are ideal for high performance concentrating solar cell devices. The difference in  $R_s$  obtained from dark and illuminated solar cell measurements can be attributed to the difference in current flow patterns in the cell in the dark and under illumination conditions. In the dark, current flows into the cell as opposed to current flow out of the cell under illumination conditions, which results in different electron flow patterns under the two conditions [140]. The device has an ideality factor less than 2 but higher than the dark ideality factor as well as a higher recombination current under illumination compared to the dark conditions. The deviation between dark and illumination conditions can be attributed to a departure from the superposition principle resulting from the non-linearity of the semiconductor device equations with respect to carrier concentration [141]. The superposition principle forms the theoretical basis for comparison of dark and illuminated I-V characteristics. This departure is due to an additional current dependent bulk recombination caused by the higher density of charge carriers under illumination and under current extraction than in the dark. It depends on the illumination intensity but is negligible at low intensities. According to Breitenstein [142], the deeper physical reason for the departure is due to the fact that under illumination and under current flow, the electron quasi Fermi level in the bulk lies above that at the same p-n junction voltage in the dark, which generally, results into higher bulk recombination under illumination and low forward bias than in the dark.

### 5.2.2.3 Parameter maps

The area around the defect feature marked X observed in Figure 5.1 was scanned using a 660 nm wavelength laser while dynamically biasing the solar cell from reverse bias to a voltage slightly greater than its  $V_{oc}$  to obtain point-by-point I-V measurements. The  $I_{sc}$  map of the scanned area is shown in Figure 5.6 while representative I-V curves extracted at point Q, an area of high photo-response, and point P, a defect region are shown in Figure 5.7. The curve fitting algorithm earlier described was applied to the point-by-point I-V measurements to extract device and performance parameters. The extracted device parameters are shown in Figure 5.8 where a decrease in the shunt resistance and an increase in the series and reverse saturation current over the defect are observed.



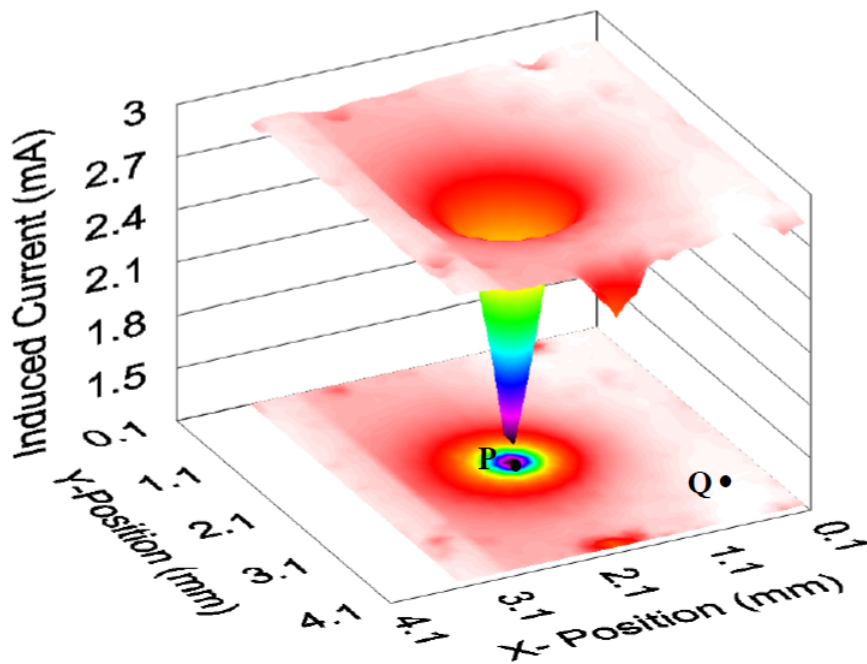
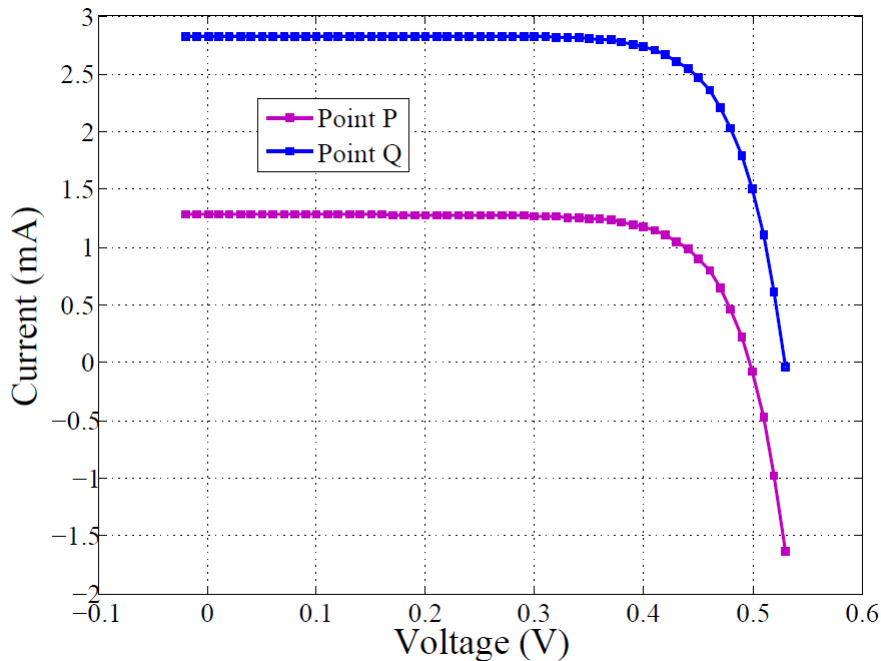
Figure 5.6:  $I_{sc}$  map of the area around the defect

Figure 5.7: Spot illuminated I-V curves extracted from LBIC measurements

A slight decrease in the ideality factor is also visible over the defect area. Localised increase in series resistance has a detrimental effect on the fill factor and the short circuit current of the solar cell. The observed decrease in the shunt resistance over the defect leads to an increase in the leakage current that drains part of the locally induced current, resulting in a decrease in the maximum power output and the open

circuit voltage while an increase in the saturation current means an increase in the dark current which results in a decrease in the short circuit current and the open circuit voltage as shown in the performance parameter maps in Figure 5.9.

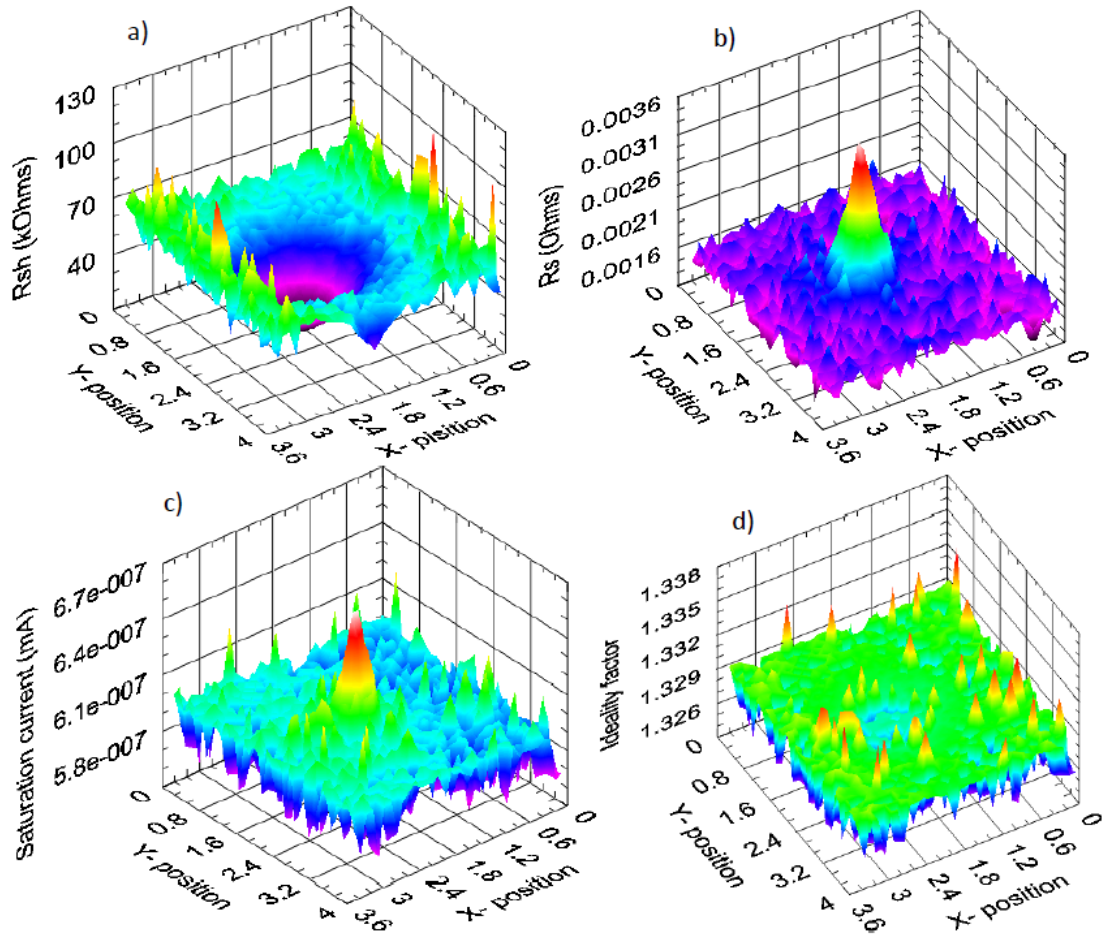


Figure 5.8: Extracted device parameter maps for a Back contact Back junction solar cell: a) Shunt resistance, b) Series resistance, c) Saturation current, d) Ideality factor.

Severe shunting can result in hot spot formation that is detrimental to the performance of the device.

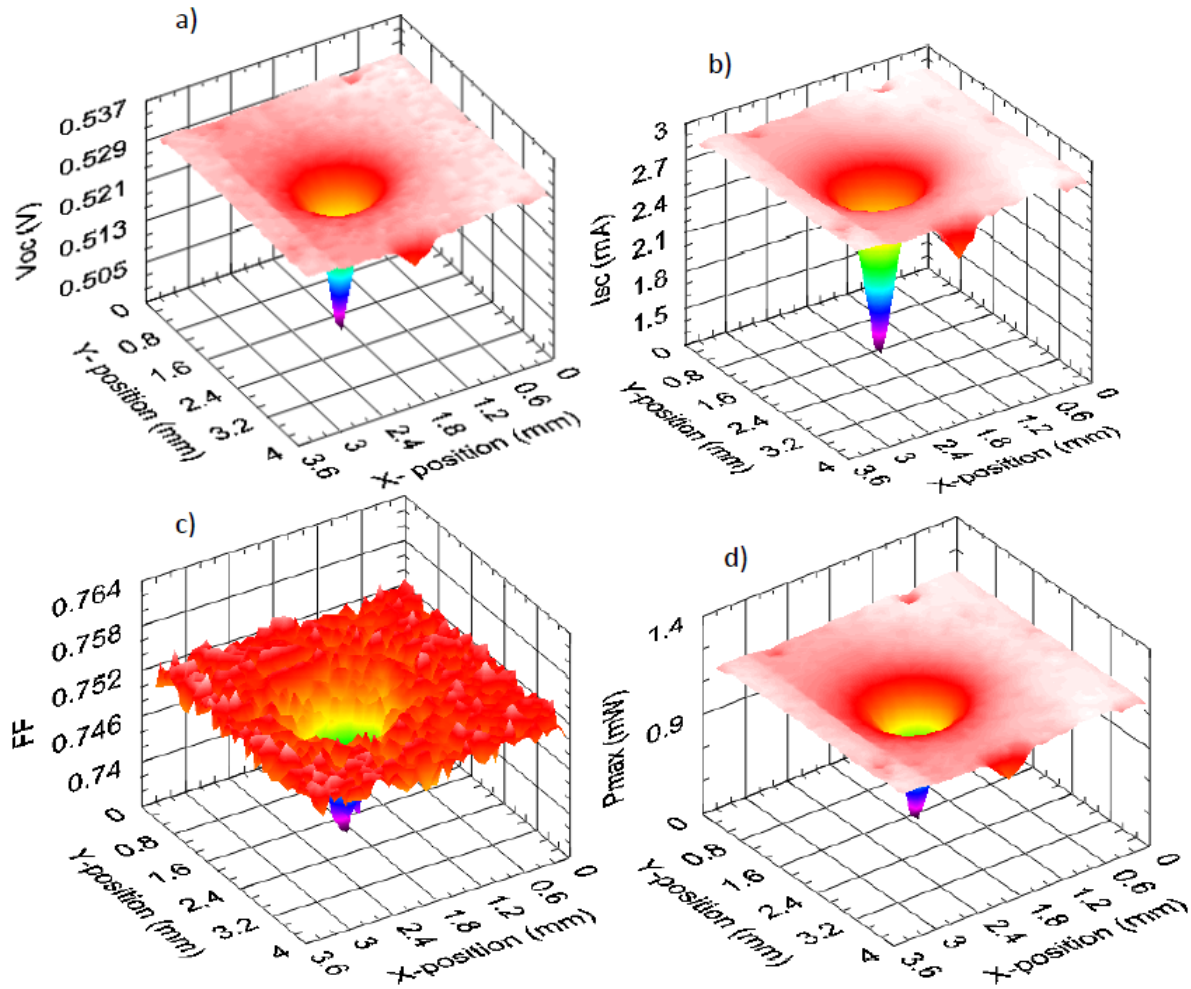


Figure 5.9: Extracted performance parameter maps for a Back contact Back junction solar cell: a) Open circuit voltage, b) Short circuit current, c) Fill factor, d) Maximum power.

### 5.3 InGaP/InGaAs/Ge triple junction solar cell

Currently, the state of the art high efficiency III-V solar cells utilise the lattice matched concentrating triple junction (CTJ) solar cell structure that consists of monolithically grown  $\text{Ga}_{0.5}\text{In}_{0.5}\text{P}$  ( $1.86\text{ eV}$ ) as the top subcell,  $\text{Ga}_{0.99}\text{In}_{0.01}\text{As}$  ( $1.36\text{ eV}$ ) as the middle subcell and Ge ( $0.67\text{ eV}$ ) as the bottom subcell on a Ge substrate [79, 143]. Though this solar cell structure has attained conversion efficiencies of more than 40% under concentration, the band gap combination of the subcells is not optimal for maximum conversion efficiency of the solar spectrum as this structure suffers from current mismatch due to the higher current produced by the Ge subcell as a result of the large band gap difference between  $\text{Ga}_{0.99}\text{In}_{0.01}\text{As}$  middle subcell and the Ge bottom subcell [144, 15, 67]. The low band gap Ge subcell produces a current density that is far in excess of what is produced by the epitaxial InGaP and InGaAs subcells grown above it, with the GaInAs middle

subcell utilising the smallest part of the spectrum and hence producing the lowest current, making it the current limiting junction [15]. In order to achieve current matching conditions under a specific spectrum, the absorbing layer of the InGaP upper subcell can be thinned so that more photons are transmitted to the GaInAs middle subcell. Alternatively, the band gaps for the top two subcells can be decreased by increasing the indium content in the top and middle subcells. This, however, increases the lattice constant of the two subcells resulting in a lattice mismatch between the top two subcells and the Ge subcell. The optimal band gap and optimal subcell thinning generally depends on the spectral content of the incident beam which determines the photo-current generated by each subcell [71].

Characterisation of multijunction solar cells presents more challenges compared to single junction solar cells due to the series connection of multiple subcells [145]. In monolithically integrated solar cells, the subcells are epitaxially grown and internally connected in series through tunnel junctions to form a two terminal device. Because each subcell is optimised to absorb a given range of wavelengths of the solar spectrum, any changes in the incident spectrum may result in current mismatch which will affect the performance of the device. In this section, we present results of photo-response mapping and parameter extraction for InGaP/InGaAs/Ge CTJ solar cell, an *n* on *p* polarity on a germanium substrate manufactured by the Emcore Corporation, with an active surface area of  $10 \times 10 \text{ mm}^2$ . Figure 5.10 [146] shows the 39% conversion efficiency receiver assembly [147] of the CTJ used in this study.

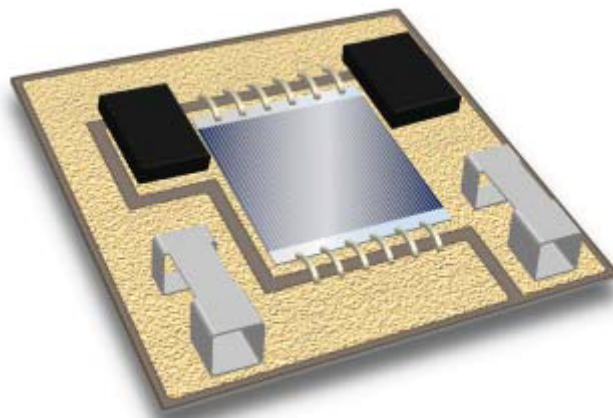


Figure 5.10: CTJ Receiver Assembly.

This CTJ solar cell is optimised for terrestrial applications under concentrated incident illumination and high current densities and incorporates a proprietary antireflective coating that provides low reflectance over a wavelength range of  $0.3$  to  $1.8 \mu\text{m}$  [147]. The band gaps of the top, middle and bottom subcells are  $1.86$ ,  $1.36$  and  $0.67 \text{ eV}$ , respectively. The spectral response of this CTJ is given in Figure 5.11 [148] and shows the spectral response ranges of the three subcells i.e. the top junction spectral response

range is  $\sim 300 - 700 \text{ nm}$ , the middle junction is  $\sim 550 - 900 \text{ nm}$ , while the bottom junction is  $\sim 800 - 1900 \text{ nm}$ . The results of the spectral response give a clear idea of what wavelengths can be used to properly perform an LBIC scan.

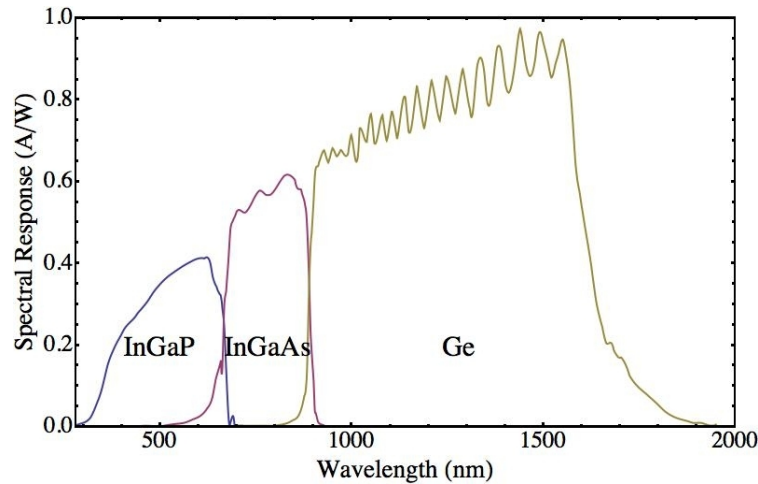


Figure 5.11: Spectral response of individual subcells of InGaP/InGaAs/Ge CTJ.

### 5.3.1 Photo-response mapping

The InGaP/InGaAs/Ge CTJ solar cell was illuminated with a  $660 \text{ nm}$  wavelength laser with a spot size of  $\sim 150 \mu\text{m}$  and intensity of  $12 \text{ mW}$ , which corresponds to an injection level of  $\sim 4 \times 10^{16}$  photons per second. This wavelength lies within the spectral response range of the top two subcells (see Figure 5.11) and so would activate the InGaP and InGaAs subcells. The Ge bottom subcell will not primarily be activated by the  $660 \text{ nm}$  laser beam as this wavelength lies outside the spectral response range of the Ge subcell and will primarily operate under dark conditions, producing no current at all.

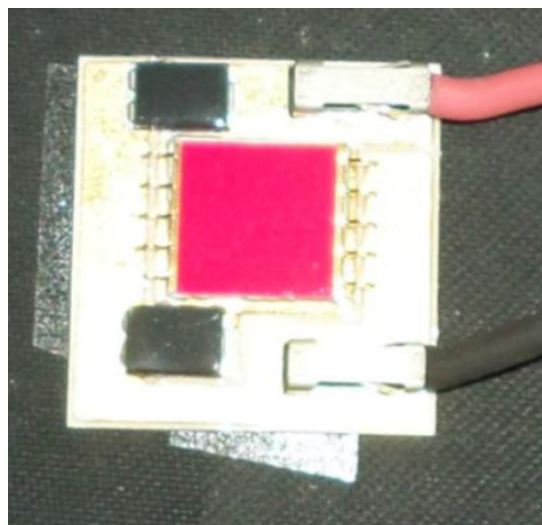


Figure 5.12: CTJ solar cell under a forward bias of  $3 \text{ V}$  showing electroluminescence.



Due to the series connection of the subcells, no current output will be expected from the CTJ solar cell device since the output current is determined by the subcell producing the lowest current. However, when an InGaP/InGaAs/Ge CTJ solar cell is forward biased, it undergoes electroluminescence, with the top InGaP subcell emitting red light that can easily be seen with a naked eye as shown in Figure 5.12, with a peak at  $680\text{ nm}$ . The emission from the middle junction lies in the infrared region, with a spectral peak at  $880\text{ nm}$  while the electroluminescence spectrum from the Ge subcell peaks at  $1700\text{ nm}$  and is very weak since Ge is an indirect bandgap material. The electroluminescence is due to the radiative recombination of electrons injected from the emitter into the base when the solar cell is forward biased [149]. Radiative recombination tends to be the dominant recombination process for direct semiconductor materials with pure and perfect crystal orientation [150]. In multijunction solar cells, the radiatively emitted light from an overlying high bandgap junction may be absorbed by a lower bandgap junction, a process called luminescent coupling. The emitted secondary luminescent photons which could be absorbed by the lower bandgap junctions will contribute to photocurrent generation of those junctions [151, 152]. For high quality III-V junctions whose recombination is largely radiative, this effect can have a significant effect on the short circuit photocurrent densities of the junctions [153].

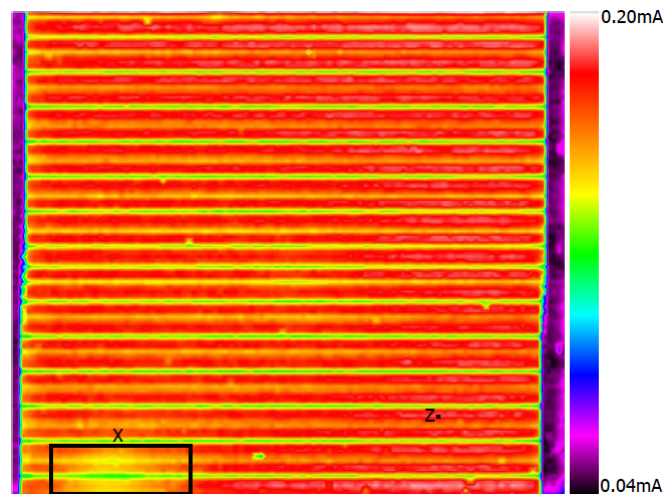


Figure 5.13:  $I_{sc}$  map for the InGaP/InGaAs/Ge CTJ using a  $660\text{ nm}$  wavelength laser.

For the InGaP/InGaAs/Ge CTJ solar cell, the emitted luminescent photons from the InGaP top subcell may be absorbed by the middle subcell leading to an increase in the InGaAs subcell current generation while the photons emitted from the middle subcell may also be absorbed by the Ge subcell, thus enhancing photocurrent generation in the bottom subcell. Radiative coupling between the subcells may therefore play an important role in overcoming current mismatch and thus improving the performance of the CTJ solar cell devices especially when they are operated under spectral mismatch conditions [154, 155]. By illuminating the CTJ solar cell with the  $660\text{ nm}$  wavelength laser, the

emitted secondary photons from the InGaAs subcell could activate the bottom Ge subcell and prevent it from being under “dark conditions”. This could explain the current response observed in Figure 5.13 when the InGaP/InGaAs/Ge CTJ solar cell is illuminated with a 660 nm wavelength laser. The  $I_{sc}$  map (Figure 5.13) shows the expected current reduction due to shading from the contact fingers and busbar metallisation. The fingers and busbar metallisation act as optical blockages that reflect the incident light. The current reduction contour adjacent to the metallisation (fingers and busbars) is due to the change in effective illuminated area as the light spot moves over a shading finger or busbar. Also observed is an area marked X that shows reduced photo-response right under a finger metallisation. This could be a shunt created during solar cell processing. A possible current loss mechanism could be local shunt paths that are formed across the p-n junction when dopant impurity atoms diffuse across the junction below the finger metallisation. Shunts in solar cells are defect related and act as low resistance connections that form alternative paths for the photo-generated current. They reduce the fill factor and output power and in severe cases, they result in reduction of  $V_{oc}$ . Severe shunts can result into hot spots which are detrimental to the performance of solar cells as they can cause serious reliability problems in finished solar cell devices and modules.

### 5.3.2 I-V measurements and parameter extraction

For series connected multijunction solar cells, the shape of the I-V curve is dominated by the I-V characteristic of the subcell producing the least current if the subcells are not current matched. I-V measurements for the InGaP/InGaAs/Ge CTJ solar cell were obtained in the dark and under full cell solar illumination conditions using a Keithley source measure unit (SMU). The curve fitting algorithm discussed previously in Chapter 4 was then used to extract the I-V parameters by fitting the experimental data to the modelled data. The results are presented and discussed in this section.

#### 5.3.2.1 Dark I-V measurements

Figure 5.14 shows the measured and fitted dark I-V characteristics for the CTJ solar cell in which we observe good agreement between the measured and fitted I-V curves, except at very low bias voltages where reverse bias voltage breakdown is observed to occur.

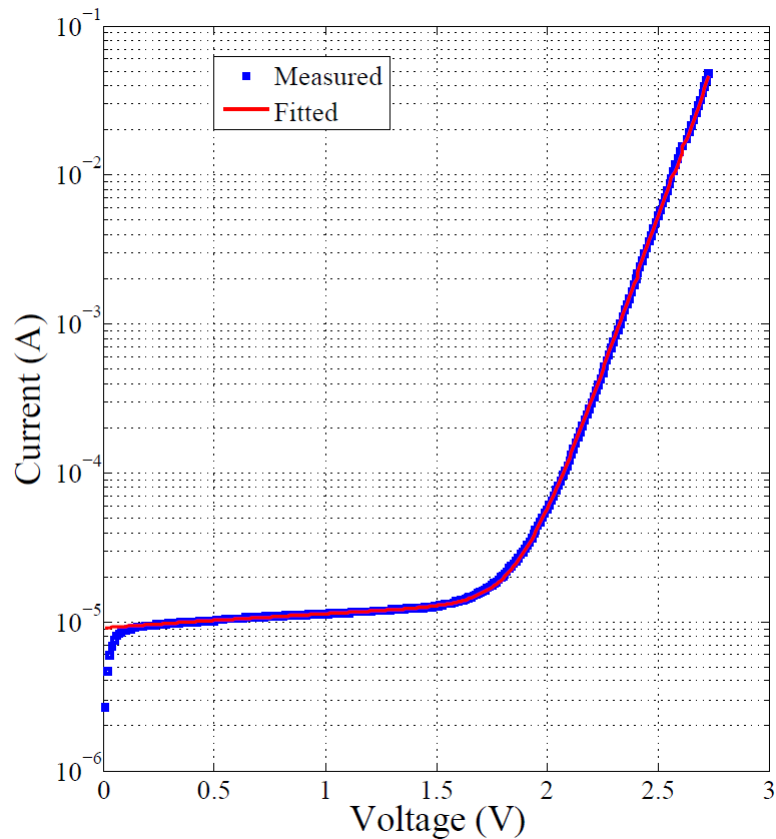


Figure 5.14: Dark I-V characteristic of a CTJ solar cell.

The breakdown could be from the Ge subcell due to its low band gap that makes it susceptible to reverse bias breakdown. The device parameters extracted using the two diode model are also shown in Table 5.3.

Table 5.3: Extracted dark I-V parameters for a triple junction solar cell.

Parameter	$n_1$	$I_{01}$ (A)	$n_2$	$I_{02}$ (A)	$R_{sh}$ ( $\Omega$ )	$R_s$ ( $\Omega$ )
Extracted value	3.21	$3.77 \times 10^{-17}$	4.13	$2.62 \times 10^{-13}$	$4.53 \times 10^5$	$1.79 \times 10^{-2}$

The graph shows that the total current is dominated by different conduction mechanisms, each dominating in a specific voltage range. At biasing voltages below  $\sim 0.1$  V, the effect of reverse bias voltage breakdown is dominant while at voltage range between  $0.1$  V and  $\sim 1.7$  V, the shunt resistance and the 2<sup>nd</sup> diode current, with a higher saturation current, dominates. The 2<sup>nd</sup> diode (recombination current diode) has on average an ideality factor of  $\sim 1.4$ , an indication that recombination mechanism is dominating the low to medium bias region. At voltages higher than  $\sim 1.7$  V, the diffusion current (1<sup>st</sup> diode), characterised by an average diode ideality factor of  $\sim 1$  is dominant. The device has a very low series resistance whose effect on the dark I-V curve at high biasing voltages is not significant.



### 5.3.2.2 Full cell solar illumination

Current and voltage measurements were taken on a clear sky day, with the measurement system on a two axis sun tracker. The plane-of-array solar irradiance as recorded by the pyranometer on the tracker was  $940 \text{ W m}^{-2}$ . A curve fitting algorithm based on the single diode model was applied to the measured I-V values to extract device and performance parameters. In Figure 5.15, the measured and fitted I-V curves are plotted showing good agreement with an  $R^2$  value of 0.9996, indicating that the single diode model may be sufficient to model the I-V characteristics of the CTJ solar cell. The single diode model has previously been applied to multijunction solar cells to predict their performance and is often used by CPV system designers [156]. The I-V characteristics show that the CTJ solar cell device is characterised by high voltage and low current values that result in lower resistive power losses compared to single junction devices.

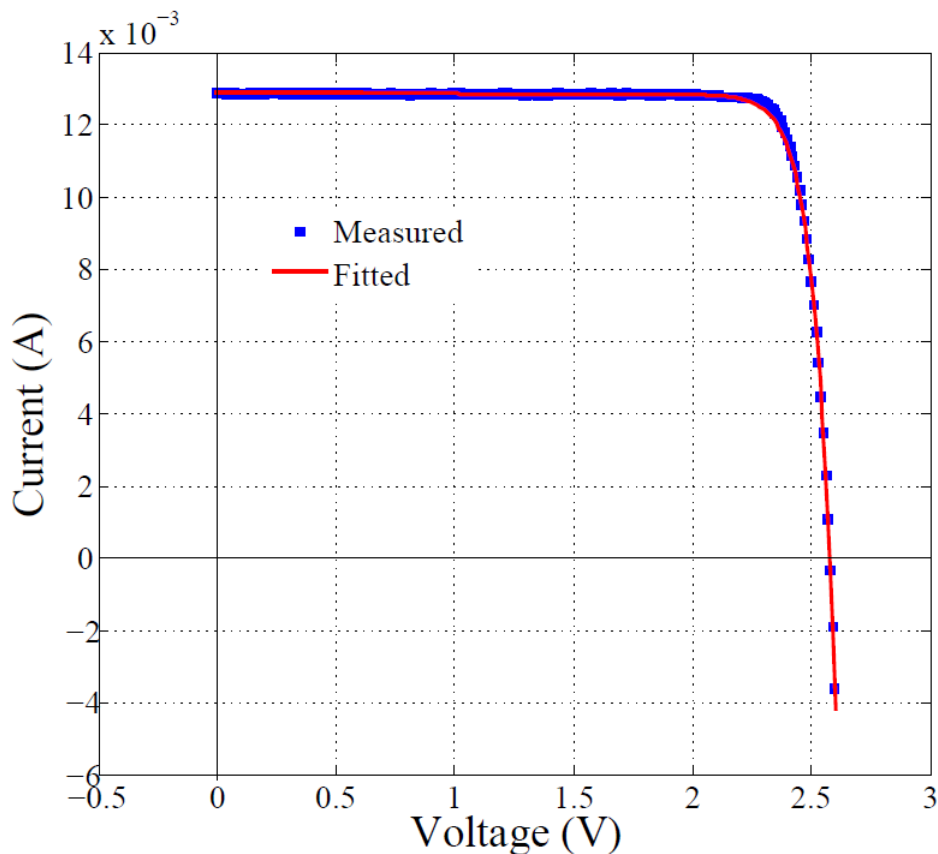


Figure 5.15: Measured and fitted full cell illumination I-V characteristic of a CTJ solar cell.

Series-connected multijunction solar cells are inherently lower current devices than single junction cells since the current output from the device is limited by the current from the lowest performing subcell, and therefore have a great advantage in minimising resistive losses especially at high concentrations. The extracted parameters are shown in Table 5.4 in which we observe that the CTJ solar cell is characterised by high shunt re-

sistance, low saturation current and ideality factor  $\sim 3$ , consistent with reported values [157].

Table 5.4: Extracted full cell illumination parameters for the triple junction concentrator solar cell.

Parameter	$n$	$I_o (A)$	$R_{sh} (\Omega)$	$R_s (\Omega)$	$I_{sc} (A)$	$V_{oc} (V)$	$FF$
Extracted Value	3.016	$5.97 \times 10^{-17}$	$5.23 \times 10^4$	0.727	0.0129	2.577	0.861

The extracted ideality factor represents the effective mean ideality factor for the three subcells that make up the lumped diode, giving an average of 1.0 per subcell. This could possibly indicate that diffusion is probably the dominant current mechanism in each subcell. In reality, variation in the ideality factor of each subcell is expected due to the differences in the junction profile as each subcell differs in structure and composition. The device also has a low series resistance which is ideal for concentrating photovoltaic devices as it minimises ohmic power losses and its effect on efficiency and fill factor. The series resistance depends on the density of front contact grid fingers [158], with higher grid density for solar cells designed for high concentration but has to be optimised to minimise device shadowing that reduces the current. The high fill factor exhibited by the device reflects the high quality of the CTJ solar cell. Most high quality III-V multi-junction concentrator solar cells have fill factor ranging from the mid to high 80% range [75]. Fill factor is often used to establish whether a multijunction solar cell is operating under current matched or mismatched conditions during spectrometric measurements. Seifer *et al.* [159] working on a dual junction device for spectrometric characterisation observed that the fill factor of the device was lowest at the current matching condition but increased with increase in current mismatch.

### 5.3.2.3 Spot illuminated I-V curve

A representative spot illuminated I-V curve was extracted from LBIC measurements at point marked Z in Figure 5.13 and fitted using an interval division algorithm based on the single diode model. The extracted and fitted I-V curves are shown in Figure 5.16, with an  $R^2$  value of 0.994. The extracted I-V characteristic shows reverse voltage breakdown in the power quadrant which could be attributed to the Ge bottom subcell not being fully activated by the 660 nm wavelength laser. Due to its low band gap, the Ge subcell is more susceptible to reverse bias breakdown compared to the InGaP and the InGaAs subcells. This voltage breakdown was, however, not observed in the full cell solar illumination I-V curve since all the subcells were fully activated by the solar spectrum that covers the spectral reponse range of the three subcells. The extracted parameters are also shown in Table 5.5. The extracted parameters are typical of single

subcell parameters, apart from the  $V_{oc}$  that is the sum of the individual subcell  $V_{oc}$ 's due to the series connection of the subcells.

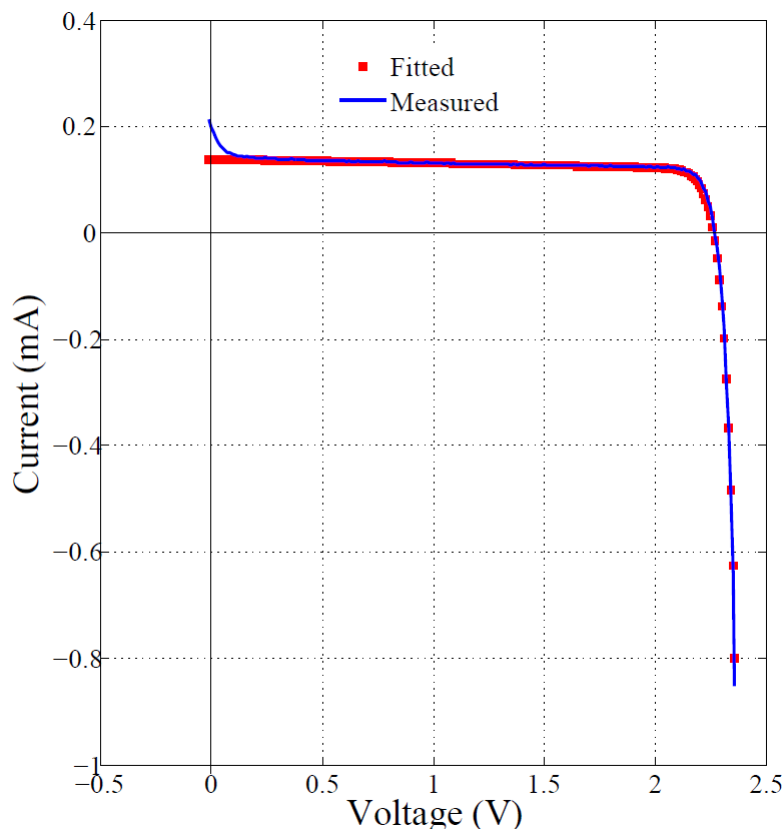


Figure 5.16: Point illuminated I-V curve extracted from LBIC measurements.

Table 5.5: Extracted parameters for the point illuminated CTJ solar cell.

Parameter	$n$	$I_o$ (A)	$R_{sh}$ ( $\Omega$ )	$R_s$ ( $\Omega$ )	$I_{sc}$ (mA)	$V_{oc}$ (V)	$FF$
Extracted value	1.83	$2.0 \times 10^{-25}$	$1.30 \times 10^5$	0.357	0.138	2.264	0.801

The extracted ideality factor is indicative of current response from a single subcell that is acting as the current limiting junction for the CTJ solar cell. Ideality factors of the individual subcells are expected to be close to 1 [157] though they may deviate from 1 due to non-ideal recombination current in the subcells.

### 5.3.3 S-LBIC measurements

S-LBIC mapping technique has an advantage over LBIC, especially when applied to multijunction solar cells as the former has a full solar spectrum compared to the latter that uses monochromatic light as a beam probe. As a result, the subcells in a multijunction series connected stack may not all be activated without any biasing (voltage or light) if the wavelength of the LBIC beam probe does not lie within the spectral response

ranges of all the subcells in the stack. This may result in some junctions operating in the dark, thus affecting the photo-response of the device. The intensity of the beam and the spectral content, however, do not change with time if a laser with a stable output is used. In S-LBIC, however, the intensity and or spectral content of the solar beam may change with time due to changing atmospheric conditions which may affect measurements, especially when scanning a relatively large area, which may result in misinterpretation of results. S-LBIC measurements should therefore be taken on a clear sky day, around solar noon on a two axis sun tracker for a small area scan that may not take a long time to complete. With the measurement system on a two axis sun tracker, an area of  $3 \times 3 \text{ mm}^2$  was selected for scanning using a scanning step size of  $0.1 \text{ mm}$  and a spot size of  $\sim 200 \mu\text{m}$ . It took  $\sim 8$  minutes to complete the scan. An interval division algorithm based on the single diode model was then applied to extract point-by-point I-V parameters which are shown in Figures 5.17 and 5.18.

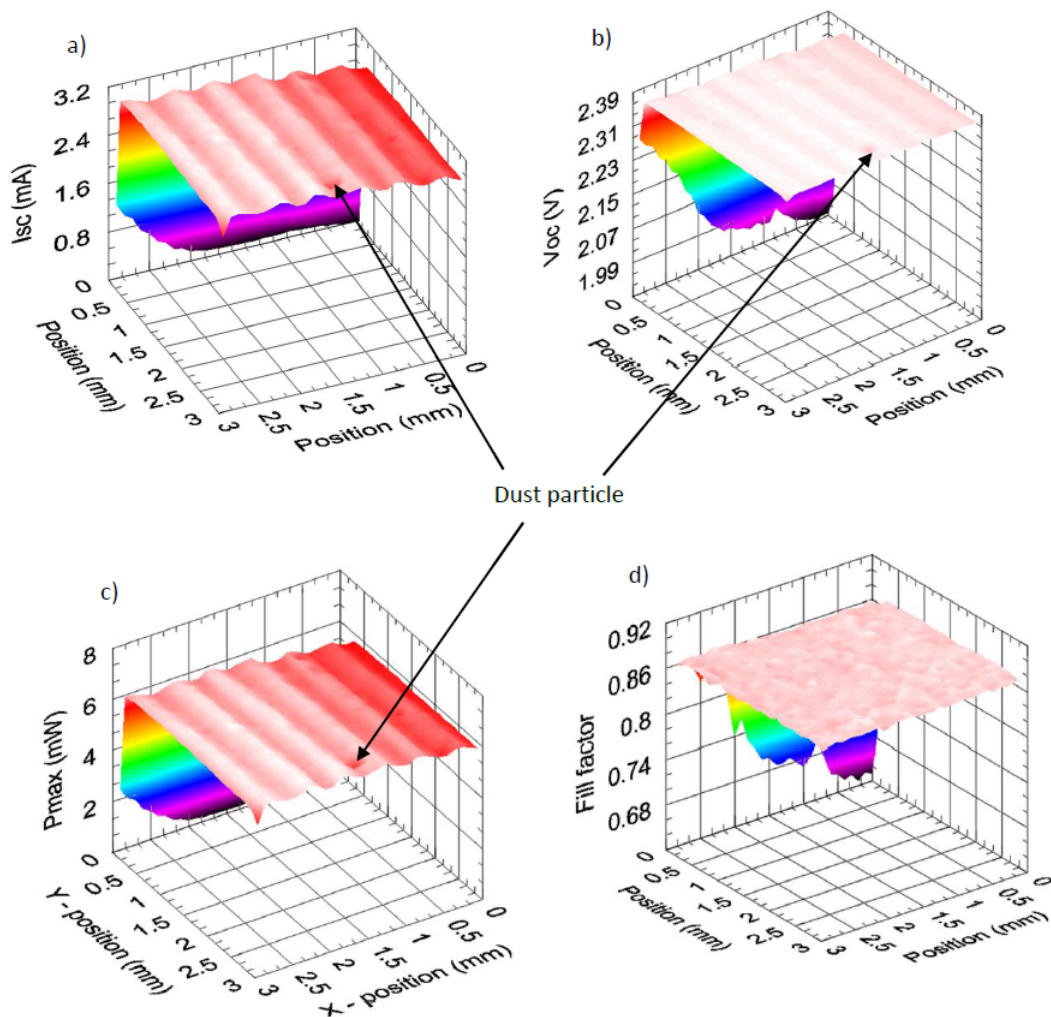


Figure 5.17: CTJ solar cell performance parameter maps: a) Short circuit current, b) Open circuit voltage, c) Maximum power, d) Fill factor.

The performance parameter maps in Figure 5.17 show a decrease in the extracted pa-

rameters due to shading from the fingers and the bus bar metallisation. The contours observed in the performance parameter maps are due to the change in the effective active area illuminated as the beam spot moves over a shading finger. Also observable is a spot with reduced photo-response due to a dust particle. Such dust particles as well as the fingers and bus bar metallisation act as optical blockages by reflecting most of the incident light, which results in reduction in the device photo-response. Shown in Figure 5.18 are device parameter maps in which an increase in the ideality factor, saturation current and series resistance over the busbar metallisation is observed while there is a decrease in the shunt resistance.

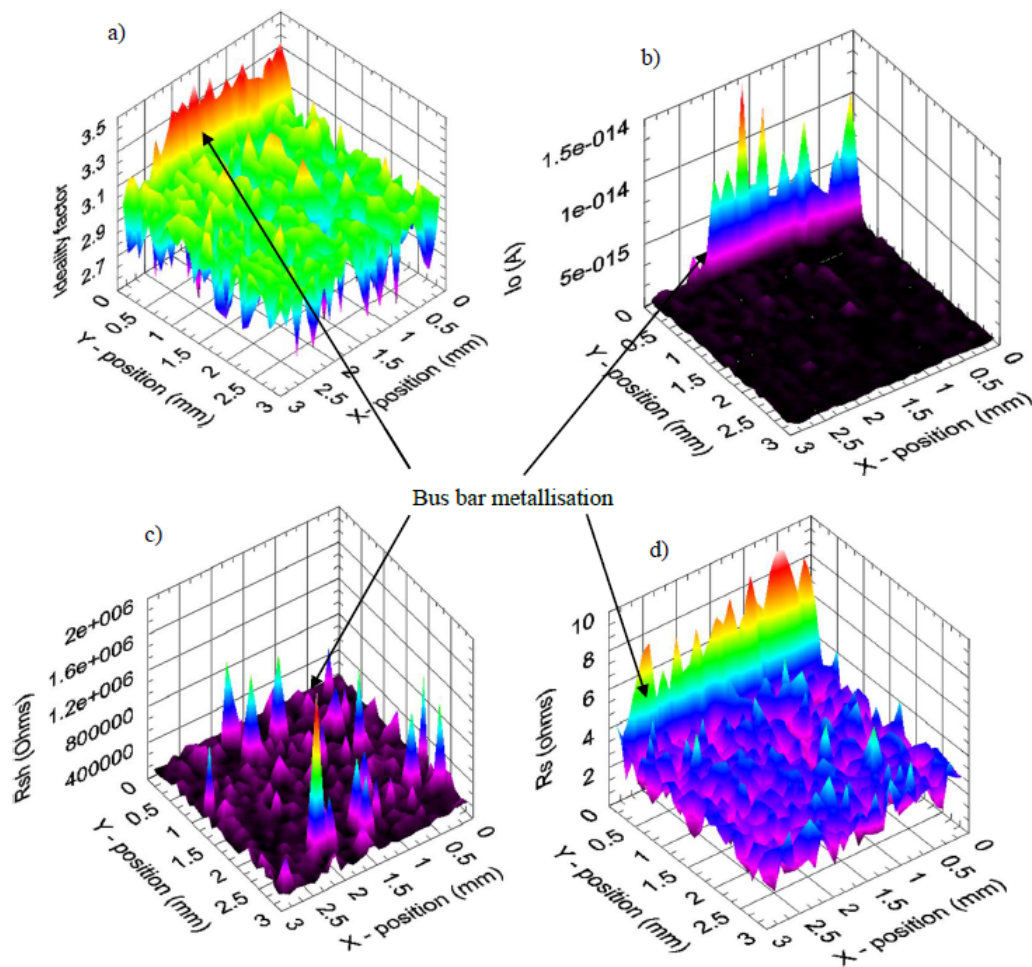


Figure 5.18: CTJ solar cell device parameter maps: a) Ideality factor, b) Saturation current, c) Shunt resistance, d) Series resistance.

The observation over the bus bar metallisation is an artefact attributed to the effect of shading on the spot illuminated I-V characteristics in this region. The device parameter maps did not show any distinct features including the effect of the dust particle observed in Figure 5.17 since it is a local optical blockage that reduces the photocurrent over a very small area.

## 5.4 Conclusion

In this Chapter, two concentrator solar cell devices, a Back contact Back junction (BC-BJ) silicon solar that is suitable for low to medium concentrator applications and an InGaP/InGaAs/Ge CTJ solar cell suitable for high concentration applications were characterised in terms of photo-response mapping and parameter extraction. The photo-response maps obtained from LBIC measurements, together with reflection measurements were used to identify localised current reducing features such as shunts and local optical blockages. It was noted that the BC-BJ silicon solar cell does not suffer from optical shading arising from the front finger metallisation since all the electrical contacts are located at the rear surface. However, it suffers from electrical shading due to recombination in regions that are not covered by a collecting emitter at the rear surface. The photo-response map obtained using a  $660\text{ nm}$  wavelength laser revealed the presence of a defect characterised by low shunt resistance and an increase in series and reverse saturation current as observed in the extracted device parameter maps over the defect region. A decrease in localised performance parameters over the defect was indicative of the detrimental effect of the defect over the performance of the device. Device and performance parameters extracted from dark and full cell solar illumination I-V characteristics for the two concentrator solar cell devices showed that the devices were characterised by high shunt and low series resistances, parameters that are ideal for concentrating solar cells that operate at high current densities. Deviations between dark and illuminated I-V parameters were observed and were attributed to departure from the superposition principle due to non-linearity of the semiconductor device equations with respect to carrier concentration. Using a  $660\text{ nm}$  wavelength laser as a beam probe while applying a voltage bias to the InGaP/InGaAs/Ge CTJ solar cell, the InGaP and InGaAs subcells were activated by the beam probe since it lies within the spectral response range of the two subcells while the Ge bottom subcell was activated through luminescent coupling, thus enabling LBIC measurements to be obtained. However, the spot illuminated I-V characteristic obtained with the  $660\text{ nm}$  wavelength laser showed reverse bias voltage breakdown in the power quadrant which was attributed to the Ge subcell not being fully activated. Voltage breakdown was not observed in the power quadrant under solar illumination. With the measurement system on a two axis sun tracker, S-LBIC measurements were carried out to obtain point-by-point solar beam I-V characteristics from which device and performance parameter maps for the CTJ solar cell were extracted. The parameters maps did not show any distinct performance reducing features, an indication of the high quality of the device.

# Chapter 6

## Intensity and Spectral change effects on solar cell I-V parameters

### 6.1 Introduction

Photovoltaic (PV) device characterisation involves extraction of performance and device parameters from I-V characteristics obtained under specific spectral conditions such as specified by the reference standard reporting conditions (SRC) to evaluate their performance. The standard reference spectra represent terrestrial solar spectral irradiance incident on a particular surface under one set of specified atmospheric conditions [160]. However, under outdoor conditions, the devices are exposed to varying conditions such as changing intensity, temperature and spectral content which affects the I-V characteristics and performance of the device. Changing illumination intensity and spectral content affects performance and device parameters of solar cells and has been studied by various researchers for various devices under full cell illumination [161, 162, 163, 164]. Mapping of spatial variation of device and performance parameters using characterisation techniques such as LBIC are based on spot illumination of the solar cell device to obtain localised point-by-point I-V characteristics. A need therefore exists to study the variation of the measured parameters of a spot illuminated cell. The localised I-V characteristics obtained are representative of the whole solar cell's response to spot illumination since measurements are made at the external contacts of the solar cell device. The evaluation of performance and device parameters at different intensities and spectral content of spot illuminated solar cells is therefore important in an effort to understand how the intensity and spectral content affect the results of LBIC. Such studies are useful in identifying various physical processes in solar cells and developing optimised designs that can result in higher photovoltaic conversion efficiencies. In this chapter, the effect of changes in intensity and spectral content on the device and performance parameters of a back contact back junction silicon solar cell and a III-V triple



junction concentrator cell under spot illumination is studied.

## 6.2 Effect of illumination intensity

Device and performance parameters of a spot illuminated Back contact Back junction (BC-BJ) silicon solar cell discussed in Sections 2.6.1.1 and 5.2.1 were extracted from I-V measurements obtained at different illumination levels while keeping the illumination spot position constant. A 445 nm wavelength laser was used as a beam probe with a spot size of  $\sim 1.2$  mm. The laser beam power output was varied from 0 to 45 mW, corresponding to an intensity variation from 0 to  $\sim 400$  kWm<sup>-2</sup>, to obtain I-V characteristics at different illumination levels. Figure 6.1 presents the illumination level dependent I-V characteristics of a BC-BJ Si solar cell which show that as the incident power changes, the corresponding I-V curve also changes.

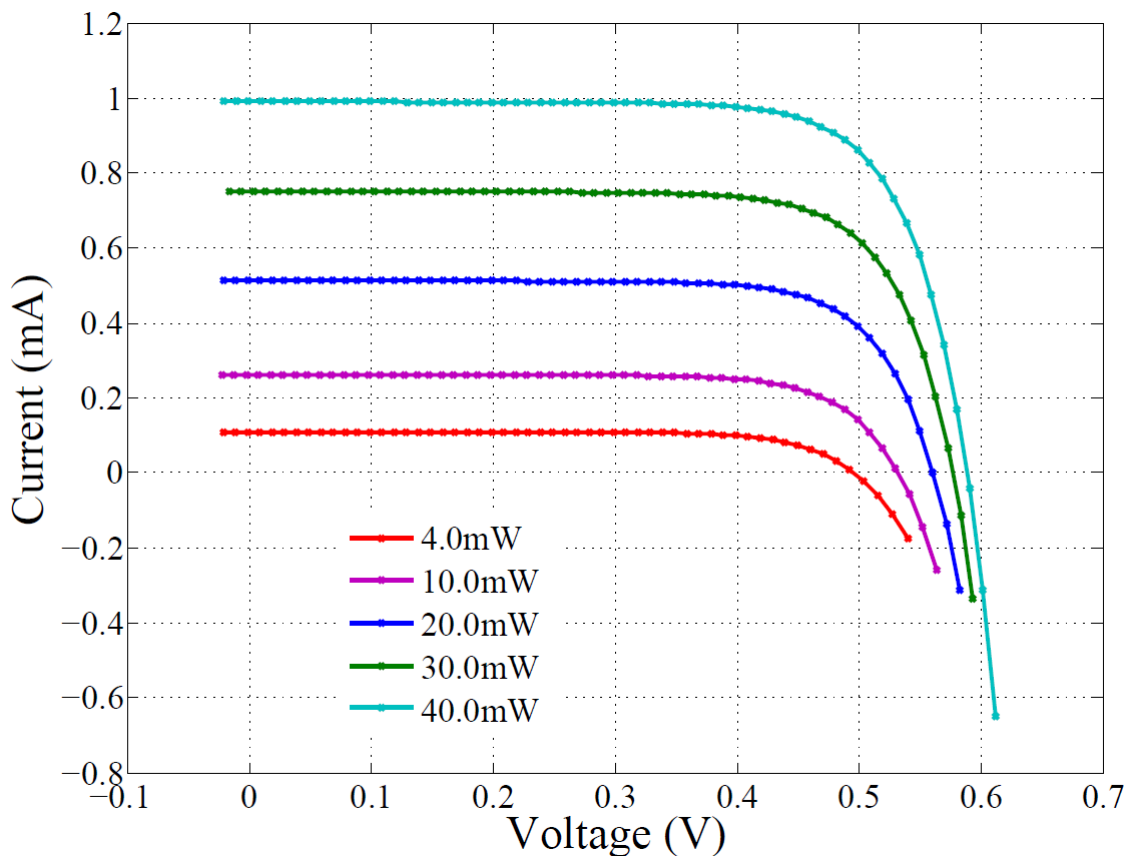


Figure 6.1: I-V characteristics of a Back contact Back junction Si solar cell at different laser power outputs.

The photo-generated current increases with photon flux due to increasing laser power output which results in the observed increase in current as the laser power output is increased. When the laser power output is increased, the number of photons incident on the solar cell increases, which results in increase in the number of photo-generated



charge carriers. As the number of photo-generated charge carriers increase, the diffusion constant, mobility and carrier lifetime change [165]. At high injection, the mobility and diffusion constant reduce while the minority carrier lifetime increases. The increase in minority carrier lifetime increases  $V_{oc}$  and  $I_{sc}$ . The increase in  $I_{sc}$  is linear while  $V_{oc}$  increases logarithmically as shown in Figure 6.2.

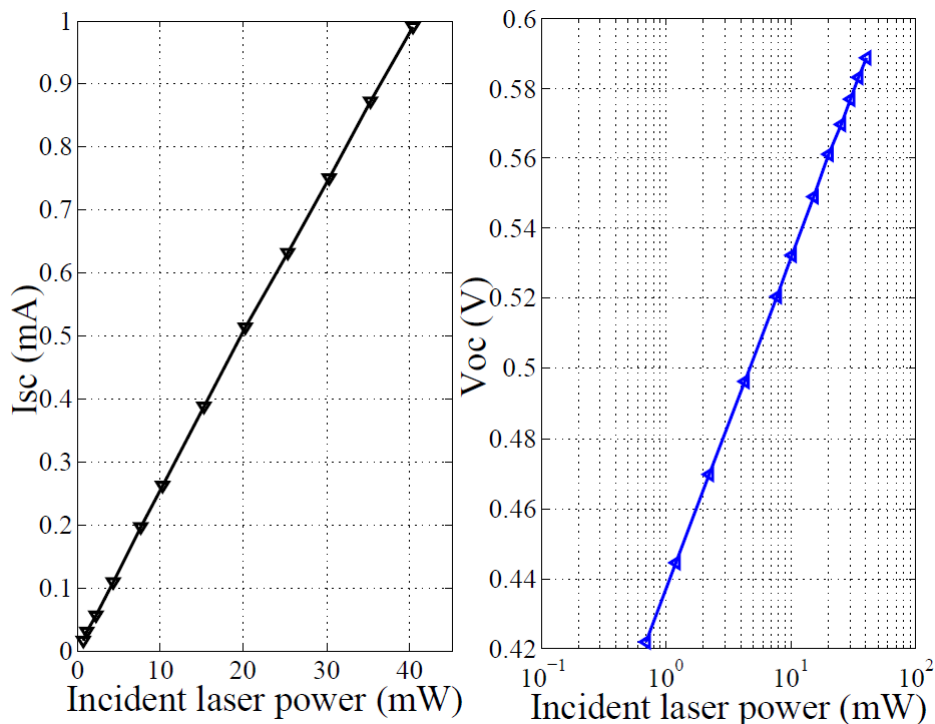


Figure 6.2: Variation of  $I_{sc}$  and  $V_{oc}$  with intensity for spot illuminated Back contact Back junction Si solar cell.

The increase in  $V_{oc}$  with intensity is due to the re-distribution of charge carriers that sets up a potential difference which results from the splitting of the thermal equilibrium Fermi level into the minority carrier electron quasi Fermi level and the minority carrier hole quasi Fermi level [75]. The difference between the quasi Fermi levels gives

$$V_{oc} \approx \frac{E_{FN} - E_{FP}}{q} \quad (6.1)$$

where  $E_{FN}$  and  $E_{FP}$  are electron and hole quasi Fermi levels respectively. As the intensity of the incident photons increases, the separation of the quasi Fermi levels increases further and hence  $V_{oc}$  also increases. Figure 6.3 shows the variation of series and shunt resistances with illumination intensity. The series resistance is observed to decrease with increasing intensity, decreasing sharply at low intensities, before levelling off at higher intensities, as earlier observed by Lal *et al.* [137] and Khan *et al.* [163] working on silicon solar cells. The decrease of  $R_s$  with illumination intensity is attributed to the increase in conductivity of the active layer with the increase in intensity of illu-

mination. The shunt resistance increases initially at low intensity before decreasing at higher illumination levels. The increase in  $R_{sh}$  with intensity at low illumination levels may be due to the presence of local inhomogeneities that lead to non-uniform current flow or to the charge leakage across the p-n junction in the cell [166]. This is because shunts are normally associated with defect regions that have a large concentration of traps. The traps make the defect regions electrically active and may act as sinks for the photo-generated charge carriers.

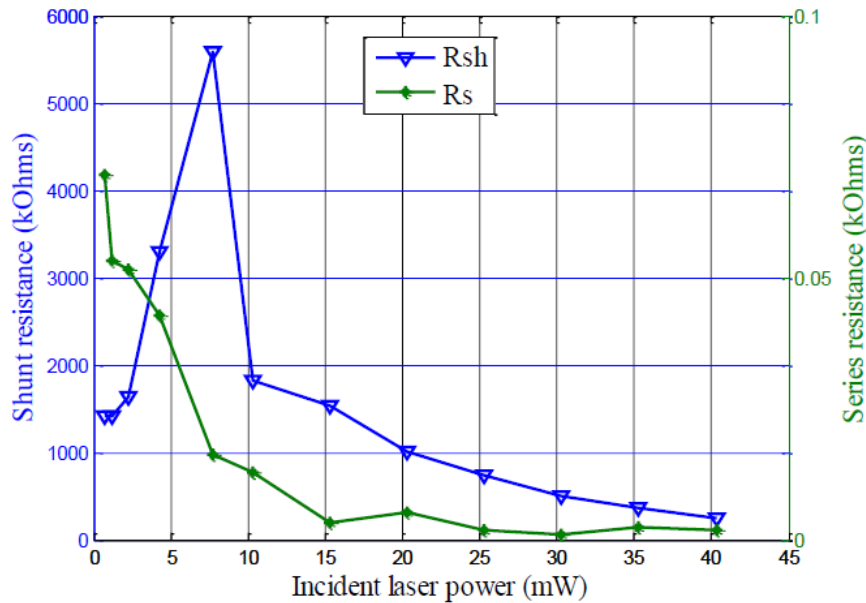


Figure 6.3: Shunt and series resistance as a function of illumination intensity.

As the illumination intensity increases, the traps begin to get filled up which leads to a reduction in the shunt current and thus increasing the shunt resistance. The shunt resistance attains a maximum value when all the traps are filled up [163]. However, as the intensity increases further, recombination centres may be introduced at the surface and within the bulk due to Auger recombination that becomes dominant at higher carrier densities, thus resulting in an effective decrease in the shunt resistance. In addition, secondary effects such as heating of the cell may contribute to a decrease in  $R_{sh}$  [167]. In Figure 6.4 the variation of ideality factor and saturation current with illumination intensity is presented showing an increase in  $n$  and  $I_o$  with intensity. The increase in  $n$  and  $I_o$  is attributed to an increase in the photo-induced recombination within the bulk as well as surface recombination processes due to increase in the density of defect states caused by the energy released from charge carrier recombination. As the charge carriers recombine, the energy released breaks the atomic bonds which may then act as defect states that create more recombination sites.

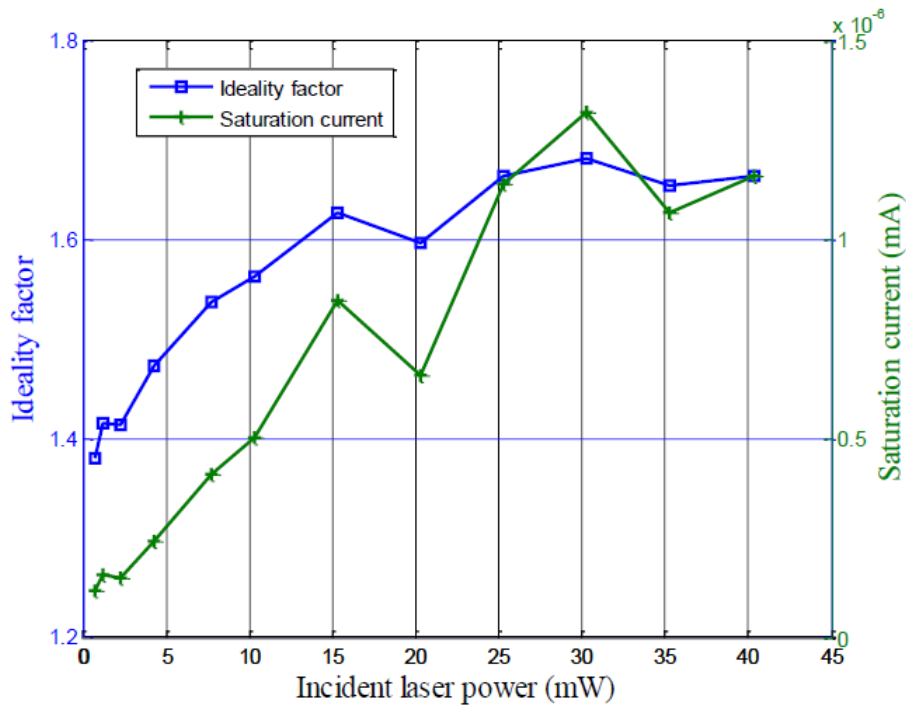


Figure 6.4: Ideality factor and saturation current as a function of illumination intensity.

## 6.3 Effect of spectral change

Spot illuminated and full cell illumination I-V characteristics were obtained to extract I-V parameters at different spectral conditions. These are presented and discussed in this section.

### 6.3.1 Back contact Back junction silicon solar cell

#### 6.3.1.1 Spot illumination

Under spot illumination, two lasers of wavelengths  $445\text{ nm}$  and  $785\text{ nm}$ , each with a power output of  $5\text{ mW}$  were used to obtain spot illuminated I-V characteristics at the two spectral conditions. These curves were fitted using the interval division algorithm to extract device and performance parameters. The measured and fitted I-V curves are shown in Figure 6.5 and the extracted parameters are listed in Table 6.1. The extracted performance parameters are observed to increase with wavelength due to the difference in the absorption coefficient and penetration depth of silicon at the two wavelengths. The absorption coefficient is a function of wavelength that determines the absorption of monochromatic light of a given wavelength.

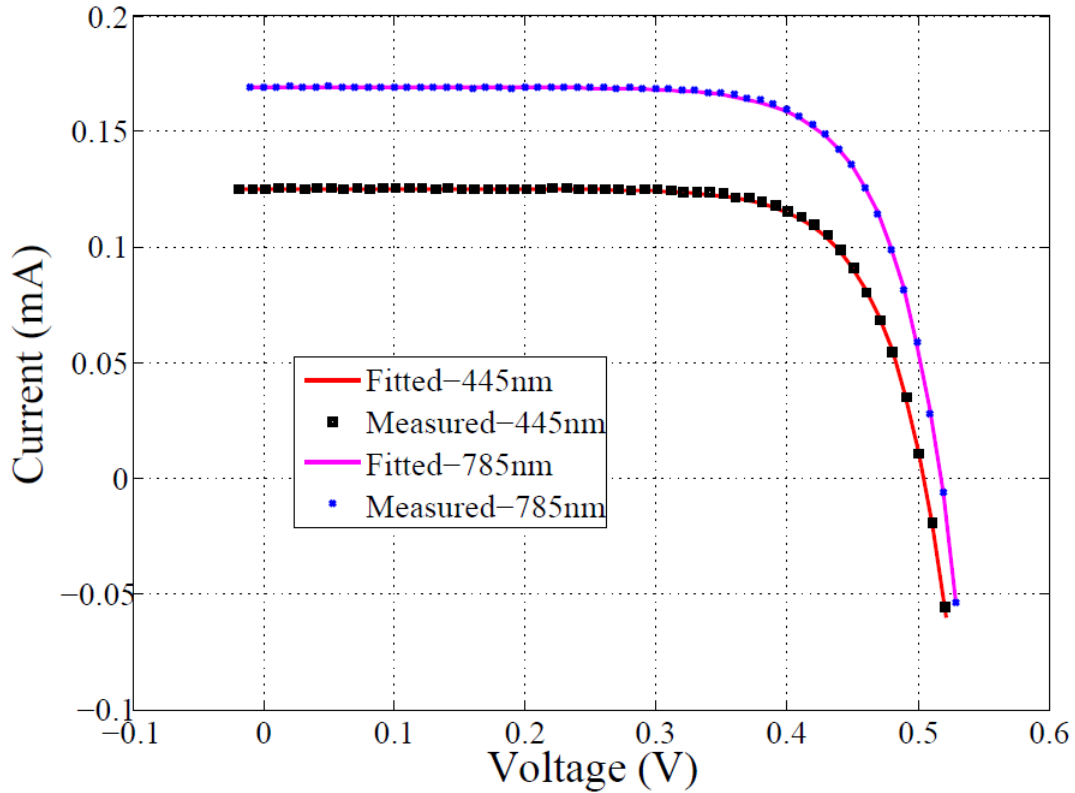


Figure 6.5: Measured and fitted I-V curves of Back contact Back junction silicon solar cell at two spectral conditions.

Table 6.1: Extracted parameters for a Back contact Back junction Si solar cell at two spectral conditions.

Laser source	Parameters						
	$n$	$I_o(A)$	$R_{sh}(M\Omega)$	$R_s(\Omega)$	$I_{sc}(mA)$	$V_{oc}(V)$	$FF$
445nm	1.58	$5.50 \times 10^{-10}$	3.362	15.97	0.125	0.504	0.728
785nm	1.62	$7.88 \times 10^{-10}$	1.655	2.42	0.169	0.517	0.730

The optical absorption coefficient of silicon and other semiconductor materials decreases with increasing wavelength as shown in Figure 6.6 [168]. Due to the high absorption coefficient of silicon for short wavelength radiations, radiations shorter than 500 nm are mainly absorbed in the front emitter region of the solar cell [169], enhancing charge carrier generation at the emitter (n-type) region of the solar cell. Charge carrier generation in the emitter is affected by surface recombination and the diffusion length as carriers generated close to the surface may recombine before they are collected by the p-n junction at the rear surface since they have to travel longer distances. This results in higher recombination losses that affects both  $I_{sc}$  and  $V_{oc}$  significantly. The device is also characterised by ideality factors less than 2 at the two spectral conditions with a higher ideality factor observed at longer wavelength radiations. The values of  $n$  and

$I_o$  are determined by the contribution of surface recombination, space charge and bulk recombination to the total recombination mechanisms taking place in the device.

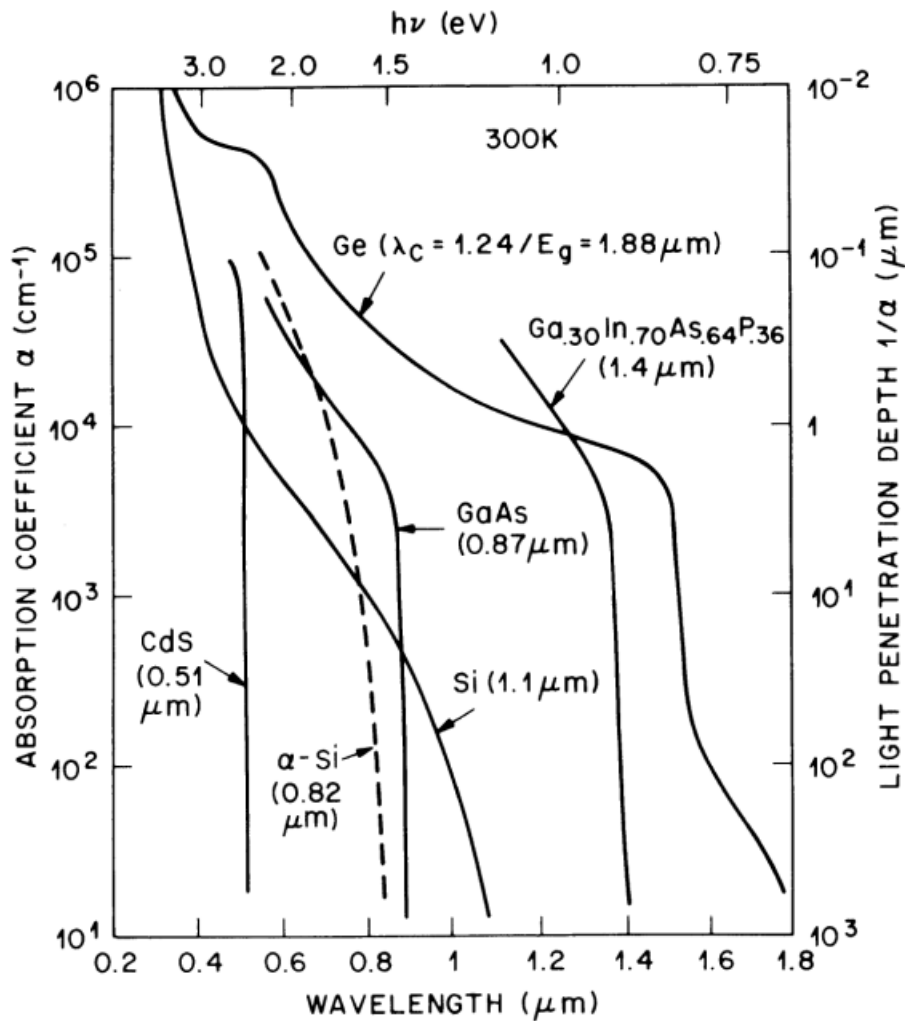


Figure 6.6: Optical absorption coefficients of various semiconductor materials.

### 6.3.1.2 Full cell illumination

I-V characteristics were obtained under full cell solar illumination, with the solar cell mounted on a two axis tracker. The solar spectral content was then changed using two long pass colour filters from Thorlabs, with cut off wavelengths of 610 nm and 1000 nm. The transmission for the filters as a function of wavelength is shown in Figure 6.7 [170].

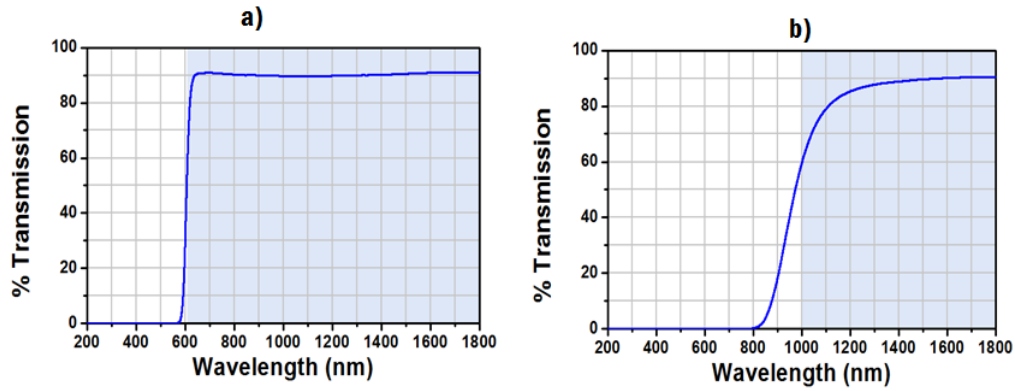


Figure 6.7: Transmission spectra for: a) the , b) long pass filters.

The measured I-V characteristics obtained at the three spectral conditions are shown in Figure 6.8 while the extracted I-V parameters are shown in Table 6.2.

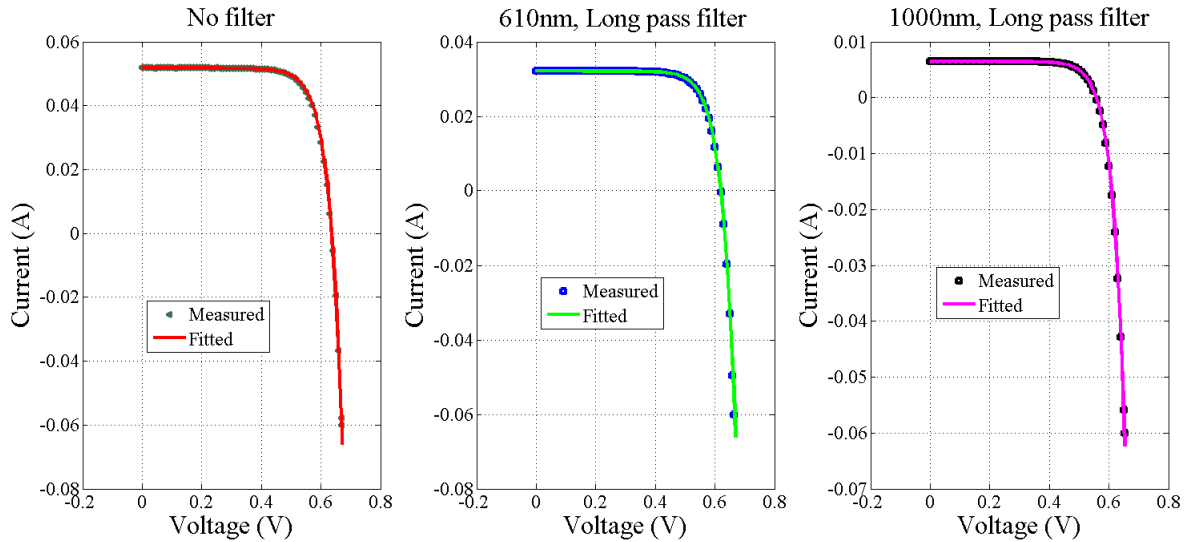


Figure 6.8: Measured and fitted full cell illumination I-V characteristics for a BC-BJ Si solar cell under different solar spectral conditions.

Table 6.2: Extracted I-V parameters of a Back contact Back junction Si solar cell under different spectral conditions.

	Parameters						
	$n$	$I_o(A)$	$R_{sh}(k\Omega)$	$R_s(\Omega)$	$I_{sc}(mA)$	$V_{oc}(V)$	$FF$
Full Solar beam	1.65	$1.75 \times 10^{-8}$	2.21	$1.95 \times 10^{-4}$	51.85	0.635	0.761
610 nm filter	1.59	$9.13 \times 10^{-9}$	3.82	$5.55 \times 10^{-2}$	32.19	0.619	0.760
1000 nm filter	1.55	$6.17 \times 10^{-9}$	20.99	$2.72 \times 10^{-3}$	6.47	0.557	0.750

The extracted performance parameters are observed to decrease with increase in cut off wavelength of the long pass filter. This decrease is due to the effect of the spectral

response of the device together with the decrease in the intensity of the radiation incident on the device as more radiation is cut off by the filters. A typical silicon solar cell spectral response is shown in Figure 6.9. When a 610 nm long pass filter is used,  $I_{sc}$  decreases by  $\sim 38\%$  while  $V_{oc}$  decreases by  $\sim 2.5\%$ . At a cut off wavelength of 1000 nm, the decrease in  $I_{sc}$  is  $\sim 87.5\%$  while  $V_{oc}$  is  $\sim 12.3\%$ . The decrease is thus higher at higher cut off wavelength since almost all the radiations within the spectral response range of the device have been cut off. The ideality factor and saturation current are also observed to decrease as the cut off wavelength is increased while the shunt resistance increases but there is no clear trend in the series resistance. The decrease in saturation current is attributed to a reduction in surface recombination as the shorter wavelength radiations are cut off, leaving the incident beam with only long wavelength radiations that penetrate deeper into the bulk material.

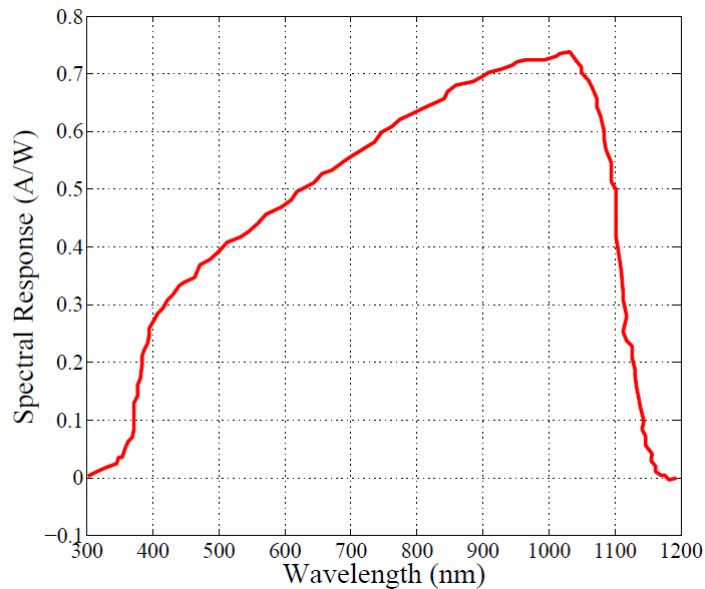


Figure 6.9: Spectral response of a Silicon solar cell.

### 6.3.2 Concentrating triple junction solar cell under full cell illumination

The amount of current generated by each subcell in a multijunction solar cell is determined by the spectral content of the beam incident on it and its spectral response. The spectral response of each subcell in the InGaP/InGaAs/Ge CTJ solar cell was shown in Figure 5.11. Changes in the spectral content of the incident beam will affect the current generated by each subcell and since the subcells are series connected, this may result in current mismatch, thus affecting the I-V characteristics and performance of the device. The effect of changing spectral content on the full cell illumination I-V characteristics and performance of the InGaP/InGaAs/Ge CTJ solar cell was investigated by changing

the spectral content of the incident solar beam using the 610 nm and a 1000 nm long pass colour filters. The measured and fitted I-V characteristics obtained with and without a filter are presented in Figure 6.10. When the 1000 nm long pass filter is used, a dark I-V curve is obtained even though the spectral response of the CTJ solar cell extends to  $\sim 1800$  nm. This is because radiations longer than 1000 nm will only activate the bottom Ge subcell while the top two subcells will not be activated and so do not produce any photo-current. Since the subcells are series connected, the photo-current from the CTJ solar cell is zero and so a dark I-V is obtained. A curve fitting algorithm was applied to the I-V curves obtained with no filter and with the 610 nm long pass filter to extract the I-V parameters shown in Table 6.3. Under solar illumination, the CTJ device attains a short circuit current of  $\sim 13.5$  mA,  $V_{oc}$  of  $\sim 2.6$  V and a fill factor of 0.86. The device also has a saturation current of  $\sim 3 \times 10^{-17}$  A and ideality factor  $\sim 3$ , consistent with reported values [157]. When the 610 nm long pass filter is used, the  $I_{sc}$  decreases to  $\sim 4$  mA while  $V_{oc}$  decreases to 2.56 V, representing  $\sim 70\%$  decrease in  $I_{sc}$  and  $\sim 2\%$  decrease in  $V_{oc}$ . This reduction is due to a decrease in the number of photons incident onto the device as the shorter wavelength radiations are cut off by the filter. In addition, due to a reduction in the amount of blue light incident on the CTJ device, the current from the top subcell decreases substantially and severely limits the  $I_{sc}$  of the CTJ solar cell .

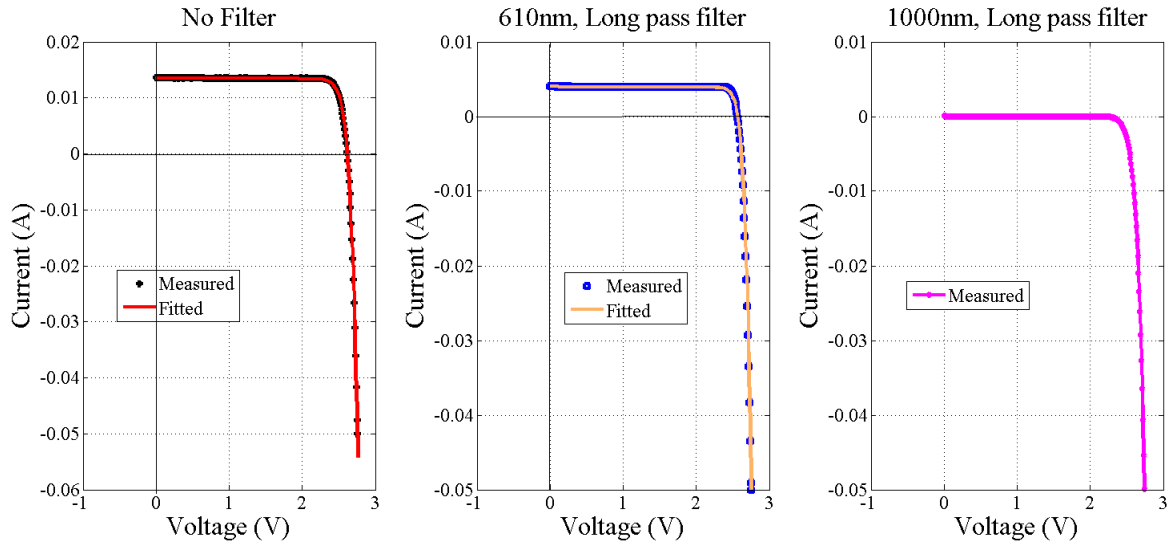


Figure 6.10: Measured and fitted full cell illumination I-V curves for a CTJ solar cell under different solar spectral conditions.

Table 6.3: Device and performance parameters of a CTJ solar cell extracted from I-V measurements obtained under two spectral conditions.

	Parameters						
	$n$	$I_o(A)$	$R_{sh}(k\Omega)$	$R_s(\Omega)$	$I_{sc}(mA)$	$V_{oc}(V)$	$FF$
Full Solar beam	2.99	$2.85 \times 10^{-17}$	20.05	0.34	13.54	2.61	0.86
610 nm filter	2.30	$7.35 \times 10^{-22}$	78.06	0.66	3.98	2.56	0.88



The decrease in current generated by the top subcell results in current mismatch that is shown by the increase in the fill factor. The ideality factor and the saturation current are also observed to decrease and this is attributed to the effect of current mismatch between the subcells since the shape of the I-V curve of a series connected multijunction device is determined by the I-V curve of the current limiting subcell. The analysis therefore shows that multijunction solar cell devices are sensitive to spectral changes in the incident beam compared to standard solar cells. The spectral sensitivity arises from the fact that current from multijunction solar cells with series connected subcells is determined by the subcell producing the least current. Since each subcell is tuned to respond to a specific range of wavelengths of the solar spectrum, any changes in the spectrum will affect the current output from each subcell and thus the overall device output. The sensitivity increases with increase in the number of series connected subcells since the spectral response range of each subcell is narrowed to accommodate the increasing number of subcells over the solar spectrum.

## 6.4 Conclusion

In this chapter, we investigated the effect of spectral change and intensity on the device and performance parameters of two concentrator solar cells. By varying the power output of the 445 nm wavelength laser from 0 to 45 mW, I-V curves of a spot illuminated BC-BJ Si solar cell were obtained at different intensities from which device and performance parameters were extracted. The short circuit current increased linearly while the open circuit voltage increased logarithmically with intensity. The series resistance decreased with intensity which was attributed to increase in conductivity of the active layer while the shunt resistance increased initially at low intensities but started to decrease as the intensity increased further. The ideality factor and the saturation current were observed to increase with intensity which was attributed to increase in recombination within the bulk and the surface. Under monochromatic spot illumination, the performance of BC-BJ Si solar cell was higher at 785 nm than at 445 nm due to higher spectral response of Si at 785 nm than at 445 nm. By changing the spectral content of the incident solar beam incident using a long pass colour filters with a cut off wavelengths of 610 nm and 1000 nm, the extracted parameters of the two concentrator solar cells were observed to change. The observed decrease in the performance parameters of the BC-BJ Si solar cell was attributed to a decrease in the number of incident photons as the shorter wavelength radiations were cut off by the filters. For the CTJ solar cell, the cut off of the radiations below 610 nm resulted in current mismatch that severely degraded the  $I_{sc}$ . The current mismatch affected the extracted device and performance parameters. With a 1000 nm long pass filter, a dark I-V was obtained since only the bottom Ge

subcell was activated.

The variation of extracted I-V parameters of a spot and or full cell illuminated solar cell with intensity and spectral content shows the importance of having a stable illumination source while performing LBIC/S-LBIC measurements. The output from the incident beam source should be stable in terms of intensity and spectral content as any variations could lead to mis-interpretation of results obtained from such measurements. This is especially crucial under outdoor conditions while performing S-LBIC measurements where the solar spectral content and intensity may change due to changing environmental conditions.

# Chapter 7

## Conclusion and outlook

The main aim of this work was to characterise solar cells in terms of photo-response using the LBIC mapping technique and parameter extraction from dark and illuminated I-V measurements so as to understand the impact and origin of non-uniformities on the performance of solar cell devices. Spatial inhomogeneities in the semiconductor starting material or variations in the device properties introduced during the device manufacturing processes can influence the performance of photovoltaic devices. This thesis presented the LBIC mapping technique, a non-destructive characterisation technique, to spatially map the photo-current response of concentrator solar cells point-by-point. The LBIC system for characterisation of solar cells was developed, compactly designed and optimised for use for both indoor and outdoor measurements. The system provides spatially resolved measurements and is an effective characterisation tool to reveal spatial non-uniformities in solar cell devices with relatively high resolution. By moving the solar cell device under study in a raster pattern under a fixed light beam source, the generated photo-current can be plotted as a function of position to obtain a photo-response map from which spatial non-uniformities and defects are identified. Incorporation of a reflection detector in the system allowed us to distinguish between optical impediments on the cell surface and other current reducing defects such as shunts. The device under test was dynamically biased by applying a sinusoidally varying voltage to obtain point-by-point I-V characteristics and to study the electrical activity of current reducing features at different biasing voltages. The LBIC/S-LBIC mapping technique was used to characterise a mc-Si solar cell and two concentrator solar cells: a Back contact Back junction (BC-BJ) silicon solar and an InGaP/InGaAs/Ge concentrating triple junction (CTJ) solar cell. The devices were characterised in terms of photo-response and parameter mapping using indoor and outdoor measurements.

The electrical activity of solar cells is normally described by measuring and interpreting their I-V characteristics using the single or double diode, lumped parameter equivalent circuit models. This involves extracting I-V parameters using parameter extraction

algorithms from the measured I-V characteristics taken either in the dark or under illumination conditions. In this thesis, a parameter extraction algorithm using an interval division method based on the lumped single diode equation but which could also be modified to use the double diode model was developed in Labview. The algorithm uses the measured I-V data and the initialised diode parameters to compute the modelled I-V curve by dividing the interval between the measured and modelled I-V curves using a user defined dividing factor for each parameter until a set tolerance for each parameter has been reached. To test its performance, the algorithm was applied to dark and illuminated I-V measurements of a mc-Si solar cell from which good agreement between measured and modelled I-V characteristics was realised. Extraction of parameter maps from LBIC measurements enabled the study of the spatial variation of device and performance parameters of the mc-Si solar cell, especially at areas containing defects observed in the photo-response maps.

Though BC-BJ silicon concentrator solar cells do not suffer from optical shading arising from the front grid metallisation since all the electrical contacts are located at the rear surface, they suffer from electrical shading due to recombination in regions that are not covered by a collecting emitter at the rear surface. The effect of electrical shading was observed as alternating regions of high and low induced current in the photo-response map of the solar cell. A defect characterised by low shunt resistance but high series and reverse saturation current was also observed in the photo-response map and was attributed to the presence of a precipitate or an inclusion introduced during the manufacturing process. A decrease in localised performance parameters over this defect as observed in the performance parameter maps is indicative of the detrimental effect of the defect over the performance of the device. A line scan through this defect at different biasing voltages revealed that its effect on photo-response was independent of the biasing voltage. Device parameters extracted from dark and full cell solar illumination I-V curves were characterised by high shunt and low series resistance, parameters that are particularly ideal for concentrator solar cells since they operate at high current densities. A concentrating triple junction solar cell was characterised using monochromatic and solar light beams. By illuminating the CTJ solar cell with a  $660\text{ nm}$  wavelength laser while applying a voltage bias, the InGaP and InGaAs subcells were activated while the Ge subcell could be activated through luminescent coupling by secondary luminescent photons emitted by the InGaAs middle subcell, thus enabling LBIC measurements to be obtained. However, point illuminated I-V curves obtained from LBIC measurements using the  $660\text{ nm}$  wavelength laser showed reverse bias voltage breakdown in the power quadrant which was attributed to the Ge subcell not being fully activated. The extracted parameters from the point illuminated I-V curve using the laser source as a beam probe were characteristic of a single subcell. Under solar illumination, reverse voltage breakdown was not observed in the power quadrant since all the subcells were fully activated

by the solar spectrum. Parameters extracted from dark and full cell solar illumination I-V characteristics showed high shunt and low series resistances which are ideal for concentrator solar cells. Device and performance parameter maps obtained from S-LBIC measurements did not show any distinct performance reducing features over the scanned area, an indication of the high quality of the CTJ solar cell device.

The BC-BJ silicon solar cell was subjected to changing intensity under spot illumination to study the effect of intensity variation on the I-V characteristics and performance of the device. The extracted device and performance parameters were observed to change with varying intensity of the beam probe. In particular,  $V_{oc}$  was observed to increase logarithmically while  $I_{sc}$  increased linearly over the intensity range considered. The series resistance was observed to decrease with intensity which was attributed to increase in conductivity while the shunt resistance initially increased before decreasing at higher intensities due to the presence of localised defect regions with a large concentration of traps. The increase in ideality factor and saturation current with intensity was attributed to photo-induced recombination within the bulk as well as surface recombination processes. Under monochromatic illumination, the extracted performance parameters for the BC-BJ Si solar cell were higher at a wavelength of  $785\text{ nm}$  than at  $445\text{ nm}$  due to high absorption coefficient of Si for shorter wavelength radiations that results in carrier generation close to the surface, where there is a higher probability of recombination before being collected at the p-n junction. Under full solar spectrum, the performance parameters were observed to decrease as the incident photons with wavelengths below  $610\text{ nm}$  and then  $1000\text{ nm}$  were blocked using the long pass colour filters. The observed decrease in the performance parameters of the BC-BJ Si solar cell was attributed to a decrease in the number of incident photons as the shorter wavelength radiations were cut off by the filters. For the CTJ solar cell, the cut off of the radiations below  $610\text{ nm}$  resulted in current mismatch that severely degraded the  $I_{sc}$ . The current mismatch affected the extracted device and performance parameters. With a  $1000\text{ nm}$  long pass filter, a dark I-V was obtained since only the bottom Ge subcell was activated. Characterisation of solar cells in terms of photo-response and parameter mapping using measurements obtained from LBIC measurements has been achieved in this thesis. The LBIC mapping technique is able to give very high spatial resolution measurements if a highly focused beam and appropriate step size are used. Practical difficulties were encountered, however, while manually focusing the incident beam onto the solar cell sample to obtain an appropriate spot size, and was time consuming. The use of an automated focusing system incorporated into the scanning routine to optimise the focusing of the incident beam onto the sample is proposed. In addition, challenges remain in identifying a suitable model applicable to LBIC measurements as only a small part of the solar cell is illuminated while the rest of the device is in the dark. The situation becomes even more complex when applied to two terminal monolithic multijunction devices. The

single or the double diode model may serve as a starting point to a more refined model. In addition, for future research with multijunction solar cells continuing from this work, use of appropriate light biasing so as to isolate and characterise individual subcells in the stack is proposed, to extract subcell parameters. The individual subcell parameters can be comparatively analysed with the multijunction device parameters to yield information that can be crucial in formulating a suitable model for multijunction devices.

# Bibliography

- [1] NS Lewis and G Crabtree. Basic Research Needs for Solar Energy Utilization: Report of the Basic Energy Sciences Workshop on Solar Energy Utilization, April 18-21, 2005. Technical report, U.S. Department of Energy, Office of Basic Energy Sciences, 2005.
- [2] BP Statistical Review of World Energy 2014. Technical report, British Petroleum (BP), Available at <http://www.bp.com/content/dam/bp/pdf/Energy-economics/statistical-review-2014/BP-statistical-review-of-world-energy-2014-full-report.pdf>, Accessed on 10/10/2014.
- [3] S Solomon, D Qin, M Manning, Z Chen, M Marquis, KB Averyt, M Tignor, and HL Miller. Summary for Policy makers In: Climate Change 2007: The Physical Science Basis. Contribution of Working Group I to the Fourth Assessment Report of the Inter-governmental Panel on Climate Change. Technical report, Intergovernmental Panel on Climate Change (IPCC), 2007.
- [4] P Frankl and S Nowak. *Technology roadmap: Solar Photovoltaic Energy*. OECD/IEA, 2010.
- [5] Renewables 2014 Global Status Report. Technical report, REN21, Available at <http://www.ren21.net/Portals/0/documents/Resources/GSR/2014/GSR2014-full%20report-low%20res.pdf>, Accessed on 21/10/2014.
- [6] GR Timilsina, L Kurdgelashvili, and PA Narbel. Solar energy: Markets, economics and policies. *Renewable and Sustainable Energy Reviews*, 16(1):449–465, 2012.
- [7] W Palz. *Power for the World: The Emergence of Electricity from the Sun*. Pan Stanford Publishing, 2010.
- [8] DM Chapin, CS Fuller, and GL Pearson. A new silicon p-n junction photocell for converting solar radiation into electrical power. *J Appl Phys*, 25(5):676–677, 1954.
- [9] W Shockley and HJ Queisser. Detailed balance limit of efficiency of p-n junction solar cells. *Journal of applied physics*, 32(3):510–519, 1961.

- [10] L Fraas and L Partain. *Solar cells and their applications*, chapter Solar Cells: A brief History and Introduction, pages 3–15. John Wiley & Sons, 2010.
- [11] SW Glunz, R Preu, and D Biro. *Comprehensive Renewable Energy*, chapter C1.16 - Crystalline Silicon Solar Cells: State-of-the-Art and Future Developments, pages 353–387. El, 2012.
- [12] S Xiao and S Xu. High-efficiency silicon solar cells-materials and devices physics. *Critical Reviews in Solid State and Materials Sciences*, 39(4):277–317, 2014.
- [13] NREL. *All solar efficiency breakthroughs since 1975 on a single chart*. National Renewable Energy Laboratory (NREL), September 2014.
- [14] G Masson, M Latour, M Reking, I Theologitis, and M Papoutsis. Global market outlook for photovoltaics 2013-2017. *European Photovoltaic Industry Association (EPIA), European Commission May*, 2013.
- [15] SP Philipps, W Guter, E Welsch, J Schöne, M Steiner, F Dimroth, and AW Bett. Present status in the development of III-V multijunction solar cells. In *Next Generation of Photovoltaics*, pages 1–21. Springer, 2012.
- [16] DE Sawyer and HK Kessler. Laser scanning of solar cells for the display of cell operating characteristics and detection of cell defects. *Electron Devices, IEEE Transactions on*, 27(4):864–872, 1980.
- [17] RM Swanson. The promise of concentrators. *Progress in Photovoltaics Research and Applications*, 8(1):93–111, 2000.
- [18] RK Jones, JH Ermer, CM Fetzer, and RR King. Evolution of multijunction solar cell technology for concentrating photovoltaics. *Japanese Journal of Applied Physics*, 51(10S):10ND01, 2012.
- [19] G Sala and A Luque. Past experiences and new challenges of PV concentrators. *Concentrator Photovoltaics (Springer Series in Optical Sciences Volume 130)*, 130:1–23, 2007.
- [20] Solar Resource Overview. Technical report, GeoModel Solar, Available at <http://solargis.info/doc/-docs/SolarGIS-TS-min15-PSADLR-PSA-Tabernas-Almeria-Spain-19940101-20131231.pdf>, Accessed on 30/05/2014.
- [21] DJ Friedman, RR King, RM Swanson, J McJannet, and D Gwinner. Editorial: Toward 100 gigawatts of concentrator photovoltaics by 2030. *IEEE Journal of Photovoltaics*, 3(4):1460–1463, 2013.



- [22] DR Myers, K Emery, and C Gueymard. Proposed reference spectral irradiance standards to improve concentrating photovoltaic system design and performance evaluation. In *Photovoltaic Specialists Conference, 2002. Conference Record of the Twenty-Ninth IEEE*, pages 923–926. IEEE, 2002.
- [23] Lu ZHAO. *High Efficiency Mechanically Stacked Multijunction Solar Cells for Concentrator Photovoltaics*. PhD thesis, Catholic University of Leuven, 2011.
- [24] DR Myers, K Emery, and C Gueymard. Revising and validating spectral irradiance reference standards for photovoltaic performance evaluation. *Journal of solar energy engineering*, 126(1):567–574, 2004.
- [25] K Emery, D Myers, and S Kurtz. What is the appropriate reference spectrum for characterizing concentrator cells? In *Photovoltaic Specialists Conference, 2002. Conference Record of the Twenty-Ninth IEEE*, pages 840–843, 2002.
- [26] MA Green. *Solar cells: Operating principles, technology, and system applications*, volume 1. The University of New South Wales, 1992.
- [27] JL Gray. The physics of the solar cell. *Handbook of photovoltaic science and engineering*, 2:82–128, 2003.
- [28] MA Green. *Silicon Solar Cells: Advanced Principles & Practice*, volume 20. Centre for Photovoltaic Devices and Systems, University of New South Wales, 1995.
- [29] SM Sze. *Physics of semiconductor devices, 1981*. Wiley, New York, 2nd edition, 1981.
- [30] J Nelson. *The physics of solar cells*. Imperial College Press, 2003.
- [31] DK Schroder. Carrier lifetimes in silicon. *Electron Devices, IEEE Transactions on*, 44(1):160–170, 1997.
- [32] D Macdonald and A Cuevas. Validity of simplified Shockley-Read-Hall statistics for modeling carrier lifetimes in crystalline silicon. *Physical Review B*, 67(7):075203, 2003.
- [33] S Rein. *Lifetime spectroscopy: A method of defect characterization in silicon for photovoltaic applications*, volume 85. Springer, 2006.
- [34] MZ Rahman and SI Khan. Advances in surface passivation of c-Si solar cells. *Materials for Renewable and Sustainable Energy*, 1(1):1–11, 2012.
- [35] CS Solanki. *Solar photovoltaics: Fundamentals, technologies and applications*. PHI Learning Pvt. Ltd., 2011.

- [36] P Mialhe, B Affour, K El-Hajj, and A Khoury. High injection effects on solar cell performances. *Active and Passive Electronic Components*, 17(4):227–232, 1995.
- [37] PP Altermatt, J Schmidt, G Heiser, and AG Aberle. Assessment and parameterisation of coulomb-enhanced auger recombination coefficients in lowly injected crystalline silicon. *Journal of Applied Physics*, 82(10):4938–4944, 1997.
- [38] MA Green. *Third Generation Photovoltaics: Advanced Solar Energy Conversion*, volume 12. Springer, 2006.
- [39] B Moralejo, MA González, J Jiménez, V Parra, O Martínez, J Gutiérrez, and O Charro. LBIC and reflectance mapping of multi-crystalline si solar cells. *Journal of electronic materials*, 39(6):663–670, 2010.
- [40] WF Mohamed and KK Mohammed. Infrared response and quantum efficiency of in-doped silicon (n) structure. *Renewable energy*, 21(3):323–331, 2000.
- [41] W Peter. *Physics of Solar Cells: From Principles to New Concepts*. John Wiley & Sons, 2008.
- [42] RM Swanson. *Handbook of Photovoltaic Science and Engineering*, chapter Photovoltaic concentrators. John Wiley & Sons, 2003.
- [43] P Pérez-Higueras, E Munoz, G Almonacid, and PG Vidal. High concentrator photovoltaics efficiencies: Present status and forecast. *Renewable and Sustainable Energy Reviews*, 15(4):1810–1815, 2011.
- [44] A Antonini. Photovoltaic concentrators—fundamentals, applications, market & prospective. *Solar Collectors and Panels, Theory and Applications, Sciyo*, pages 31–54, 2010.
- [45] PJ Verlinden. *Solar Cells (Second Edition)*, chapter IC-5- High efficiency Back-Contact Silicon Solar Cells for one Sun and Concentrator Applications, pages 327–351. Elsevier, 2013.
- [46] A Blakers. *Concentrator Photovoltaics*, chapter Silicon concentrator solar cells. Springer, 2007.
- [47] RA Sinton, Y Kwark, JY Gan, and RM Swanson. 27.5-percent silicon concentrator solar cells. *Electron Device Letters, IEEE*, 7(10):567–569, 1986.
- [48] SW Glunz, J Dicker, D Kray, JY Lee, R Preu, S Rein, E Schneiderlöchner, J Sölter, W Warta, and G Willeke. High-efficiency cell structures for medium-quality silicon. *Proc. 17th PVSEC*, 2001.

- [49] K Kotsovos and K Misiakos. *Trends in Solar Energy Research*, chapter Three-dimensional simulation of Base Carrier Transport effects in Back side point contact Silicon solar cells, pages 47–76. Nova Science Publishers Inc, 2006.
- [50] EV Kerschaver and G Beaucarne. Back-contact solar cells: A review. *Progress in Photovoltaics: Research and Applications*, 14(2):107–123, 2006.
- [51] F Granek. *High efficiency back-contact back-junction silicon solar cells*. PhD thesis, Albert-Ludwigs-University, Freiberg, Germany, 2009.
- [52] DS Kim, V Meemongkolkiat, A Ebong, B Rounsaville, V Upadhyaya, A Das, and A Rohatgi. 2d-modeling and development of interdigitated back contact solar cells on low-cost substrates. In *Photovoltaic Energy Conversion, Conference Record of the 2006 IEEE 4th World Conference on*, volume 2, pages 1417–1420. IEEE, 2006.
- [53] SH Lee and A Rehman. Advancements in n-type base crystalline silicon solar cells and their emergence in the photovoltaic industry. *The Scientific World Journal*, 2013, 2013.
- [54] MD Lammert and RJ Schwartz. The interdigitated back contact solar cell: A silicon solar cell for use in concentrated sunlight. *Electron Devices, IEEE Transactions on*, 24(4):337–342, 1977.
- [55] R Bock, S Mau, J Schmidt, and R Brendel. Back-junction back-contact n-type silicon solar cells with screen-printed aluminum-alloyed emitter. *Applied Physics Letters*, 96(26):263507–263507, 2010.
- [56] R Keding, D Stuwe, M Kamp, C Reichel, A Wolf, R Woehl, D Borchert, H Reinecke, and D Biro. Co-diffused back-contact back-junction silicon solar cells without Gap regions. 2013.
- [57] CM Garner, RD Nasby, and FW Sexton. An interdigitated back contact solar cell with high-current collection. *Electron Device Letters, IEEE*, 1(12):256–258, 1980.
- [58] M Hermle, F Granek, O Schultz-Wittmann, and SW Glunz. Shading effects in back-junction back-contacted silicon solar cells. In *Photovoltaic Specialists Conference, 2008. PVSC'08. 33rd IEEE*, pages 1–4. IEEE, 2008.
- [59] C Reichel, F Granek, M Hermle, and SW Glunz. Investigation of electrical shading effects in back-contacted back-junction silicon solar cells using the two-dimensional charge collection probability and the reciprocity theorem. *Journal of Applied Physics*, 109(2):024507, 2011.

- [60] PJ Cousins, DD Smith, H Luan, J Manning, TD Dennis, A Waldhauer, KE Wilson, G Harley, and WP Mulligan. Generation 3: Improved performance at lower cost. In *Photovoltaic Specialists Conference (PVSC), 2010 35th IEEE*, pages 275–278. IEEE, 2010.
- [61] JM Gee, WK Schubert, and PA Basore. Emitter wrap-through solar cell. In *Photovoltaic Specialists Conference, 1993., Conference Record of the Twenty Third IEEE*, pages 265–270. IEEE, 1993.
- [62] SW Glunz. High-efficiency crystalline silicon solar cells. *Advances in Optoelectronics*, 2007, 2007.
- [63] F Kiefer, C Ulzhofer, T Brendemuhl, NP Harder, R Brendel, V Mertens, S Bordihn, C Peters, and JW Muller. High efficiency N-type emitter-wrap-through silicon solar cells. *IEEE Journal of Photovoltaics*, 1(1):49–53, 2011.
- [64] IG Romijn, AA Mewe, MWPE Lamers, E Kossen, EE Bende, and AW Weeber. An overview of MWT cells and evolution to the ASPIRE concept: A new integrated mc-si cell and module design for high-efficiencies. In *Proceedings of the 23rd European Photovoltaic Solar Energy Conference, Valencia, Spain, 2008*.
- [65] F Clement, B Thaidigsmann, R Hoenig, T Fellmeth, A Spribille, E Lohmueller, A Krieg, M Glatthaar, H Wirth, and D Biro. Pilot-line processing of highly-efficient MWT silicon solar cells. In *Proceedings of the 25th European Photovoltaic Solar Energy Conference and Exhibition, 2010*.
- [66] T Fellmeth, M Menkoe, F Clement, D Biro, and R Preu. Highly efficient industrially feasible metal wrap through (MWT) silicon solar cells. *Solar Energy Materials and Solar Cells*, 94(12):1996–2001, 2010.
- [67] SP Philipps, F Dimroth, and AW Bett. *Solar Cells (Second Edition)*, chapter IC6 High Efficiency III-V Multi-junction Solar Cells, pages 353–381. Elsevier, 2013.
- [68] G Kinsey. High-concentration, III-V multijunction solar cells. *Solar Cells and Their Applications*, 217:293, 2010.
- [69] BE Sagol, U Seidel, N Szabó, K Schwarzburg, and T Hannappel. Basic concepts and interfacial aspects of high-efficiency III-V multijunction solar cells. *CHIMIA International Journal for Chemistry*, 61(12):775–779, 2007.
- [70] NV Yastrebova. High-efficiency multijunction solar cells: Current status and future potential. *Solar Energy*, 2007.
- [71] JM Olson, DJ Friedman, and S Kurtz. High-efficiency III-V multijunction solar cells, 2003.

- [72] AW Bett, F Dimroth, and G Siefert. Multijunction concentrator solar cells. *Concentrator Photovoltaics (Springer Series in Optical Sciences Volume 130)*, 130:67–87, 2007.
- [73] RW Miles, KM Hynes, and I Forbes. Photovoltaic solar cells: An overview of state-of-the-art cell development and environmental issues. *Progress in Crystal Growth and Characterization of Materials*, 51(1):1–42, 2005.
- [74] JD McCambridge, MA Steiner, BL Unger, KA Emery, EL Christensen, MW Wanlass, AL Gray, L Takacs, R Buelow, TA McCollum, et al. Compact spectrum splitting photovoltaic module with high efficiency. *Progress in Photovoltaics: Research and Applications*, 19(3):352–360, 2011.
- [75] H Cotal, C Fetzer, J Boisvert, G Kinsey, R King, P Hebert, H Yoon, and N Karam. III-V multijunction solar cells for concentrating photovoltaics. *Energy & Environmental Science*, 2(2):174–192, 2009.
- [76] G Segev, G Mittelman, and A Kribus. Equivalent circuit models for triple-junction concentrator solar cells. *Solar Energy Materials and Solar Cells*, 98:57–65, 2012.
- [77] SM Samberg, JPand Bedair. Current matching for high efficiency multijunction solar cells. *J Elec Electron*, 1, 2012.
- [78] DC Law, RR King, H Yoon, MJ Archer, A Boca, CM Fetzer, S Mesropian, T Isshiki, M Haddad, KM Edmondson, et al. Future technology pathways of terrestrial III-V multijunction solar cells for concentrator photovoltaic systems. *Solar Energy Materials and Solar Cells*, 94(8):1314–1318, 2010.
- [79] W Guter, J Schöne, SP Philipps, M Steiner, G Siefert, A Wekkeli, E Welser, E Oliva, AW Bett, and F Dimroth. Current-matched triple-junction solar cell reaching 41.1% conversion efficiency under concentrated sunlight. *Applied Physics Letters*, 94(22):223504–1–223504–3, 2009.
- [80] F Dimroth, W Guter, J Schone, E Welser, M Steiner, E Oliva, A Wekkeli, G Siefert, SP Philipps, and AW Bett. Metamorphic GaInP/GaInAs/Ge triple-junction solar cells with 41% efficiency. In *Photovoltaic Specialists Conference (PVSC), 2009 34th IEEE*, pages 1038–1042. IEEE, 2009.
- [81] RR King, D Bhusari, D Larrabee, X-Q Liu, E Rehder, K Edmondson, H Cotal, RK Jones, JH Ermer, CM Fetzer, et al. Solar cell generations over 40% efficiency. *Progress in Photovoltaics: Research and Applications*, 20(6):801–815, 2012.

- [82] JR Sites and TJ Nagle. LBIC analysis of thin-film polycrystalline solar cells. In *Photovoltaic Specialists Conference, 2005. Conference Record of the Thirty-first IEEE*, pages 199–204. IEEE, 2005.
- [83] FJ Vorster. *On the evaluation of photovoltaic concentrator system*. PhD thesis, Nelson Mandela Metropolitan University, 2008.
- [84] M Boostandoost, X Ycaza, R Leihkauf, U Kerst, and C Boit. Challenges for parametric analysis of the solar cells using failure analysis technique developed for the microelectronics. In *ISTFA: Conference Proceedings from the 38th International Symposium for Testing and Failure Analysis*, pages 255–263, 2012.
- [85] SR Dhariwal, LS Kothari, and SC Jain. Saturation of photovoltage and photocurrent in p-n junction solar cells. *Electron Devices, IEEE Transactions on*, 23(5):504–507, 1976.
- [86] JP Boyeaux and A Laugier. LBIC quantitative mapping. *Le Journal de Physique Colloques*, 50(C6):C6–111, 1989.
- [87] FJ Vorster and EE van Dyk. Bias-dependent high saturation solar LBIC scanning of solar cells. *Solar energy materials and solar cells*, 91(10):871–876, 2007.
- [88] JD Zook. Effects of grain boundaries in poly-crystalline solar cells. *Applied Physics Letters*, 37(2):223–226, 2008.
- [89] C Donolato. Theory of beam induced current characterization of grain boundaries in polycrystalline solar cells. *Journal of Applied Physics*, 54(3):1314–1322, 1983.
- [90] V Khanna, OS Sastry, AK Mukerjee, and KL Chopra. Automatic laser scanner for solar cells. *Review of scientific instruments*, 55(10):1580–1584, 1984.
- [91] J Martin, C Fernández-Lorenzo, JA Poce-Fatou, and R Alcantara. A versatile computer-controlled high-resolution LBIC system. *Progress in photovoltaics: Research and Applications*, 12(4):283–295, 2004.
- [92] J Carstensen, G Popkirov, J Bahr, and H Föll. CELLO: An advanced LBIC measurement technique for solar cell local characterization. *Solar energy materials and solar cells*, 76(4):599–611, 2003.
- [93] P Vorasayan, TR Betts, R Gottschalg, and AN Tiwari. Characterisation of a LBIC system by scanning of silicon solar cells and modules. 2007.
- [94] JF Hiltner and JR Sites. High resolution laser stepping measurements on polycrystalline solar cells. In *16th European Photovoltaic Solar Energy Conference*, 2000.

- [95] P Vorasayan, TR Betts, R Gottschalg, and AN Tiwari. Structural analysis of thin film silicon PV modules by means of large area laser beam induced current measurements. 2006.
- [96] T Michel, R Gottschalg, and DG Infield. Large area laser scanning of amorphous silicon modules. In *19th European Photovoltaic Solar Energy Conference*, pages 2522–2524, 2004.
- [97] FJ Vorster and EE van Dyk. High saturation solar light beam induced current scanning of solar cells. *Review of scientific instruments*, 78(1):013904, 2007.
- [98] A Kaminski, O Breitenstein, JP Boyeaux, P Rakotoniaina, and A Laugier. Light beam induced current and infrared thermography studies of multicrystalline silicon solar cells. *Journal of Physics: Condensed Matter*, 16(2):S9, 2004.
- [99] O Breitenstein, J Bauer, and JP Rakotoniaina. Material-induced shunts in multicrystalline silicon solar cells. *Semiconductors*, 41(4):440–443, 2007.
- [100] J Navas, R Alcántara, C Fernández-Lorenzo, and J Martín-Calleja. Trichromatic high resolution-LBIC: A system for the micrometric characterization of solar cells. *InTech*, 2011.
- [101] R Corkish, T Puzzer, AB Sproul, and KL Luke. Quantitative interpretation of electron-beam-induced current grain boundary contrast profiles with application to silicon. *Journal of applied physics*, 84(10):5473–5481, 1998.
- [102] HJ Fitting, H Glaefeke, and W Wild. Electron penetration and energy transfer in solid targets. *physica status solidi (a)*, 43(1):185–190, 1977.
- [103] J Marek. Light Beam Induced Current characterization of grain boundaries. *J Appl Phys*, 55(2):318–326, 1984.
- [104] G Micard, G Hahn, A Zuschlag, S Seren, and B Terheiden. Quantitative evaluation of grain boundary activity in multi-crystalline semiconductors by light beam induced current: An advanced model. *Journal of Applied Physics*, 108(3):034516, 2010.
- [105] C Donolato. Beam induced current characterization in polycrystalline semiconductors. In *Polycrystalline Semiconductors*, pages 138–154. Springer, 1985.
- [106] C Fernández-Lorenzo, JA Poce-Fatou, R Alcántara, J Navas, and J Martín. High resolution laser beam induced current focusing for photoactive surface characterization. *Applied Surface Science*, 253(4):2179–2188, 2006.

- [107] <http://www.coherent.com/Products/?1007/CUBE-Lasers>, Accessed on 07/04/2014.
- [108] Thorlabs Reflective Objective, <http://www.thorlabs.com/>, Accessed on 03/02/2014.
- [109] Motion control stages, <http://www.pimicos.com>, Accessed on 11/03/2013.
- [110] SR570 User Manual, <http://www.thinksrs.com/downloads/PDFs/Manuals/SR570m.pdf>, Accessed on 10/02/2014.
- [111] B Sopori, P Rupnowski, V Mehta, V Budhraj, S Johnston, N Call, H Mountinho, M Al-Jassim, A Shaikh, M Seacrist, et al. Performance limitations of mc-Si solar cells caused by defect clusters. *ECS Transactions*, 18(1):1049–1058, 2009.
- [112] JL Maurice. On the origin of the electrical activity in silicon grain boundaries. *Revue de Physique Appliquée*, 22(7):613–621, 1987.
- [113] W Dimassi, M Bouaïcha, H Nouri, MF Boujmil, BS Nasrallah, and B Bessaïs. Grooving of grain boundaries in multi-crystalline silicon: Effect on solar cell performance. *Nuclear Instruments and Methods in Physics Research Section B: Beam Interactions with Materials and Atoms*, 253(1):260–263, 2006.
- [114] J Oualid, CM Singal, J Dugas, JP Crest, and H Amzil. Influence of illumination on the grain boundary recombination velocity in silicon. *Journal of applied physics*, 55(4):1195–1205, 1984.
- [115] M Mauk, P Sims, J Rand, and A Barnett. Thin silicon solar cells. *Practical Handbook of Photovoltaics: Fundamentals and Applications*, page 185, 2003.
- [116] EQB Macabebe and EE van Dyk. Parameter extraction from dark current-voltage characteristics of solar cells. *South African Journal of Science*, 104(9-10):401–404, 2008.
- [117] K Bouzidi, M Chegaar, and M Aillerie. Solar cells parameters evaluation from dark IV characteristics. *Energy Procedia*, 18:1601–1610, 2012.
- [118] M Haouari-Merbah, M Belhamel, I Tobias, and JM Ruiz. Extraction and analysis of solar cell parameters from the illuminated current–voltage curve. *Solar Energy Materials and Solar Cells*, 87(1):225–233, 2005.
- [119] M Chegaar, G Azzouzi, and P Mialhe. Simple parameter extraction method for illuminated solar cells. *Solid-State Electronics*, 50(7):1234–1237, 2006.



- [120] MK Munji, W Okullo, EE van Dyk, and FJ Vorster. Local device parameter extraction of a concentrator photovoltaic cell under solar spot illumination. *Solar Energy Materials and Solar Cells*, 94(12):2129–2136, 2010.
- [121] K Bouzidi, M Chegaar, M Aillerie, and JP Charles. Contribution to the evaluation of the illuminated solar cells parameters. *Renewable Energies and Power Quality Journal*, 2010.
- [122] DSH Chan and JCH Phang. Analytical methods for the extraction of solar-cell single- and double-diode model parameters from IV characteristics. *Electron Devices, IEEE Transactions on*, 34(2):286–293, 1987.
- [123] A Jain and A Kapoor. Exact analytical solutions of the parameters of real solar cells using Lambert W-function. *Solar Energy Materials and Solar Cells*, 81(2):269–277, 2004.
- [124] A Ortiz-Conde, FJ García Sánchez, and J Muci. New method to extract the model parameters of solar cells from the explicit analytic solutions of their illuminated I-V characteristics. *Solar Energy Materials and Solar Cells*, 90(3):352–361, 2006.
- [125] C Zhang, J Zhang, Y Hao, Z Lin, and C Zhu. A simple and efficient solar cell parameter extraction method from a single current-voltage curve. *Journal of applied physics*, 110(6):064504, 2011.
- [126] N Enebish, D Agchbayar, S Dorjkhand, D Baatar, and I Ylemj. Numerical analysis of solar cell current-voltage characteristics. *Solar energy materials and solar cells*, 29(3):201–208, 1993.
- [127] L Sandrolini, M Artioli, and U Reggiani. Numerical method for the extraction of photovoltaic module double-diode model parameters through cluster analysis. *Applied Energy*, 87(2):442–451, 2010.
- [128] F Ghani, Mike Duke, and J Carson. Numerical calculation of series and shunt resistance of a photovoltaic cell using the Lambert W-function: Experimental evaluation. *Solar Energy*, 87:246–253, 2013.
- [129] DL King, BR Hansen, JA Kratochvil, and MA Quintana. Dark current-voltage measurements on photovoltaic modules as a diagnostic or manufacturing tool. In *Photovoltaic Specialists Conference, 1997., Conference Record of the Twenty-Sixth IEEE*, pages 1125–1128. IEEE, 1997.
- [130] A Kaminski, JJ Marchand, and A Laugier. Non ideal dark I-V curves behavior of silicon solar cells. *Solar Energy Materials and Solar Cells*, 51:221–231, 1998.

- [131] GDK Mahanama and HS Reehal. Dark and illuminated characteristics of crystalline silicon solar cells with ECR plasma CVD deposited emitters. *International journal of electronics*, 92(9):525–537, 2005.
- [132] J Beier and B Voss. Humps in dark I-V curves- analysis and explanation. In *Photovoltaic Specialists Conference, 1993., Conference Record of the Twenty Third IEEE*, pages 321–326. IEEE, 1993.
- [133] O Breitenstein, P Altermatt, K Ramspeck, MA Green, J Zhao, and A Schenk. Interpretation of the commonly observed I-V characteristics of c-Si cells having ideality factor larger than two. In *Photovoltaic Energy Conversion, Conference Record of the 2006 IEEE 4th World Conference on*, volume 1, pages 879–884. IEEE, 2006.
- [134] O Breitenstein, JP Rakotoniaina, M Hejjo Al Rifai, and M Werner. Shunt types in crystalline silicon solar cells. *Progress in Photovoltaics: Research and Applications*, 12(7):529–538, 2004.
- [135] WSM Brooks, SJC Irvine, and V Barrioz. High-resolution laser beam induced current measurements on  $\text{Cd}_{0.9}\text{Zn}_{0.1}\text{S}/\text{CdTe}$  solar cells. *Energy Procedia*, 10:232–237, 2011.
- [136] C Honsberg and S Bowden. *PV CDROM*, <http://www.pveducation.org/pvcdrom>, Accessed on 12/09/2013.
- [137] Priyanka, M Lal, and SN Singh. A new method of determination of series and shunt resistances of silicon solar cells. *Solar Energy Materials and Solar Cells*, 91(2):137–142, 2007.
- [138] C Gong, E Van Kerschaver, J Robbelein, NE Posthuma, S Singh, J Poortmans, and R Mertens. High efficient n-type interdigitated back contact silicon solar cells with screen-printed al-alloyed emitter. In *Photovoltaic Specialists Conference (PVSC), 2010 35th IEEE*, pages 003145–003148. IEEE, 2010.
- [139] M El-Tahchi, A Khoury, M De Labardonnie, P Mialhe, and F Pelanchon. Degradation of the diode ideality factor of silicon n–p junctions. *Solar Energy Materials and Solar Cells*, 62(4):393–398, 2000.
- [140] AG Aberle, SR Wenham, and MA Green. A new method for accurate measurements of the lumped series resistance of solar cells. In *Photovoltaic Specialists Conference, 1993., Conference Record of the Twenty Third IEEE*, pages 133–139. IEEE, 1993.

- [141] SJ Robinson, AG Aberle, and MA Green. Departures from the principle of superposition in silicon solar cells. *Journal of Applied Physics*, 76(12):7920–7930, 1994.
- [142] O Breitenstein. Understanding the current-voltage characteristics of industrial crystalline silicon solar cells by considering inhomogeneous current distributions. *Opto-Electronics Review*, 21(3):259–282, 2013.
- [143] G jiang Lin, J Bi, M Song, J Liu, W Xiong, and M Huang. III-V multijunction solar cells. 2013.
- [144] JF Geisz, DJ Friedman, JS Ward, A Duda, WJ Olavarria, TE Moriarty, JT Kiehl, MJ Romero, AG Norman, and KM Jones. 40.8% efficient inverted triple-junction solar cell with two independently metamorphic junctions. *Applied Physics Letters*, 93(12):123505, 2008.
- [145] DL King, BR Hansen, JM Moore, and DJ Aiken. New methods for measuring performance of monolithic multijunction solar cells. In *Photovoltaic Specialists Conference, 2000. Conference Record of the Twenty-Eighth IEEE*, pages 1197–1201. IEEE, 2000.
- [146] *Emcore CTJ Terrestrial Receiver Assembly*, <http://assets.componentsense.com/images/datasheets/89821-11-806719f4db94fd8c10dcab811f006cbd.pdf>, Accessed on 14/03/2013.
- [147] EmcoreCorporation. *Triple-Junction Solar Cell for Terrestrial Applications- Data sheet*,. <http://www.emcore.com/wp-content/uploads/CTJ-Cell-10mm.pdf>.
- [148] RD Schultz. On the design of concentrator photovoltaics modules. Master’s thesis, Nelson Mandela Metropolitan University, 2012.
- [149] G Shu, N Ou, P Hsueh, T Lin, J Wang, J Shen, C Wu, and C Ko. Measuring Photovoltages of III-V Multijunction Solar Cells by Electroluminescence Imaging. *Applied Physics Express*, 6(10):102302, 2013.
- [150] C Baur, M Hermle, F Dimroth, and AW Bett. Effects of optical coupling in III-V multilayer systems. *Applied physics letters*, 90(19):192109, 2007.
- [151] MA Steiner and JF Geisz. Non-linear luminescent coupling in series-connected multijunction solar cells. *Applied Physics Letters*, 100(25):251106, 2012.
- [152] D Derkacs, DT Bilir, and VA Sabnis. Luminescent coupling in GaAs/GaInNAsSb multijunction solar cells. *Photovoltaics, IEEE Journal of*, 3(1):520–527, 2013.

- [153] DJ Friedman, JF Geisz, and MA Steiner. Effect of luminescent coupling on the optimal design of multi-junction solar cells. *IEEE Journal of Photovoltaics*, 4(3):986–990, May 2014.
- [154] H Yoon, RR King, GS Kinsey, S Kurtz, and DD Krut. Radiative coupling effects in GaInP/GaAs/Ge multijunction solar cells. In *Photovoltaic Energy Conversion, 2003. Proceedings of 3rd World Conference on*, volume 1, pages 745–748. IEEE, 2003.
- [155] AS Brown and MA Green. Radiative coupling as a means to reduce spectral mismatch in monolithic tandem solar cell stacks theoretical considerations. In *Photovoltaic Specialists Conference, 2002. Conference Record of the Twenty-Ninth IEEE*, pages 868–871. IEEE, 2002.
- [156] Geoffrey S Kinsey, Peter Hebert, Kent E Barbour, Dmitri D Krut, Hector L Cotal, and Raed A Sherif. Concentrator multijunction solar cell characteristics under variable intensity and temperature. *Progress in Photovoltaics: Research and Applications*, 16(6):503–508, 2008.
- [157] A Ben Or and J Appelbaum. Estimation of multijunction solar cell parameters. *Progress in Photovoltaics: Research and Applications*, 21(4):713–723, 2013.
- [158] TA Gessert and TJ Coutts. Grid metallization and antireflection coating optimization for concentrator and one-sun photovoltaic solar cells. *Journal of Vacuum Science & Technology A*, 10(4):2013–2024, 1992.
- [159] G Siefer, C Baur, M Meusel, F Dimroth, AW Bett, and W Warta. Influence of the simulator spectrum on the calibration of multijunction solar cells under concentration. In *Photovoltaic Specialists Conference, 2002. Conference Record of the Twenty-Ninth IEEE*, pages 836–839. IEEE, 2002.
- [160] CA Gueymard, D Myers, and K Emery. Proposed reference irradiance spectra for solar energy systems testing. *Solar energy*, 73(6):443–467, 2002.
- [161] W Okullo, MK Munji, FJ Vorster, and EE van Dyk. Effects of spectral variation on the device performance of copper indium diselenide and multi-crystalline silicon photovoltaic modules. *Solar Energy Materials and Solar Cells*, 95(2):759–764, 2011.
- [162] P Faine, SR Kurtz, C Riordan, and JM Olson. The influence of spectral solar irradiance variations on the performance of selected single-junction and multi-junction solar cells. *Solar cells*, 31(3):259–278, 1991.

- [163] F Khan, SN Singh, and M Husain. Effect of illumination intensity on cell parameters of a silicon solar cell. *Solar Energy Materials and Solar Cells*, 94(9):1473–1476, 2010.
- [164] M Chegaar, A Hamzaoui, A Namoda, P Petit, M Aillerie, and A Herguth. Effect of illumination intensity on solar cells parameters. *Energy Procedia*, 36:722–729, 2013.
- [165] SC Solanki. *Solar photovoltaics: Fundamentals, technologies and applications*. PHI Learning Pvt. Ltd., 2011.
- [166] KM Kandil, SA Majida, MA Asma, MA Latifa, M Ibrahim, and AG Adel. Investigation of the performance of CIS photovoltaic modules under different environmental conditions. *Smart Grid and Renewable Energy*, 2:375–387, 2011.
- [167] P Singh, SN Singh, M Lal, and M Husain. Temperature dependence of I-V characteristics and performance parameters of silicon solar cell. *Solar Energy Materials and Solar Cells*, 92(12):1611–1616, 2008.
- [168] SM Sze. *Semiconductor devices: Physics and Technology*. John Wiley & Sons, 2008.
- [169] AK Sharma, SK Agarwal, and SN Singh. Determination of front surface recombination velocity of silicon solar cells using the short-wavelength spectral response. *Solar energy materials and solar cells*, 91(15):1515–1520, 2007.
- [170] Thorlabs. *Mounted long pass colored glass filters*, <http://www.thorlabs.com>, Accessed on 30/05/2014.

# Appendix A

## Research outputs associated with this work

### A.1 Journal publication

N. Kwarikunda, E.E. van Dyk, F.J. Vorster, W. Okullo, M.K. Munji, “Application of LBIC measurements for characterisation of triple junction solar cells”, *Physica B: Condensed Matter*, 439, 122-125 (2014)

### A.2 Conference papers

N. Kwarikunda, E.E. van Dyk, F.J. Vorster, W. Okullo, “LBIC measurements as a defect mapping tool for multijunction solar cells”, *Proceedings of the 29<sup>th</sup> European Photovoltaic Solar Energy Conference and Exhibition*, Amsterdam, Netherlands, 2084-2087 (2014)

N. Kwarikunda, E.E. van Dyk, F.J. Vorster, W. Okullo, “Characterisation of multijunction solar cells using the S-LBIC mapping technique” 2<sup>nd</sup> Southern African Solar Energy Conference (SASEC), Port Elizabeth, South Africa, 2014

N. Kwarikunda, E.E. van Dyk, F.J. Vorster, W. Okullo, “Effect of spectral changes on I-V parameters of triple junction solar cells”, 58<sup>th</sup> Annual Conference of South Africa Institute of Physics, Richards Bay, South Africa, 2013

N. Kwarikunda, E.E. van Dyk, F.J. Vorster, W. Okullo, M.K. Munji, “Application of LBIC measurements for characterisation of triple junction solar cells”, 5<sup>th</sup> South African Conference on Photonic Materials, Kariega Game Reserve, South Africa, 2013

# Appendix B

## Awards received

**N. Kwarikunda**, E.E. van Dyk, F.J. Vorster, W. Okullo, “LBIC measurements as a defect mapping tool for multijunction solar cells”, **Poster Award winner** in the thematic area of “Solar cells/Assemblies/Modules for Terrestrial Concentrator Systems and for Space Solar Generators”, 29<sup>th</sup> European Photovoltaic Solar Energy Conference and Exhibition, Amsterdam, Netherlands, 2014

**N. Kwarikunda**, E.E. van Dyk, F.J. Vorster, W. Okullo, “Analysis of photo-response of a back contact silicon solar cell under spot illumination”, **Best PhD Poster Presentation** in the Applied Physics Forum at the 59<sup>th</sup> Annual Conference of the South African Institute of Physics, University of Johannesburg, South Africa, 2014

**N. Kwarikunda**, E.E. van Dyk, F.J. Vorster, W. Okullo, M.K. Munji, “Application of LBIC measurements for characterisation of triple junction solar cells”, **Best Poster Presentation** at the 5<sup>th</sup> South African Conference on Photonic Materials, Kariega Game Reserve, South Africa, 2013